

MEMS-Based Microanalytical System for
Dielectrophoresis Studies of Biological Macromolecules

Shane M. Crippen

A thesis submitted in partial fulfillment of the
requirements for the degree of

Master of Science in Electrical Engineering

University of Washington

1999

Program Authorized to Offer Degree: Department of Electrical Engineering

20000627 179

DTIC QUALITY INSPECTED 4

University of Washington

Abstract

MEMS-Based Microanalytical System for
Dielectrophoresis Studies of Biological Macromolecules

Shane M. Crippen

Chairperson of the Supervisory Committee

Associate Professor Deirdre R. Meldrum

Department of Electrical Engineering

This thesis describes a body of work specifically addressing the design and fabrication of a MEMS-based microanalytical system capable of studying the dielectrophoresis of biological macromolecules such as DNA and bovine serum albumin (BSA). Through a process of discovery that involved extensive theoretical and literature based analysis coupled with laboratory validation and extension of current dielectrophoresis knowledge, it was concluded that DNA studied in this research exhibited both negative and positive dielectrophoresis depending upon the frequency of the applied electric field. Such knowledge may lead to the application of dielectrophoresis separation techniques for DNA.

University of Washington

Abstract

MEMS-Based Microanalytical System for
Dielectrophoresis Studies of Biological Macromolecules

Shane M. Crippen

Chairperson of the Supervisory Committee

Associate Professor Deirdre R. Meldrum

Department of Electrical Engineering

This thesis describes a body of work specifically addressing the design and fabrication of a MEMS-based microanalytical system capable of studying the dielectrophoresis of biological macromolecules such as DNA and bovine serum albumin (BSA). Through a process of discovery that involved extensive theoretical and literature based analysis coupled with laboratory validation and extension of current dielectrophoresis knowledge, it was concluded that DNA studied in this research exhibited both negative and positive dielectrophoresis depending upon the frequency of the applied electric field. Such knowledge may lead to the application of dielectrophoresis separation techniques for DNA.

© Copyright 1999

Shane M. Crippen

University of Washington

Graduate School

This is to certify that I have examined this copy of a master's thesis by

Shane M. Crippen

and have found it is complete and satisfactory in all respects,

and that any and all revisions required by the final

examining committee have been made.

Committee Members:

Deirdre R. Meldrum

Blake Hannaford

Ger van den Engh

Date: _____

In presenting this thesis in partial fulfillment of the requirements for a Master's degree at the University of Washington, I agree that the Library shall make its copies freely available for inspection. I further agree that extensive copying of this thesis is allowable only for scholarly purposes, consistent with "fair use" as prescribed in the U.S.

Copyright Law. Any other reproduction for any purposes or by any means shall not be allowed without my written permission.

Signature_____

Date_____

University of Washington

Abstract

MEMS-Based Microanalytical System for
Dielectrophoresis Studies of Biological Macromolecules

Shane M. Crippen

Chairperson of the Supervisory Committee

Associate Professor Deirdre R. Meldrum

Department of Electrical Engineering

This thesis describes a body of work specifically addressing the design and fabrication of a MEMS-based microanalytical system capable of studying the dielectrophoresis of biological macromolecules such as DNA and bovine serum albumin (BSA). Through a process of discovery that involved extensive theoretical and literature based analysis coupled with laboratory validation and extension of current dielectrophoresis knowledge, it was concluded that DNA studied in this research exhibited both negative and positive dielectrophoresis depending upon the frequency of the applied electric field. Such knowledge may lead to the application of dielectrophoresis separation techniques for DNA.

Table of Contents

Table of Contents	i
List of Figures	ix
List of Tables.....	xiii
Chapter 1 Introduction	1
1.1 Goals of the Genomation Laboratory.....	1
1.2 Statement of Need	2
1.2.1 Microanalytical System.....	2
1.2.2 Benchmark Experiment.....	4
1.3 Characterization of and Alternative Technologies for Biological Macromolecular Separation and Concentration	5
1.3.1 Characterization Research.....	5
1.3.2 Optical Trapping	5
1.3.3 Opt-electrostatic Trapping.....	6
1.3.4 Dielectrophoresis.....	6
1.4 Dielectrophoresis: The Manipulative Technique of Choice for Biological Macromolecules	7
1.5 Summary of Results	7
1.6 Organization of Thesis	8
Chapter 2 Theory.....	9

2.1	Development of Dielectrophoretic Force Expression	9
2.1.1	Force and Torque on Infinitesimal Dipole	10
2.1.2	Dielectric Particle with No Loss in Electric Field.....	11
2.1.3	Dielectric Particle with Loss in Electric Field	12
2.1.4	Layered Dielectric Particle with Loss in Electric Field	13
2.1.5	Effective Moment Calculation of Dielectrophoretic Force and Torque	15
2.2	Generalized Definition for Dielectrophoresis	17
2.2.1	Clausius-Mossotti Function	17
2.2.2	An Illustration of Frequency Dependent Dielectrophoresis.....	18
2.3	Dielectric Properties in General	20
2.3.1	Methods for Measuring Dielectric Properties	20
2.3.2	An Illustrative Dielectric Dispersion Curve.....	22
2.4	Dielectric Properties of DNA.....	26
2.5	Contemporary Dielectric Model of DNA.....	27
2.6	Parameter Dependence of Dielectric Dispersion	30
2.6.1	Molecular Weight.....	30
2.6.2	Concentration	30
2.6.3	Ionic Strength	31
2.6.4	Temperature	31
2.6.5	Summary of Parameter Dependence	31

2.6.6 Dielectric Dispersion Curves for DNA	32
2.7 Dielectric Properties of BSA.....	34
2.7.1 Contemporary Dielectric Model of BSA	34
2.7.2 Parameter Dependence of Dielectric Dispersion	35
2.7.3 Dielectric Dispersion Curves for BSA.....	35
2.8 Summary	37
Chapter 3 Related Work.....	38
3.1 Early Pioneers in Establishing Conditions of Dielectrophoresis	38
3.1.1 Pohl	38
3.1.2 Jones.....	41
3.2 Proposed Dielectrophoretic Separation Methods.....	43
3.2.1 Dielectrophoretic Migration.....	43
3.2.2 Dielectrophoretic Retention	43
3.2.3 Dielectrophoretic/Gravitational Field-Flow Fractionation.....	44
3.3 Dielectrophoretic Methods Applied to Cells and Microbeads	45
3.3.1 Davis and Giddings	45
3.3.2 Gascoyne, Wang, Huang, and Yang	45
3.4 Dielectrophoretic Methods Applied to Biological Macromolecules.....	54
3.4.1 Ajdari and Prost.....	54
3.4.2 Washizu.....	55

3.4.3	Asbury and van den Engh	58
3.5	Uncertainties and Discrepancies in Related Work	62
3.5.1	Dimensions of Parallel Array Electrodes	62
3.5.2	Applied Electric Field Strengths and Frequencies	63
3.5.3	Suspension Medium, Chamber, and Flow Conditions	63
3.6	Summary	64
Chapter 4	Methods and Materials	65
4.1	General Design of Microanalytical Systems	65
4.1.1	Critical Design Issues in Microanalytical Systems	65
4.1.2	Materials and Technologies for Fabrication of Microanalytical Systems:....	67
4.2	Electrical Subsystem Functional Requirements	69
4.2.1	MEMS Microelectrode Device	69
4.2.2	Electrical Interconnect.....	71
4.2.3	Electrical Instrumentation	72
4.3	Fluidic Subsystem Functional Requirements	74
4.3.1	MEMS Microfluidic Device.....	74
4.3.2	Fluidic Interconnect.....	75
4.3.3	Fluid Pump	76
4.4	Optical Subsystem Functional Requirements	77
4.4.1	Microscope Interface Platen.....	77

4.4.2	Microscopy Station	78
4.5	Microanalytical System Integration	81
4.6	Design and Fabrication of the Electrical Subsystem.....	83
4.6.1	MEMS Microelectrode Device	84
4.6.2	Geometry #1 - Parallel, Interdigitated.....	86
4.6.3	Geometry #2 - Parallel, Interdigitated, Castellated	88
4.6.4	Geometry #3 - Concentric Travelling Wave	90
4.6.5	Geometry #4 - Variable Pitch Rate	92
4.6.6	Variable Electrode Thickness and Summary of Electrode Geometries	94
4.6.7	Photolithography	95
4.6.8	Electrical Interconnect.....	101
4.7	Design and Fabrication of the Fluidic Subsystem.....	104
4.7.1	MEMS Microfluidic Device.....	104
4.7.2	Characteristic Fluid Flow Velocities.....	106
4.7.3	Selected Channel Geometries.....	110
4.7.4	Soft Lithography Method of Replica Molding.....	111
4.7.5	SU-8 Process and Protocols.....	118
4.7.6	SU-8 25 Characterization: Bias Point and Linearization Methods.....	121
4.7.7	General Characterization for all SU-8 Resists.....	124
4.7.8	Fluidic Interconnect.....	124

4.8 Design and Fabrication of the Microscope Interface Platen	125
4.9 Fluidic Sample Preparation	126
4.10 Summary	127
Chapter 5 Data Collection	128
5.1 Characteristic Frequency Response of Microelectrical Devices	128
5.1.1 Measuring Frequency Response.....	128
5.1.2 Frequency Response as Function of Dielectric Medium for Electrode Thickness of 40 Å	131
5.1.3 Frequency Response as Function of Dielectric Medium for Electrode Thickness of 2000 Å	132
5.1.4 Frequency Response as Function of Electrode Thickness	134
5.1.5 Summary of Frequency Response as Function of Dielectric Medium and Electrode Thickness	136
5.2 DNA Trapping Response for Frequencies up to 100 Hz	137
5.2.1 Parallel Electrode Structures	138
5.2.2 Castellated Electrode Structures.....	139
5.3 DNA Trapping Response for Frequencies Between 100 Hz and 1 kHz.....	139
5.3.1 Parallel Electrode Structures	139
5.3.2 Castellated Electrode Structures.....	140
5.4 DNA Trapping Response for Frequencies Between 1 kHz and 10 kHz	141
5.4.1 Parallel Electrode Structures	141

5.4.2	Castellated Electrode Structures.....	142
5.5	DNA Trapping Response for Frequencies Between 10 kHz and 100 kHz	142
5.5.1	Parallel Electrode Structures	143
5.5.2	Castellated Electrode Structures.....	144
5.6	DNA Trapping Response for Frequencies Between 100 kHz and 1 MHz.....	144
5.6.1	Parallel Electrode Structures	144
5.6.2	Castellated Electrode Structures.....	145
5.7	DNA Trapping Response for Frequencies Around 1 MHz.....	145
5.7.1	Parallel Electrode Structures	145
5.7.2	Castellated Electrode Structures.....	148
5.8	Summary of Trapping Response for DNA.....	148
5.9	Summary	149
Chapter 6	Data Analysis and Reduction	151
6.1	Development of Lumped Parameter Circuit Model for Microelectrical Devices	152
6.1.1	Problem Statement	153
6.1.2	Electrode Polarization	154
6.1.3	Modeling the Effects of Electrode Polarization	155
6.1.4	Electrode Polarization Determines Dependency of Low Frequency System Response on Electrode Thickness	161
6.2	Proposed Model of DNA Trapping.....	162

6.3 Summary	165
Chapter 7 Conclusion.....	166
7.1 Development and Acquisition of Experimental Infrastructure	166
7.2 Dielectrophoresis of DNA.....	167
7.2.1 Process of Discovery	167
7.2.2 Discussion of Dielectrophoresis Studies	169
7.2.3 Summary of Experimental Conclusions.....	171
7.2.4 Uncertainties and Unanticipated Problems	171
7.3 Potential Applications	172
7.4 Future Work	174
Bibliography.....	176
Appendix A... ..	189

List of Figures

Figure 2-1 Layered particle	14
Figure 2-2 Clausius-Mossotti curve	19
Figure 2-3 Dielectric dispersion curve for a two-component solution.....	23
Figure 2-4 Possible dielectric dispersion curve of DNA.....	33
Figure 2-5 Possible dielectric dispersion curve of BSA	36
Figure 3-1 Electrode geometries of Pohl.....	40
Figure 3-2 Isomotive dielectrophoretic force field geometry	41
Figure 3-3 Experimental test cell used by Jones	42
Figure 3-4 Positive and negative dielectrophoretic collection regions	47
Figure 3-5 Electric field distribution.....	48
Figure 3-6 Vector representation of $\nabla \vec{E} ^2$	51
Figure 3-7 DEP/G-FFF system	53
Figure 3-8 Regions of dielectrophoresis for avidin.....	58
Figure 3-9 Trapping potential	60
Figure 3-10 Schematic of swirling motion of trapped DNA molecules	61
Figure 3-11 Definition of electrode dimensions	62
Figure 4-2 MEMS microelectrode device	70
Figure 4-3 Electrical interconnect	72

Figure 4-4 Electrical instruments	73
Figure 4-5 MEMS microfluidic device	75
Figure 4-6 Fluidic interconnect	76
Figure 4-7 Microscope interface platen	78
Figure 4-8 Absorption and emission spectra for fluorescent dyes	79
Figure 4-9 Microscopy station	81
Figure 4-10 Microanalytical system integration	82
Figure 4-12 Microanalytical system integration into Zeiss Axiovert 135	83
Figure 4-13 Schematic of MEMS microelectrode device	84
Figure 4-14 Detailed schematic of MEMS microelectrode device	86
Figure 4-15 Parallel, interdigitated, electrode geometry	87
Figure 4-16 Parallel, interdigitated, castellated electrode geometry	89
Figure 4-17 Concentric travelling wave electrode geometry	91
Figure 4-18 Variable pitch rate geometry	93
Figure 4-19 MRC 882 SputterSphere.....	96
Figure 4-20 Photolithography chemicals	97
Figure 4-21 Light field photomask.....	98
Figure 4-22 Quintel 2001 3" Aligner	99
Figure 4-23 A processed wafer containing microelectrode devices	100
Figure 4-24 Tempress 601 Dicing Saw.....	101

Figure 4-25 Electrical interconnect	102
Figure 4-26 Machine shop drawing for cantilever arm.....	103
Figure 4-27 MEMS microfluidic device	104
Figure 4-28 Surface plot of mean fluid flow velocity.....	110
Figure 4-29 Channel shapes	111
Figure 4-30 SU-8 photomasks.....	113
Figure 4-31 Sheet of photomasks.....	114
Figure 4-32 SU-8 master mold.....	115
Figure 4-33 Illustration of micromolding system	116
Figure 4-34 Micromolding system.....	117
Figure 4-35 Elements of the molding process.....	118
Figure 4-36 SU-8 Photoresist and associated processing chemicals.....	119
Figure 4-37 Thickness and spin speed curve for SU-8 25	120
Figure 4-38 Bias point spin speed curve for SU-8 25 resist.....	123
Figure 4-39 Linearized spin speed curve	123
Figure 4-40 Microfluidic assembly	125
Figure 4-41 Optical mechanical interface	126
Figure 5-1 Comparison of electrode configurations	130
Figure 5-2 Characteristic frequency response of 40 Å microelectrode device	131
Figure 5-3 Characteristic frequency response of 2000 Å microelectrode device	133

Figure 5-4 Characteristic frequency response as function of electrode thickness	135
Figure 5-5 DNA trapping at 30 Hz.....	138
Figure 5-6 DNA trapping at 100 Hz.....	140
Figure 5-7 DNA trapping at 1 kHz.....	141
Figure 5-8 DNA trapping at 10 kHz.....	143
Figure 5-9 DNA trapping at 1 MHz and low threshold electric field strength	146
Figure 5-10 DNA trapping at 1 MHz and high threshold electric field strength	147
Figure 6-1 System circuit model	158
Figure 6-2 Lumped parameter circuit model.....	159
Figure 6-3 Equivalent circuit.....	160
Figure 6-4 Model of DNA trapping	162

List of Tables

Table 2.1 Summary of the dependence of the dispersion regions on various parameters	32
Table 3.1 Comparison of electrode parameters among various groups	63
Table 4.1 Definition of geometries used in variable pitch rate design.....	94
Table 4.2 Wafers of various electrode thickness.....	95
Table 4.3 Example of fluid flow velocity calculation.....	109
Table 4.4 Operational protocols for patterning SU-8 photoresist	124
Table 5.1 Summary of frequency response.....	136
Table 5.2 Summary of trapping response for DNA	149

Dedication

I wish to first and foremost thank my advisor and friend, Deirdre R. Meldrum, in her support of this research. She brought me into her lab, paid my tuition, supported my proposals, and never questioned my judgement. This research was by no means inexpensive. With the initial lack of infrastructure to conduct this research, acquisitions were key early on. She supported these acquisitions and, thereby, allowed me to carry out my research.

Next I wish to thank my research mentor and friend, Mark Holl, in his support of this research. From the early morning bemoanings, to the afternoon meetings, to the late night Taco Bell runs he never tired as I pushed forward under my limited time constraints. As I was pushy and compulsive at times, he never turned his back on me and always had an open door. Wet under the collar when I started, he single handedly taught me how to be a research engineer. He truly made this a valuable experience for me, and I never could have accomplished this research without him.

I wish to thank my friends, Neal and Mohan, for putting up with me these past months. Neal always knew how to appease the cookie monster in me. He unselfishly gave of his time whenever I had a question. I could always count on him to be there when I needed him. As I do not proclaim to be a chemical reagent expert, Mohan helped me to prepare the fluid samples I used in this research. I could always count on him to ask how my day was going.

I wish to thank the wonderful friends I made during my time here in Seattle: Clint, Thomas, Lance, Brian, and Len. To my roommate, Clint, I always felt at ease talking with you. My verbosity when we were together can only be explained by my admiration of you. Thomas, we were inseparable. From Lake Chelan, to Mount Si, to the Columbia River Gorge, to the Yakima River Valley, to Tiger Mountain, you and I explored Washington together. As I am an explorer at heart, your companionship made those experiences that much more valuable. Even in our busiest moments, we always managed to sneak out for a cup of coffee. Lance, we befriended each other when I first moved

here and remained friends throughout my stay. Although we didn't always see eye to eye, something held us together. I know my cat, Sandy, especially appreciated your affection in her time of rehabilitation. You will become a wonderful officer for the Navy. Hang in there. You'll make it. Brian, you finished here before the rest of us and moved on, and your kindness and generosity will always be remembered. From the beginning, you always ensured we all got together in our short time here. I look forward to seeing you and Sara over the holidays. Len, we've known each from the beginning as well. I really enjoyed talking philosophy with you over our ping-pong matches. Our time here is finished, but you all will always live on as part of me. May chance one day again cross our paths again. I wish you all only happiness and good fortune.

I wish to thank my family for their support of me throughout my entire life. They taught me responsibility and accountability early on in the most abnormal of ways. The antithesis of controlling, they always let me make my own decisions and never questioned those decisions. The freedom and spirit of life I value today results from their parental philosophy. Finally, I wish to thank the US Air Force Academy for providing me with countless opportunities under the caveat of hard work achievement. I look forward to serving my Air Force and my country. Public service is the most noble of noble endeavors.

1 Introduction

This thesis describes a body of work that can be viewed from two global perspectives: an engineering perspective and a scientific perspective. From an engineering perspective, it specifically addresses the design and fabrication of a microanalytical system capable of studying the dielectrophoresis of biological macromolecules such as DNA and bovine serum albumin (BSA). From a scientific perspective, this thesis builds upon and extends the scientific work of others in the field of dielectrophoresis such as Asbury and van den Engh, Washizu, and Gascoyne [2, 3, 34-40, 102-116]. The impetus for studying the dielectrophoresis of biological macromolecules such as DNA and BSA derives from the specific needs of the Genomation Laboratory located at the University of Washington.

1.1 Goals of the Genomation Laboratory

The goals of the Genomation Laboratory located at the University of Washington are in line with the sequencing technology goal of the Human Genome Project as delineated by Collins [24]. The long-term goal of the Genomation Laboratory is to develop expandable, exportable technology to automate and improve a key area and current bottleneck of genomic research: the automated handling of submicroliter fluid samples. According to Meldrum, automated fluid sample handling is necessary for the Human Genome Project to meet its sequencing goals and also to meet the increasing demands from medicine, agriculture, and environmental science [54].

Funded by the National Institutes of Health, the Genomation Laboratory and subcontractor Orca Photonics Systems, Inc. initially developed the Acapella 1k system capable of preparing 1000 samples for polymerase chain reactions (PCRs), restriction enzyme digests (RED), and Sanger sequencing reactions (SR) in an 8 hour work day. The most recent system, the Acapella 5k, came online in fiscal year 1999 and is capable of preparing 5000 samples in an 8 hour work day. All fluid handling occurs in piezo-electric dispensers and glass microcapillaries.

1.2 Statement of Need

Acapella 1k and 5k fluid handling protocols dictate the addition of BSA as a reagent to mitigate the effects of nonspecific adsorption of Taq polymerase to the walls of the piezo-electric dispensers and microcapillaries. Downstream protocols, however, are intolerant of BSA, thus, motivating the development of a procedure that can separate DNA from BSA. One method of biological macromolecular manipulation that might enable this is dielectrophoresis.

Two specific objectives were identified to address this need:

- 1) The design and fabrication of a microanalytical system to examine the dielectrophoresis of biological macromolecules and
- 2) The demonstration of said microanalytical system using a benchmark experiment already demonstrated by Asbury and van den Engh as being capable of trapping DNA using dielectrophoresis [2, 3].

These objectives, therefore, constitute the subject of this thesis.

1.2.1 *Microanalytical System*

This section briefly describes the components of the microanalytical system used to study the dielectrophoresis of biological macromolecules in this research. The system serves as a flexible, experimental platform that is comprised of three subsystems: electrical, fluidic, and optical.

The electrical subsystem is comprised of a MEMS microelectrode device, electrical interconnect, and associated electrical measurement instruments. The microelectrode device was designed and fabricated using standard photolithography procedures. A light field chrome photomask, generated by PhotoSciences (Torrance, California, USA) from an Auto CAD LT 98 (Autodesk, Inc.) DXF file, was used to pattern the microelectrode device geometry on 0.020" thick, 3" diameter borosilicate glass wafers purchased from

US Precision Glass Co., Inc. (Elgin, IL, USA). The metal deposition process involved the deposition of a Tungsten adhesion layer at 20 Å or 75 Å followed by a gold layer at varied thicknesses ranging from 40 Å to 10,000 Å. The flexibility of the electrical interconnect allows many different microelectrode device designs to be evaluated. For purposes of this research, the electrode structures used were similar to those of Gascoyne, Asbury and van den Engh, and Washizu [2, 3, 34-40, 102-116].

The fluidic subsystem is comprised of a MEMS microfluidic device, fluidic interconnect, and fluid pump. The microfluidic device was designed and fabricated using standard photolithography and soft photolithography procedures coupled into a micromolding system. A dark field photomask, generated by an Avatra engineering plotter at 3600 dpi resolution from an Auto CAD LT 98 (Autodesk, Inc.) DXF file, was used to pattern the microfluidic device geometry on 0.025 " thick, 4" diameter silicon wafers purchased from Addison Engineering, Inc. (San Jose, CA, USA). The microfluidic devices were patterned at various geometries using an SU-8 epoxy-based negative photoresist purchased from MicroChem, Corp. (Newton, MA, USA). This initial pattern transfer served as a master mold to subsequently cast polydimethylsiloxane (PDMS) against (Sylgard 184, K.R. Anderson, Inc., Santa Clara, CA). This PDMS then served as a mold for which to cast a two-part polyurethane against. This polyurethane then served as the master mold against which future microfluidic devices could be cast using PDMS. These molding methods and support structure allow alternative channel geometries to be examined with rapid turn around times. For purposes of this research, the microfluidic device contained a channel geometry of 500 µm in width, 10 mm in length, and 50 µm in depth.

The optical subsystem is comprised of a microscope interface platen and epi-fluorescent microscopy station. The interface platen was designed using SolidWorks 98 (Personal Workstations, Bellevue, WA, USA). The platen and support hardware serve to interface the microelectrode and microfluidic devices to the epi-fluorescent microscopy station. The microanalytical system, as a whole, allows the electrical and fluidic assemblies to be

inserted and removed from the epi-fluorescent microscopy station via the microscope interface platen with ease, repeatable performance, and rapid setup times.

1.2.2 Benchmark Experiment

A demonstration of the microanalytical system was performed using a benchmark experiment similar to that already demonstrated by Asbury and van den Engh as being capable of trapping DNA via dielectrophoresis [2, 3].

The benchmark experiment used similar parameters of DNA length (48.5 kb λ phage purchased from USB Corp., Cleveland, OH, USA) and concentration (200 ng/mL), labeling (YOYO-1 iodide purchased from Molecular Probes, Eugene, OR, USA), and fluid medium (Tris-buffer: 0.4 mM Tris, 0.5 mM NaCl, and 0.04 mM EDTA).

The fluorescently labeled DNA in Tris-buffer was injected into the microfluidic device channel of 500 μm in width, 10 mm in length, and 50 μm in depth. Both input and output ports were subsequently clamped to prevent fluid flow. The microfluidic device channel directed the sample over the electrode arrays of the microelectrode device of both interdigitated parallel and parallel castellated design. The parallel geometry had an electrode width of 70 μm and gap of 30 μm for an electrode period of 100 μm . The castellated design also had a 100 μm period with characteristic tooth dimension of 20 μm . The fluorescently labeled DNA was then observed using a Zeiss Axiovert 135 epi-fluorescent microscope under application of applied electric fields at discrete frequencies of 30 Hz, 100 Hz, 1 kHz, 10 kHz, 100 kHz, and 1 MHz and at applied voltages between 0.5 $V_{\text{p-p}}$ and 20 $V_{\text{p-p}}$. Image capture was performed by integrating the image for 5 seconds using the integration feature of a Dage-MTI 3-Chip Cooled CCD Color Camera (Michigan City, IN).

1.3 Characterization of and Alternative Technologies for Biological Macromolecular Separation and Concentration

This section briefly examines current work that may help better characterize biological macromolecules such as DNA and BSA. This section also briefly examines alternative technologies that may serve as manipulative techniques. These technologies include optical trapping, opt-electrostatic trapping, and dielectrophoresis. A comparison of these techniques in the context of the needs of the Genomation Laboratory is given along with the reasons that resulted in the subsequent selection of dielectrophoresis.

1.3.1 Characterization Research

New technologies that support the goals of the Genomation Laboratory may be enabled through a better understanding of the conformational and dielectric properties of biological macromolecules such as DNA and BSA. Although extensive studies on the conformational and dielectric properties of DNA have been conducted, DNA is still not well understood or characterized. For example, competing theories still exist over the mechanics of DNA movement through a gel and other viscous materials. This is not to say that characterizing DNA is easy. Indeed, DNA undergoes many conformational changes, such as coiled or elongated, depending on environmental conditions such as pH and ionic strength of the medium.

Research by such people as Smith and Perkins attempted to better characterize the mechanical properties of DNA [56, 65-68, 75-78]. For example, Smith determined force versus extension curves for DNA through direct mechanical measurements of the elasticity of single DNA molecules by using magnetic beads. Others such as Takashima and Mandel have attempted to better characterize the dielectric properties of DNA.

1.3.2 Optical Trapping

Optical trapping refers to the direct manipulation of particles using lasers. The principle pioneer in this area is Ashkin [4-15]. This technique essentially relies on gradient

trapping forces resulting from radiation pressure that subsequently push dielectric particles into the high-intensity region of a highly focused light beam. Two characteristic traps exist: levitation traps and tweezer traps. Chiu and Zare first demonstrated experimental optical trapping of DNA [22]. They later applied this method to demonstrate the injection of single DNA molecules into tapered capillaries [21].

Optical trapping better serves as a technique to micromanipulate individual molecules of DNA than as a technique to effect mass manipulation of DNA. This is due to the small trapping capacity of a laser trap. Resolution is on the order of a single molecule. In satisfying the needs of the Genomation Laboratory, however, a mass manipulative technique is required. Further, the knowledge and equipment infrastructure to deploy laser trapping methods does not currently exist in this lab.

1.3.3 Opt-electrostatic Trapping

Mizuno combined lasers and electric fields to manipulate particles such as DNA [57-60, 62, 63]. He termed this technique opt-electrostatic trapping and demonstrated the conformational stretching of DNA under an intense dc field, subsequent cutting by an ultraviolet laser, and isolation and recovery into a capillary. Such abilities, he theorized, could lead to a micromanipulation technique for accelerated DNA sequencing.

As with optical trapping, opt-electrostatic trapping better serves as a technique to micromanipulate individual molecules of DNA, and the knowledge and equipment infrastructure to deploy lasers does not currently exist in this lab.

1.3.4 Dielectrophoresis

Dielectrophoresis is a dipole-dependent phenomenon that relies on highly nonuniform fields to move particles. Dielectrophoretic manipulative techniques have recently grown in popularity. This increase in popularity is due to recent advances in the fundamental understanding of dielectrophoresis as well as the available infrastructure to fabricate devices with dielectrophoresis capabilities. Applications of this technique are numerous

and range from particle characterization to sorting and separation. It has, however, seen limited application with particles in the range $< 1 \mu\text{m}$ as is the case with DNA. Reasons for this are due to the paradigm that particles of size $< 1 \mu\text{m}$ are typically thought to be dominated by random thermal or Brownian motion in solution. The work of Asbury and van den Engh and Washizu has clearly demonstrated that DNA can be routinely and efficiently concentrated [2, 3, 102-116].

1.4 Dielectrophoresis: The Manipulative Technique of Choice for Biological Macromolecules

In satisfying the needs of the Genomation Laboratory, it was concluded that dielectrophoresis may hold promise as a manipulative technique to effect the mass manipulation of biological macromolecules such as DNA and BSA. The phenomenon is very sensitive to the dielectric properties of the particle. DNA and BSA have significantly different dielectric properties. For example, the magnitude of the dipole moment for DNA is much larger than for BSA. This difference in dipole moments further results in significant differences in their respective dielectric constants or permittivities. It was concluded that such differences may prove to successfully separate DNA from BSA and, thereby, satisfy the needs of the Genomation Laboratory.

1.5 Summary of Results

This research successfully designed and implemented a microanalytical system for conducting dielectrophoresis studies of biological macromolecules such as DNA and BSA. Through these dielectrophoresis studies, it was concluded that the DNA examined in this research exhibits both negative and positive dielectrophoresis. Further, such behavior requires that the DNA examined in this research be modeled as a particle with ohmic and/or dielectric losses. Separation of DNA from BSA was not demonstrated due to nonspecific adsorption and optical detection problems encountered with BSA. It is

anticipated, though, that the results of this work will lead to a dielectrophoretic separation method capable of separating DNA from BSA.

1.6 Organization of Thesis

This thesis is organized in the following manner. In Chapter 2, a theory of dielectrophoresis using the effective moment method of Jones will be presented [45]. It will be shown that a particle can undergo positive or negative dielectrophoresis depending on particle and medium conditions and also the frequency and magnitude of the applied electric field. This has important ramifications in the use of dielectrophoresis manipulative techniques. Chapter 3 will look at current applications of dielectrophoresis as reported in the available literature along with the sometimes disparate results. Structures for generating the necessary highly nonuniform electric fields with well defined minimum and maximum field regions for dielectrophoresis will also be considered. Chapter 4 will present the decoupled design method of the microanalytical system as fabricated, characterized, and used for purposes of this research to conduct dielectrophoresis studies of biological macromolecules. Chapter 5 will present the observed experimental results of dielectrophoresis studies of DNA. Chapter 6 will analyze these results and propose a model that attempts to explain the dielectrophoretic behavior of DNA studied in this research throughout the frequency range from near dc to 1 MHz. Chapter 7 will conclude with the findings and contributions of this research, uncertainties, potential dielectrophoresis applications, and suggested future work.

2 Theory

This chapter will outline the fundamental principles of dielectrophoresis according to the effective moment method of Jones [45]. The dielectrophoretic force for three different particles in the presence of a nonuniform electric field will be considered: a single layered particle with no ohmic or dielectric loss, a single layered particle with ohmic and/or dielectric loss, and a layered particle with ohmic and/or dielectric loss. It will be shown using the complex Clausius-Mossotti function that the frequency dependent dielectric properties of the particle determine whether it experiences a phenomenon termed positive dielectrophoresis or negative dielectrophoresis. The relevant phenomenon determines how the particle behaves in the presence of a nonuniform electric field. The frequency dependent dielectric properties of biological macromolecules such as DNA and bovine serum albumin (BSA) will be considered. It will be further shown how parameters such as molecular weight, concentration, ionic strength, and temperature effect dielectric properties. An understanding of these principles will lend understanding to the results reported in the available literature (see Chapter 3) and the observed experimental results reported in Chapters 5 and 6.

2.1 Development of Dielectrophoretic Force Expression

Pohl first termed dielectrophoresis as the "translational motion of neutral matter caused by polarization effects in a nonuniform electric field" [69]. Since then, many have sought to understand the phenomenon of dielectrophoresis and apply its principles towards useful means. This section will clearly establish the theoretical basis for dielectrophoresis according to the effective moment method developed by Thomas B. Jones [45]. The resulting dielectrophoretic force expression will then lend insight into the behavior of particles in nonuniform electric fields.

2.1.1 Force and Torque on Infinitesimal Dipole

A particle is said to have a dipole moment when its positive and negative charge centers are displaced. Such a particle is called a dipole. This dipole can be either a permanent or an induced dipole. The dipole moment is a vector, \vec{p} , defined as,

$$\vec{p} = q\vec{d}, \quad 2.1$$

where: q is the magnitude of the charge and \vec{d} a vector with direction from negative to positive charge center. The unit of dipole moment is the Debye (D) where 1 D is equivalent to $3.33 \cdot 10^{-30}$ Coulomb-meter or 10^{-30} esu-cm.

The presence of an externally applied electric field will influence the dipole. In an uniform electric field, the net force on the dipole is zero due to equal and opposite forces experienced by the positive and negative charge centers. The dipole will, however, experience a torque and align at some equilibrium angle with respect to the electric field. This torque, \vec{T} , is given by,

$$\vec{T} = \vec{p} \times \vec{E}, \quad 2.2$$

where: \vec{p} is the dipole moment and \vec{E} the electric field vector.

In a nonuniform electric field, the positive and negative charge centers will experience different values of the electric field, \vec{E} , and hence experience a net force. The net force, \vec{F}_{dipole} , is given by,

$$\vec{F}_{dipole} = (\vec{p} \cdot \nabla) \vec{E}, \quad 2.3$$

where: \vec{p} is the dipole moment, ∇ the del operator, and \vec{E} the electric field vector.

The torque experienced by a dipole in a nonuniform field is also given by Eq. 2.2 and thus a dipole will experience a torque in both uniform and nonuniform electric fields.

From Eq. 2.3, it is seen that a dipole will only experience a dielectrophoretic force in the presence of a nonuniform field.

2.1.2 Dielectric Particle with No Loss in Electric Field

The effective moment method will now be introduced to determine the dipole moment in Eq. 2.3 and, thus, enable the calculation of electromechanical forces and torques exerted by electric fields upon particles. The effective dipole moment, \overline{p}_{eff} , aligned parallel to the applied field is defined as the moment of an equivalent, free-charge, point dipole that, when immersed in the same dielectric liquid of permittivity ϵ_1 and positioned at the centroid of the original particle, produces the same dipolar electrostatic potential. For a dielectric particle, the effective dipole moment is determined by solving the appropriate boundary value problem and then comparing this to the induced dipole term of the electrostatic potential solution, Φ_{dipole} , defined as,

$$\Phi_{dipole} = \frac{|\overline{p}_{eff}| \cos \theta}{4\pi\epsilon_1 r^2}, \quad 2.4$$

where: θ and r are the polar and radial position in spherical coordinates and ϵ_1 the permittivity of the medium.

It can then be shown using Eq. 2.4 that a dielectric sphere of radius, R , and permittivity, ϵ_2 , suspended in a fluid of permittivity, ϵ_1 , and subjected to an electric field of magnitude, E_0 , will experience an effective dipole moment given by,

$$|\overline{p}_{eff}| = 4\pi K R^3 |\overline{E}|, \quad 2.5$$

where K is called the Clausius-Mossotti function. For particles experiencing no ohmic or dielectric loss, the Clausius-Mossotti function provides a measure of the strength of the effective polarization of a spherical particle and is defined as,

$$K = \frac{\epsilon_2 - \epsilon_1}{\epsilon_2 + 2\epsilon_1}, \quad 2.6$$

where ϵ_1 and ϵ_2 are the permittivities of the medium and particle, respectively. When $\epsilon_2 > \epsilon_1$, then $K > 0$, and the effective moment vector is colinear with the applied electric field. Also when $\epsilon_1 > \epsilon_2$ and $K < 0$, the effective moment vector and applied electric field are antiparallel. The Clausius-Mossotti function is limited to values within the range $-0.5 \leq K \leq 1.0$.

2.1.3 Dielectric Particle with Loss in Electric Field

When considering ohmic loss present in the system, the particle and fluid medium now have finite conductivities, σ_2 and σ_1 , in addition to their dielectric permittivities, ϵ_2 and ϵ_1 , respectively. In this case, the complex permittivities of the medium and particle are defined as,

$$\underline{\epsilon}_1 = \epsilon_1 + \frac{\sigma_1}{j\omega} \quad 2.7$$

and

$$\underline{\epsilon}_2 = \epsilon_2 + \frac{\sigma_2}{j\omega}. \quad 2.8$$

Through a boundary value problem solution for the potential at the surface of the particle, it can be shown that the complex effective dipole moment, \overline{p}_{eff} , is given by,

$$\overline{p}_{eff} = 4\pi\epsilon_1 \underline{K} R^3 \overline{E}, \quad 2.9$$

where the complex Clausius-Mossotti function, \underline{K} , is given by,

$$\underline{K} = \frac{\underline{\epsilon}_2 - \underline{\epsilon}_1}{\underline{\epsilon}_2 + 2\underline{\epsilon}_1}. \quad 2.10$$

The underbar present in Eqs. 2.7 through 2.10 denotes the fact that the terms are now complex entities.

Dielectric loss, ϵ'' , can also occur in the system. In such instances, more general forms of Eqs. 2.9 and 2.10 can be used by defining $\underline{\epsilon}_1$ as,

$$\underline{\epsilon}_1 = \underbrace{\epsilon_1'}_{\epsilon_1} - \underbrace{j\epsilon_1''}_{\text{dielectric loss}} + \underbrace{\frac{\sigma_1}{j\omega}}_{\text{ohmic loss}}, \quad 2.11$$

and by defining $\underline{\epsilon}_2$ as,

$$\underline{\epsilon}_2 = \underbrace{\epsilon_2'}_{\epsilon_2} - \underbrace{j\epsilon_2''}_{\text{dielectric loss}} + \underbrace{\frac{\sigma_2}{j\omega}}_{\text{ohmic loss}}, \quad 2.12$$

where: the substitutions $\epsilon_1 \rightarrow \epsilon_1'$ and $\epsilon_2 \rightarrow \epsilon_2'$ have been performed. The factor $4\pi\epsilon_1$ is also replaced by $4\pi\epsilon_1'$ in Eq. 2.9.

2.1.4 Layered Dielectric Particle with Loss in Electric Field

Layered particles have layers or shells each with its own respective complex permittivity as shown in Figure 2-1.

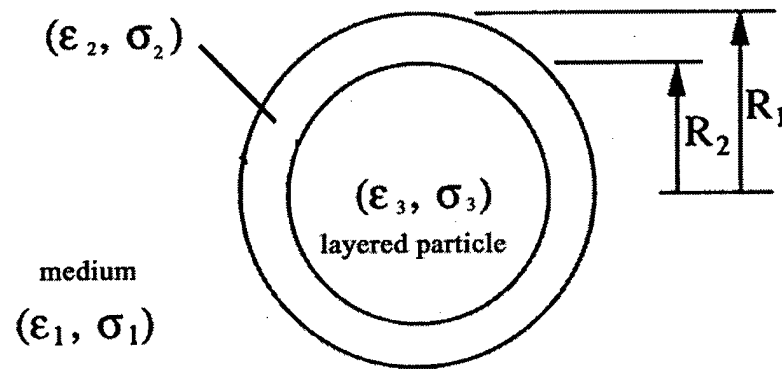


Figure 2-1 Layered particle.

An equivalent single-layered representation for the layered particle can be determined through an effective permittivity given by,

$$\epsilon_2' = \epsilon_2 \left\{ \frac{a^3 + 2 \left(\frac{\epsilon_3 - \epsilon_2}{\epsilon_3 + 2\epsilon_2} \right)}{a^3 - \left(\frac{\epsilon_3 - \epsilon_2}{\epsilon_3 + 2\epsilon_2} \right)} \right\}. \quad 2.13$$

In the case of a particle with core complex permittivity, ϵ_3 , and core radius, R_2 , concentric layer with complex permittivity, ϵ_2 , and outer radius, R_1 , and suspended in a medium of complex permittivity, ϵ_1 , and $a = R_1/R_2$, the complex Clausius-Mossotti function is given by,

$$\underline{K} = \frac{\epsilon_2' - \epsilon_1}{\epsilon_2' + 2\epsilon_1}. \quad 2.14$$

This method for determining the effective permittivity can be extended to a particle with any number of layers. As an alternative simplifying approximation, it can be shown that

the complex Clausius-Mossotti function may be written as a partial fraction expansion given by,

$$\underline{K} = K_{\infty} - \frac{\Delta K_{\alpha}}{j\omega\tau_{\alpha} + 1} - \frac{\Delta K_{\beta}}{j\omega\tau_{\beta} + 1} - \dots - \frac{\Delta K_N}{j\omega\tau_N + 1}, \quad 2.15$$

where: N denotes the number of relaxation times inherent in the system consisting of the particle and suspension medium and $\tau_{\alpha}, \tau_{\beta}, \dots, \tau_N$ are the associated time constants. Also ΔK_i denotes the change in the value of the permittivity resulting from the relaxation, and ω is the radial frequency. Equation 2.15 can be broken up into its real and imaginary components, and they are defined as,

$$\text{Re}[\underline{K}] = K_{\infty} - \frac{\Delta K_{\alpha}}{\omega^2\tau_{\alpha}^2 + 1} - \frac{\Delta K_{\beta}}{\omega^2\tau_{\beta}^2 + 1} - \dots - \frac{\Delta K_N}{\omega^2\tau_N^2 + 1} \quad 2.16$$

and

$$\text{Im}[\underline{K}] = K_{\infty} - \frac{\omega\tau_{\alpha}\Delta K_{\alpha}}{\omega^2\tau_{\alpha}^2 + 1} - \frac{\omega\tau_{\beta}\Delta K_{\beta}}{\omega^2\tau_{\beta}^2 + 1} - \dots - \frac{\omega\tau_N\Delta K_N}{\omega^2\tau_N^2 + 1}. \quad 2.17$$

This will be of use in formalizing the frequency-dependent, time-averaging dielectrophoretic force.

2.1.5 Effective Moment Calculation of Dielectrophoretic Force and Torque

The basis of the effective moment method is the hypothesis that the force and torque upon a particle can be expressed in terms of the effective moments identified from solution of the induced electrostatic field due to the particle. Consistent with this hypothesis, Eqs. 2.3 and 2.2 for the dipole force and torque take on the following time-dependent forms,

$$\overline{F}(t)_{DEP} = (\overline{p}_{eff}(t) \cdot \nabla) \overline{E}(t) \text{ and} \quad 2.18$$

$$\overline{T}(t) = \overline{p}_{eff}(t) \times \overline{E}(t). \quad 2.19$$

For a lossless dielectric particle of radius R and permittivity ϵ_2 immersed in a lossless dielectric fluid of permittivity ϵ_1 and subject to a nonuniform electric field, \overline{E} , the effective dipole moment evaluates from Eq. 2.5 and the Clausius-Mossotti evaluates from Eq. 2.6 to give the dielectrophoretic force as,

$$\overline{F}(t)_{DEP} = 2\pi\epsilon_1 R^3 \left(\frac{\epsilon_2 - \epsilon_1}{\epsilon_2 + 2\epsilon_1} \right) \nabla |\overline{E}|^2. \quad 2.20$$

See Appendix A and Pohl for a derivation of the above relation as this is the classic dielectrophoretic force calculation determined by Pohl [69].

For particles with ohmic loss, the dielectrophoretic force expression is given by,

$$\overline{F}(t)_{DEP} = 2\pi\epsilon_1 R^3 \text{Re}(\underline{K}) \nabla |\overline{E}|^2. \quad 2.21$$

The real part of the complex Clausius-Mossotti function as defined in Eq. 2.16 then determines the frequency dependence of the average dielectrophoretic force which in turn depends on the parameters of the particle and the suspending medium. The time-average electric torque is then defined as,

$$\overline{T}(t) = -4\pi\epsilon_1 R^3 \text{Im}[\underline{K}] \nabla |\overline{E}|^2. \quad 2.22$$

By proper substitution of Eqs. 2.11 and 2.12 into Eqs. 2.21 and 2.22, the more general force and torque equations accounting for dielectric loss are given by,

$$\overline{F}(t)_{DEP} = 2\pi\epsilon_1' R^3 \text{Re}[\underline{K}] \nabla |\overline{E}|^2 \text{ and} \quad 2.23$$

$$\overline{T}(t) = -4\pi\epsilon_1' R^3 \text{Im}[\underline{K}] \nabla |\overline{E}|^2. \quad 2.24$$

The dielectrophoretic force and torque equations as given in Eqs. 2.21 and 2.22 may be used with confidence as long as the dielectric loss in the suspension medium is negligible where negligible is defined as $\epsilon_1'' \ll \epsilon_1'$.

2.2 Generalized Definition for Dielectrophoresis

Incorporating the arguments of the preceding section, a compact equation describing the frequency-dependent, time-averaging dielectrophoretic force on a layered spherical particle with ohmic loss is given as,

$$\begin{aligned}\overline{F}(t)_{DEP} &= 2\pi\epsilon_1 R^3 \operatorname{Re}[\underline{K}] \nabla |\overline{E}|^2 \\ &= 2\pi\epsilon_1 R^3 \left[K_\infty - \frac{\Delta K_\alpha}{\omega^2 \tau_\alpha^2 + 1} - \frac{\Delta K_\beta}{\omega^2 \tau_\beta^2 + 1} - \dots - \frac{\Delta K_N}{\omega^2 \tau_N^2 + 1} \right] \nabla |\overline{E}|^2.\end{aligned}\tag{2.25}$$

The dielectrophoretic force equation in Eq. 2.25 reveals following four important principles [45]:

- \overline{F}_{DEP} is proportional to particle volume, R^3 ,
- \overline{F}_{DEP} is proportional to the dielectric permittivity of the medium in which the particle is suspended, ϵ_1 ,
- \overline{F}_{DEP} is directed along the gradient of the electric field intensity, $\nabla |\overline{E}|^2$, and
- \overline{F}_{DEP} magnitude and direction depend on the magnitude and sign of the real part of the complex Clausius-Mossotti function, $\operatorname{Re}[\underline{K}]$.

2.2.1 Clausius-Mossotti Function

The real part of the complex Clausius-Mossotti is frequency-dependent and determines the magnitude and direction of the dielectrophoretic force. This principle results in

interesting behavior for a particle that experiences ohmic and/or dielectric losses. Depending upon the frequency of the applied electric field, the particle will behave differently in the suspending medium. The behavior can be summarized as follows.

- Positive dielectrophoresis: $\text{Re}[\underline{K}] > 0$. Particles are attracted to electric field intensity maxima and repelled from minima.
- Negative dielectrophoresis: $\text{Re}[\underline{K}] < 0$. Particles are attracted to electric field intensity minima and repelled from maxima.

2.2.2 An Illustration of Frequency Dependent Dielectrophoresis

As an illustration of this phenomenon, the dielectrophoretic spectrum for a single-layered, dielectric particle with purely ohmic loss will be considered. The particle of permittivity and conductivity, ϵ_2 and σ_2 , suspended in a medium of permittivity and conductivity, ϵ_1 and σ_1 , has one relaxation process, τ_{MW} . It can be shown that the real part of the complex Clausius-Mossotti function reduces to

$$\text{Re}[\underline{K}] = \frac{\epsilon_2 - \epsilon_1}{\epsilon_2 + 2\epsilon_1} + \frac{3(\epsilon_1\sigma_2 - \epsilon_2\sigma_1)}{\tau_{MW}(\sigma_2 + 2\sigma_1)^2(1 + \omega^2\tau_{MW}^2)}. \quad 2.26$$

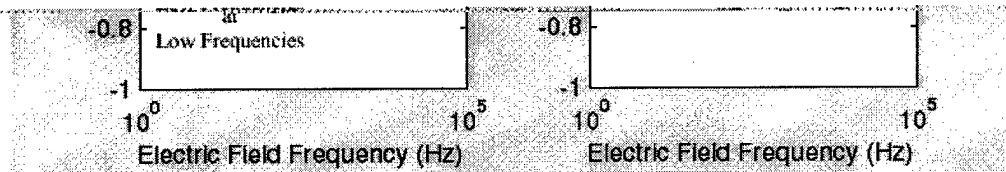
The relaxation time given in Eq. 2.26 is defined by,

$$\tau_{MW} = \frac{\epsilon_2 + \epsilon_1}{\sigma_2 + 2\sigma_1}. \quad 2.27$$

High and low frequency limits for $\text{Re}[\underline{K}]$ may be determined by examining the limit as the frequency goes to zero and to infinity.

$$\operatorname{Re}[\underline{K}] \rightarrow \begin{cases} \frac{\sigma_2 - \sigma_1}{\sigma_2 + 2\sigma_1}, \text{ for } \omega\tau_{MW} \ll 1 \\ \frac{\epsilon_2 - \epsilon_1}{\epsilon_2 + 2\epsilon_1}, \text{ for } \omega\tau_{MW} \gg 1 \end{cases} \quad 2.28$$

These two limiting cases are identified in Figure 2-2 where in Figure 2-2 (a) the condition $\epsilon_2/\epsilon_1 > 1$ and $\sigma_2/\sigma_1 < 1$ exists, and in Figure 2-2 (b) the condition $\epsilon_2/\epsilon_1 < 1$ and $\sigma_2/\sigma_1 > 1$ exists. These conditions may be representative of homogeneous dielectric spheres with ohmic loss.



ERROR: undefined
OFFENDING COMMAND: B

STACK:

$$\text{Re}[\underline{K}] \rightarrow \begin{cases} \frac{\sigma_2 - \sigma_1}{\sigma_2 + 2\sigma_1}, \text{ for } \omega\tau_{MW} \ll 1 \\ \frac{\epsilon_2 - \epsilon_1}{\epsilon_2 + 2\epsilon_1}, \text{ for } \omega\tau_{MW} \gg 1 \end{cases} \quad 2.28$$

These two limiting cases are identified in Figure 2-2 where in Figure 2-2 (a) the condition $\epsilon_2/\epsilon_1 > 1$ and $\sigma_2/\sigma_1 < 1$ exists, and in Figure 2-2 (b) the condition $\epsilon_2/\epsilon_1 < 1$ and $\sigma_2/\sigma_1 > 1$ exists. These conditions may be representative of homogeneous dielectric spheres with ohmic loss.

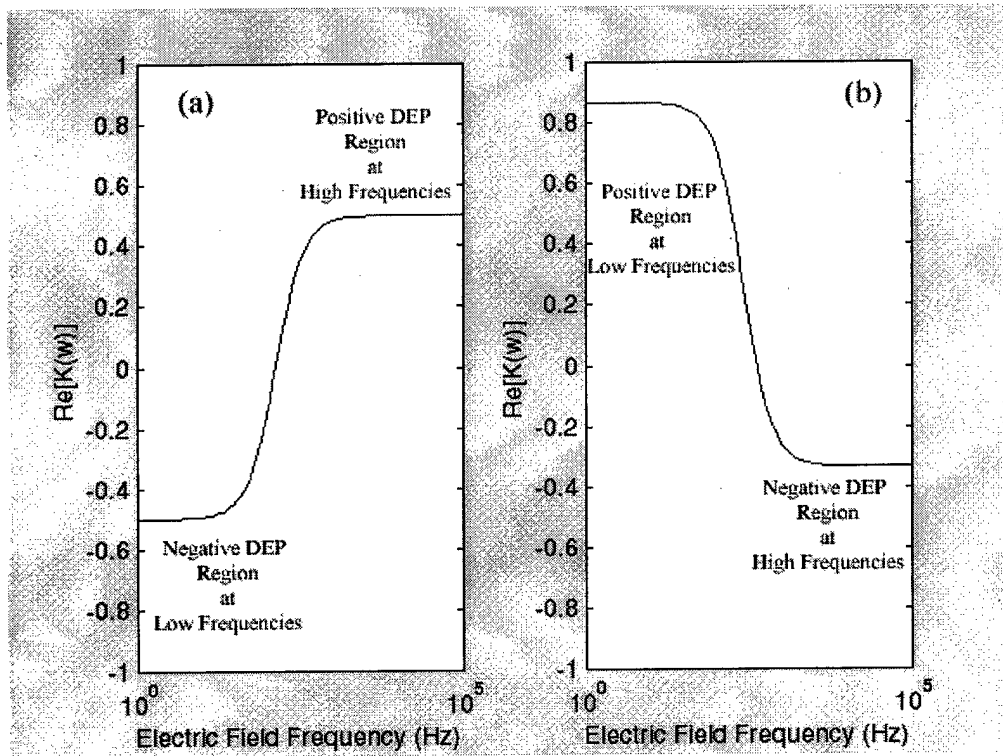


Figure 2-2 Clausius-Mossotti curve: (a) $\text{Re}[\underline{K}]$ plot for $\epsilon_1/\epsilon_0 = 2.5$, $\epsilon_2/\epsilon_0 = 10$, $\sigma_1 = 4 \cdot 10^{-8} \text{ S/m}$, and $\sigma_2 = 1 \cdot 10^{-8} \text{ S/m}$ (b) $\text{Re}[\underline{K}]$ plot for $\epsilon_1/\epsilon_0 = 10$, $\epsilon_2/\epsilon_0 = 2.5$, $\sigma_1 = 4 \cdot 10^{-8} \text{ S/m}$, $\sigma_2 = 1 \cdot 10^{-7} \text{ S/m}$ [45].

2.3 Dielectric Properties in General

Dielectric dispersion properties may be of use in separating biological macromolecules such as DNA or BSA or of use in sequencing different molecular weight DNA. An abundance of literature exists on the dielectric properties of biological macromolecules. While general trends concerning the frequency dielectric properties of these macromolecules is agreed upon, detailed data rarely agree between research groups. It is, therefore, important to understand how dielectric properties are measured. In this section, measurement methods of dielectric properties will be considered. An example dielectric dispersion curve will then be presented to explain important features of such curves. Dielectric dispersion curves for DNA and a common protein, bovine serum albumin (BSA), will then be presented to determine relevant dielectric properties that may be of use in separation and sequencing experiments.

2.3.1 *Methods for Measuring Dielectric Properties*

Devising methods to measure the dielectric properties of a biological solution consisting of the medium and the particle is not trivial. Grant et al. give an excellent characterization of dielectric measurement methods and the problems encountered when a broad frequency range is required [43]. In order to characterize a range of biological solutions by dielectric methods, an apparatus able to cover a very broad frequency range is required. A single apparatus or technique which can give the full required frequency coverage does not currently exist.

According to Grant, at the low frequency end of the spectrum, bridge techniques are used. Although these can in theory extend down to dc, practical measurements on conductive biological solutions are difficult below 1 kHz because of electrode polarization effects. At higher frequencies transmission lines are employed. Such techniques are subdivided into coaxial lines and waveguides. The frequency range of a coaxial line in practice is from around 50 MHz to 12 GHz. Above this and below 100

GHz waveguides are employed. Above 100 GHz, free space methods must be used, but these are relatively unimportant for biological solutions.

Of practical concern is the measurement of dielectric properties for biological solutions at low frequencies due to electrode polarization. Electrode polarization results from a formation of a layer of ions near to the electrodes that modifies the field distribution within the test solution. This phenomenon causes an increase in the measured capacitance. Because of this, it is difficult to generate a dielectric dispersion curve for biological solutions at frequencies below a few kHz. According to Grant, one method for alleviating electrode polarization is to deposit a layer of platinum black on the electrodes. Various calibration methods then can be employed to factor out the effect of electrode polarization on the measurement of dielectric properties.

The measurement of dielectric properties is further complicated by the fact that the imaginary contribution to complex permittivity resulting from ohmic and dielectric losses cannot be determined separately. In biological systems both effects are generally present, and it is impossible to separate the two contributions from measurements at one isolated frequency. Equations 2.11 and 2.12 can be modified to account for this dichotomy. The total measured frequency-dependent conductivity of the solution is lumped into a single term, σ , resulting from both the conductivity of the medium, σ_1 , and particle, σ_2 ,

$$\sigma = \sigma_1 + \sigma_2. \quad 2.29$$

The total frequency-dependent loss of the solution is defined as,

$$\epsilon'' = \frac{\sigma}{\epsilon_0 \omega} = \frac{\sigma_1 + \sigma_2}{\epsilon_0 \omega}. \quad 2.30$$

Solving Eq. 2.30 for the total loss due to the medium and the loss due to the particle and substitution of Eq. 2.29 yields,

$$\begin{aligned}
\varepsilon_1'' &= \frac{\sigma_1}{\varepsilon_0 \omega} \\
&= \frac{\sigma - \sigma_2}{\varepsilon_0 \omega} = \frac{\sigma}{\varepsilon_0 \omega} - \frac{\sigma_2}{\varepsilon_0 \omega} \\
&= \varepsilon'' - \frac{\sigma_2}{\varepsilon_0 \omega} \quad \text{and}
\end{aligned}
\tag{2.31}$$

$$\begin{aligned}
\varepsilon_2'' &= \frac{\sigma_2}{\varepsilon_0 \omega} \\
&= \frac{\sigma - \sigma_1}{\varepsilon_0 \omega} = \frac{\sigma}{\varepsilon_0 \omega} - \frac{\sigma_1}{\varepsilon_0 \omega} \\
&= \varepsilon'' - \frac{\sigma_1}{\varepsilon_0 \omega} ,
\end{aligned}
\tag{2.32}$$

respectively.

Equations 2.31 and 2.32 represent the total frequency-dependent loss due to ohmic and dielectric losses. Substitution of Eqs. 2.31 and 2.32 into Eqs. 2.11 and 2.12 results in new expressions for the complex permittivity of the medium,

$$\underline{\varepsilon}_1 = \varepsilon_1' - j\varepsilon_1'' , \tag{2.33}$$

and the complex permittivity of the particle,

$$\underline{\varepsilon}_2 = \varepsilon_2' - j\varepsilon_2'' . \tag{2.34}$$

2.3.2 An Illustrative Dielectric Dispersion Curve

Dielectric dispersion curves plot the real part of complex permittivity for the particle and medium, ε_1' and ε_2' , versus frequency. The real part of the complex permittivity is often referred to as the dielectric constant. Both terms can be used interchangeably. Gabler provides an excellent qualitative description of the important features of a dielectric dispersion curve as shown in Figure 2-3 [31]. According to Gabler, Figure 2-3 represents

the dielectric dispersion curve for a two-component system, particle and medium. The situation depicted assumes that both types of molecules in the solution are polar and that one is substantially larger in size than the other. This situation is representative of the case where a protein, or other biological macromolecule, is dissolved in water.

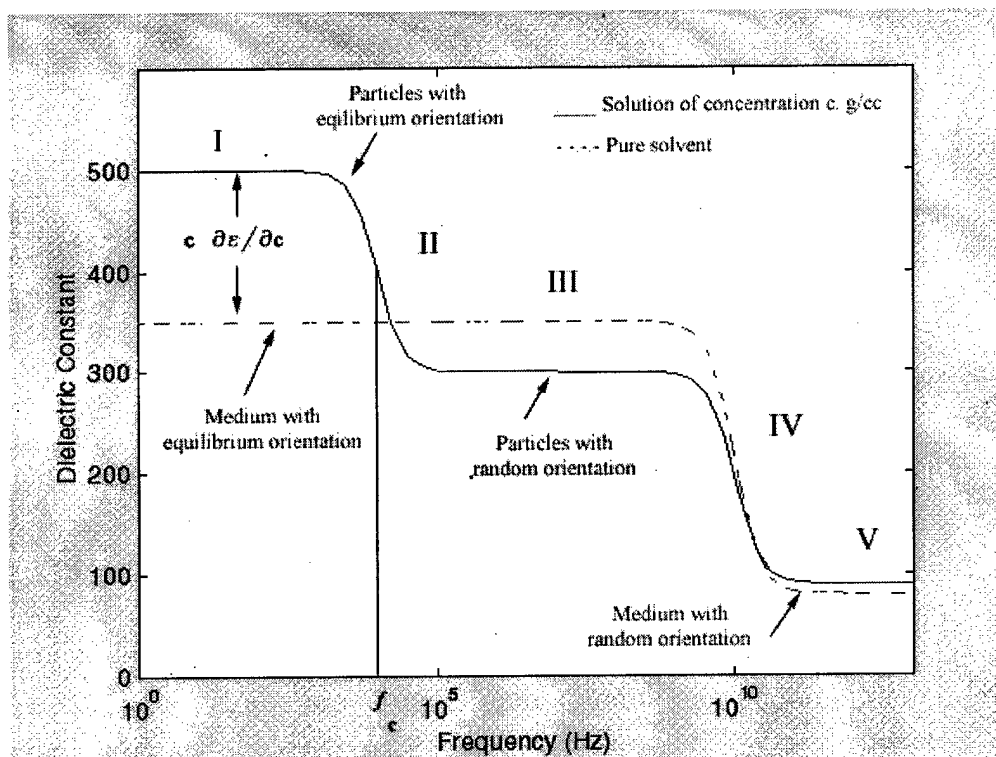


Figure 2-3 Dielectric dispersion curve for a two-component solution consisting of the particle suspended in a medium. The dielectric constant varies with the frequency of the applied field. As the frequency of the electric field increases, the effective dielectric constant decreases as the particle passes through different dispersion regions [31].

In Figure 2-3, the variation of the dielectric constant with frequency is divided into five general regions. These regions are qualitatively described as follows.

- Region I: At low frequencies of the field reversals, the larger biological macromolecules have sufficient time to reorient themselves in the alternating field. The retarding frictional forces acting on the biological molecules are small compared to the electrical orienting forces. The value of the dielectric constant is maximum.
- Region II: As the frequency of the field reversals increases, the effects of frictional forces are no longer negligible, and complete reorientation and equilibrium is not achieved by the larger macromolecules. As the frequency of the field increases, the dielectric constant decreases. This region of the curve is particularly interesting because the extent of the reorientation of the macromolecule is dependent upon the hydrodynamic properties of the macromolecule itself. This region of the curve is termed a region of dielectric dispersion when the dielectric constant falls from one value to another.
- Region III: At these frequencies the effects of frictional forces retarding the reorientation of the macromolecules have completely overwhelmed the electrical orienting forces, so the permanent dipoles of the macromolecules make no contribution to the dielectric constant. The solvent molecules, being very small, still achieve complete reorientation of their dipoles, and make the most significant contribution to the dielectric constant.
- Region IV: As the frequency of the field is further increased, another dispersion region is reached. Here the solvent molecules are beginning to lag the fluctuations of the field, and complete orientation of solvent dipoles is decreased so the dielectric constant again decreases.
- Region V: In this region, the field reversals are so fast that only the atomic distortions of induced dipoles can keep pace. The dielectric constant, therefore, is very small.

In Figure 2-3, the dielectric increment of the solution, $\partial\epsilon/\partial c$, is defined as a function of the dielectric constant of the medium, ϵ'_1 , and the dielectric constant of the solution, ϵ , according to,

$$\frac{\partial\epsilon}{\partial c} = \frac{\epsilon - \epsilon'_1}{c}. \quad 2.35$$

Equation 2.35 may be rewritten as,

$$\epsilon = \epsilon'_1 + \left(\frac{\partial\epsilon}{\partial c} \right) c. \quad 2.36$$

Equation 2.36 states that the dielectric constant of a solution is composed of two contributions: one from the medium and the other from the particle. The medium's contribution is represented by ϵ'_1 and the particle's contribution is dependent on its concentration, c . If the particle concentration is zero, then $\epsilon = \epsilon'_1$, and only the medium contributes to the dielectric constant. If the particle concentration changes the solution's dielectric constant, then $\partial\epsilon/\partial c$ multiplied by the particle concentration equals the increase in the dielectric constant of the solution over that of the pure medium.

Another useful parameter that can be determined from Figure 2-3 is a quantity called the relaxation time, τ_c . The relaxation time is a way of measuring how long it takes a molecule to reorient itself in a changing electric field. It is explicitly a function of molecular size and shape, and through inferred values of the relaxation time, that structural information is obtained from the dispersion regions. A larger or more extended molecule will take longer to change its orientation and so will have a larger relaxation time than will a small compact molecule. This relaxation time is different than the Maxwell-Wagner interfacial polarization relaxation time identified in Eq. 2.15 as this provides a theoretical estimate for the relaxation time. Here the relaxation time is that as defined by Debye and is determined from experimental data to occur at the critical frequency, f_c . The critical frequency, f_c , is defined as the frequency in the dispersion

region at which the dielectric constant is midway between the lower value, ϵ_∞ , and upper value, ϵ_0 . Debye described the shape the first dielectric dispersion region should take as,

$$\epsilon = \epsilon_\infty + \frac{\epsilon_0 - \epsilon_\infty}{1 + (f/f_c)^2}. \quad 2.37$$

The corresponding relaxation time at the critical frequency, f_c , is defined as,

$$\tau_c = \frac{1}{2\pi f_c}. \quad 2.38$$

For spherical particles, the relaxation time has quantitatively been expressed as,

$$\tau_c = \frac{4\pi\eta_v a^3}{k_B T}, \quad 2.39$$

where a is the sphere's radius, η_v the medium viscosity, k_B Boltzmann's constant, and T the absolute temperature. Equations describing the relaxation time for nonspherical particles have also been developed. In general, there will be two characteristic relaxation times for ellipsoids of revolution, one for rotation about each axis of symmetry.

2.4 Dielectric Properties of DNA

Takashima first determined useful dielectric properties of DNA [80-85]. An abundance of literature has been generated since Takashima by those seeking to understand the dielectric properties of DNA and, thereby, understand the physical charge structure of DNA [20, 23, 30, 32, 33, 50, 64, 73, 86-88, 91, 92]. While this literature agrees upon general trends in the dielectric dispersions of DNA, specific numbers such as relaxation times and dielectric increments are rarely in agreement. This is, in part, due to the problems discussed of devising a single appropriate apparatus to measure dielectric properties over a broad frequency spectrum. Differences also arise in experimental

parameters used such as DNA molecular weight, concentration, ionic strength, and temperature. Attempting to consolidate dielectric dispersions reported by various references is, therefore, challenging due to the number of factors in the process space. In general, developing dielectric dispersion curves require careful, repeatable methods and appropriate measurement equipment.

2.5 Contemporary Dielectric Model of DNA

This section will present a contemporary model of DNA that attempts to account for the observed dielectric dispersions of DNA. The general sensitivity of the dielectric dispersion to molecular weight, concentration, ionic strength, and temperature will also be discussed.

DNA undergoes two dielectric dispersions in the radio frequency range. Another dispersion is observed in the microwave frequency range, but this dispersion is attributed to the relaxation of water. Only radio frequencies are of importance in the investigation of DNA dielectric dispersion behavior. The low frequency dispersion occurs in Region II as the transition from Region I to Region III of Figure 2-3 and is termed the α dispersion. The high frequency dispersion occurs in Region IV as the transition from Region III to Region V of Figure 2-3 and is termed the β dispersion.

The counterion fluctuation model of DNA as developed by Mandel is generally well accepted and capable of accounting for the observed dielectric dispersions of DNA [50]. In this model, DNA behaves as a rigid-rod model whose dielectric effects are attributed to large, induced dipole moments originating in the distribution of strongly associated counterions around the macromolecule.

Minakata provides an excellent qualitative description of Mandel's counterion fluctuation model [55]. Polyelectrolytes are macromolecules having many ionizable groups. In aqueous solution a polyelectrolyte molecule dissociates into a polyion and a number of counterions. Major portions of the counterions are condensed to the polyion forming an

ionic atmosphere. These bound ions are relatively freely mobile in a domain around the polyion, under an external electric field, but their motion is substantially limited within this domain because of the strong attraction of the polyion. This limited movement of bound ions induces large polarizability of the polyion and is responsible for the large dielectric constant of the polyelectrolyte solution [55].

Mandel soon found this rigid-rod model to be inadequate because although it modeled the α dispersion well, it did not exhibit a β dispersion. He, in conjunction with van der Touw, later expanded the counterion fluctuation model to represent DNA as a flexible-rod comprised of a sequence of thin, rodlike subunits of identical length [87]. This model incorporates the possibility that the motion of the associated counterions along the chain may be characterized by two different relaxation times. A long relaxation time arises from counterion fluctuations over the complete macromolecule across all subunits while the shorter relaxation time arises from counterion fluctuations over only a limited number of the subunits. This implies that a fluctuation in the distribution of the associated counterions along the chain relaxes toward the equilibrium distribution in two steps.

- 1) A relatively slower process equilibrates the number of associated counterions between different subunits with a longer relaxation time leading to a uniform distribution of the counterions along the whole macromolecule. Here the α dispersion exists.
- 2) A process characterized by a shorter relaxation time that leads to a uniform distribution of the associated counterions along each subunit, but does not affect the number of counterions on each subunit. Here the β dispersion exists.

In the presence of a small external electric field, this uniform distribution is perturbed and gives rise to an induced dipole moment. This induced dipole moment is assumed to be responsible for the observed dielectric increment with respect to the dielectric increment of the medium which is not affected in this frequency range by the macromolecule.

Mandel developed equations for estimating the magnitudes of the observed dielectric increments in both dispersion regions [50]. In the low frequency α dispersion region, the dielectric increment is given by,

$$\alpha \text{ dispersion} \rightarrow \frac{\partial \epsilon}{\partial c} = \frac{e^2 \bar{f} N c \gamma S^2}{3 k T \epsilon_0}, \quad 2.40$$

and in the high frequency β dispersion region by,

$$\beta \text{ dispersion} \rightarrow \frac{\partial \epsilon}{\partial c} = \frac{e^2 \bar{f} N c \gamma b^2}{36 k T \epsilon_0}, \quad 2.41$$

where N is the total number of monovalent counterions of charge e per macromolecule, \bar{f} the average fraction of bound counterions, ϵ_0 the permittivity of free space, γ the ratio of the effective electric field acting on a macromolecule and the average Maxwell field in the solution, c the number of macromolecules per m^3 , and S the radius of gyration of the macromolecule. In Eq. 2.41, b^2 replaces S^2 where b is the length of one subunit.

Mandel additionally provided equations estimating the relaxation times in the α and β dispersion regions as,

$$\tau_\alpha^{-1} = \tau_r^{-1} + \tau_q^{-1}, \quad 2.42$$

$$\tau_r = \frac{\pi \eta_s L^3}{6 k T (\ln 2 p - 0.5)}, \text{ and} \quad 2.43$$

$$\tau_\beta = \frac{b^2}{\pi^2 k T u}, \quad 2.44$$

where: τ_r is the rotational relaxation time of prolate ellipsoids of revolution or cylindrical particles rotating about the short axis neglecting the flexibility of the chain, τ_q a relaxation parameter based upon the relaxation time of associated counterions between

subunits, η_s the viscosity of the medium, L the length of the macromolecule measured along its major axis for the ellipsoid, and $p = L/d$ with d the length of the minor axis or diameter of the cylinder. No theoretical estimate for τ_q fitting into the framework of the model is yet available.

2.6 Parameter Dependence of Dielectric Dispersion

It is generally accepted that DNA undergoes two dielectric dispersions in the radio frequency range: the α dispersion and the β dispersion. The α dispersion is very well characterized and exists at near dc up to around 1 kHz while the β dispersion has only recently received considerable interest and exists anywhere from tens of kHz up to a couple of MHz. The placement of these dispersions and associated dielectric increments within this frequency range depends upon various parameters such as molecular weight, concentration, ionic strength, and temperature. This section describes the dependence of the dispersion region on these parameters.

2.6.1 Molecular Weight

- *α Dispersion:* The α dispersion is strongly dependent upon molecular weight. The dielectric increment and relaxation time of DNA solutions increases with increasing molecular weight [80].
- *β Dispersion:* The β dispersion is generally independent of molecular weight [50].

2.6.2 Concentration

- *α Dispersion:* The α dispersion is strongly dependent upon concentration. The dielectric increment of DNA solutions increases with increasing concentration [86]. The relaxation time is not significantly dependent on the concentration [80].

- *β Dispersion:* The β dispersion is strongly dependent upon concentration. The dielectric increment and relaxation time of DNA solutions increases with increasing concentration [50].

2.6.3 Ionic Strength

- *α Dispersion:* The α dispersion is strongly dependent upon ionic strength. The dielectric increment and relaxation time of DNA solutions decreases with increasing ionic strength[80, 86].
- *β Dispersion:* The β dispersion is generally independent of ionic strength [50].

2.6.4 Temperature

- *α Dispersion:* The α dispersion is strongly dependent upon temperature. The dielectric increment of DNA solutions increases with increasing temperature [86]. The relaxation time is not significantly dependent on the temperature [86].
- *β Dispersion:* The β dispersion is generally independent of temperature [50].

2.6.5 Summary of Parameter Dependence

Table 2.1 shows a summary of the effects of various parameters on the observed dielectric dispersions of DNA.

Table 2.1 Summary of the dependence of the dispersion regions on various parameters.

A + sign indicates an increase in the in the parameter, a – sign a decrease, and an = sign indicates no significant effect.

Parameter	α Dispersion		β Dispersion	
	Dielectric Increment	Relaxation Time	Dielectric Increment	Relaxation Time
Molecular Weight (+)	+	+	=	=
Concentration (+)	+	=	+	+
Ionic Strength (+)	-	-	=	=
Temperature (+)	+	=	=	=

2.6.6 Dielectric Dispersion Curves for DNA

Because the α dispersion is strongly dependent on a host of parameters, it is not possible to depict one dielectric dispersion curve for DNA. Therefore, determination of the unique and relevant experimental parameters for anticipated experimental inquiry must match as closely as possible with the current available literature. Using the experimental parameters for this research of low concentration and ionic strength, high molecular weight, and at room temperature, Figure 2-4 was derived as the best fit estimate of anticipated behavior.

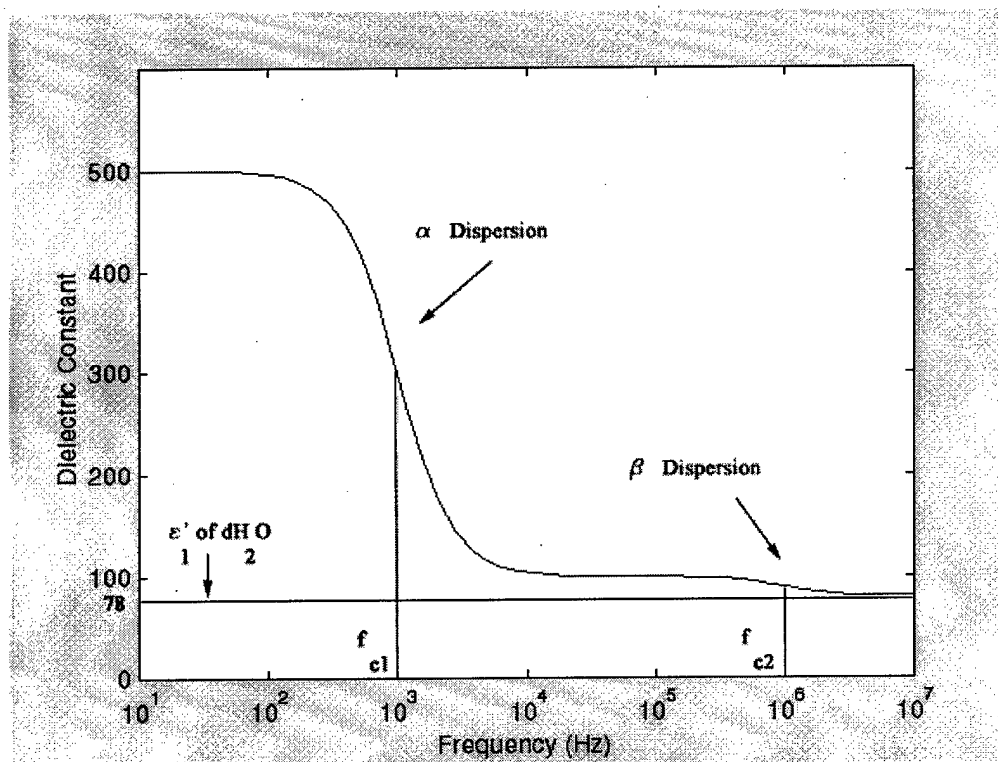


Figure 2-4 Possible dielectric dispersion curve of DNA used in this research at the appropriate molecular weight, concentration, ionic strength, and temperature.

Using Eqs. 2.37 and 2.38, DNA exhibits two relaxation times of approximately 0.15 ms and 0.15 μ s for the corresponding critical frequencies, f_{c1} and f_{c2} . The dielectric constant well exceeds that of deionized water (dH₂O) at low frequencies up to around 1 kHz approaching values of 500. DNA then enters the α dispersion and levels out to a dielectric constant value of approximately 100. The β dispersion is reached at approximately 1 MHz when the dielectric constant of DNA falls near that of dH₂O. Figure 2-4 depicts the dispersion curve for dH₂O as well for reference.

Using Eq. 2.6 as a first order approximation and assuming no ohmic or dielectric loss in the system, then the Clausius-Mossotti function, K , takes on the following values in different frequency ranges.

- Low Frequency (10^1 - 10^2 Hz): $\epsilon'_1 = 78, \epsilon'_2 = 500, K = 0.64$.
- α Dispersion (10^2 - 10^4 Hz): $0.64 \leq K \leq 0.086$.
- Mid-range Frequency (10^4 - 10^5 Hz): $\epsilon'_1 = 78, \epsilon'_2 = 100, K = 0.086$.
- β Dispersion (10^5 - 10^7): $0.086 \leq K \leq 0.0085$.
- High Frequency (10^7 - $10^{??}$ Hz): $\epsilon'_1 = 78, \epsilon'_2 = 80, K = 0.0085$.

The decreasing value of the Clausius-Mossotti function, K , with frequency shows that the dielectrophoretic force also decreases with frequency according to Eq. 2.20.

2.7 Dielectric Properties of BSA

Available literature on the dielectric properties of bovine serum albumin (BSA) is more sparse than that available for DNA [17-19, 27-29, 38, 41, 42]. The conclusions drawn from the available literature, however, are generally agreed upon in contrast to that for DNA. This section will present a contemporary model of BSA that accounts for the observed dielectric dispersions. A dielectric dispersion curve for BSA will then be shown and the parameter dependence of the dispersions discussed.

2.7.1 Contemporary Dielectric Model of BSA

Bovine serum albumin (BSA) is a globular, low-density lipoprotein (ldl). Essex et al. reported a five-component dielectric dispersion in BSA [29]. According to Essex et al., measurements of the dielectric properties of globular proteins in aqueous solution show the presence of three principal dispersions termed in order of occurrence the β , δ , and

γ dispersions. Note that the literature reports the first dispersion of BSA and other proteins as β instead of α as is the case with DNA. These dispersions take place over the respective frequency ranges of .01-10 MHz, 10 MHz-1GHz, and 1-100 GHz. BSA takes the form of a rigid spheroid of axial ratio 1:3 capable of rotating about both axes. This accounts for a double-component β dispersion termed β_1 and β_2 . A double-component δ dispersion, termed δ_1 and δ_2 , also exists where δ_1 is possibly due to proton fluctuation or to rotation of the side-chains projecting from the molecule. The δ_2 results from the relaxation of bound water. The γ dispersion results from the relaxation of free water.

2.7.2 Parameter Dependence of Dielectric Dispersion

Dielectric measurements of BSA are usually conducted at very high concentrations ranging from 55 mg/mL to 100.8 mg/mL. Unfortunately, little research has been performed to determine the parameter dependence of molecular weight, ionic strength, and temperature on the dielectric dispersion of BSA. The parameter dependence of concentration is similar to that of DNA. Increased concentration generally increases the dielectric increment of BSA and results in an increased relaxation time.

2.7.3 Dielectric Dispersion Curves for BSA

Frequencies of concern to this research are in the β dispersion region since this dispersion region occurs in the frequency range 0.01-10 MHz. Figure 2-5 shows a dielectric dispersion curve for BSA over the frequency range 1 Hz-10 M Hz. Unfortunately, no dielectric dispersion data exists for extremely dilute BSA solutions. Figure 2-5 corresponds to BSA at a concentration of 55 mg/ml.

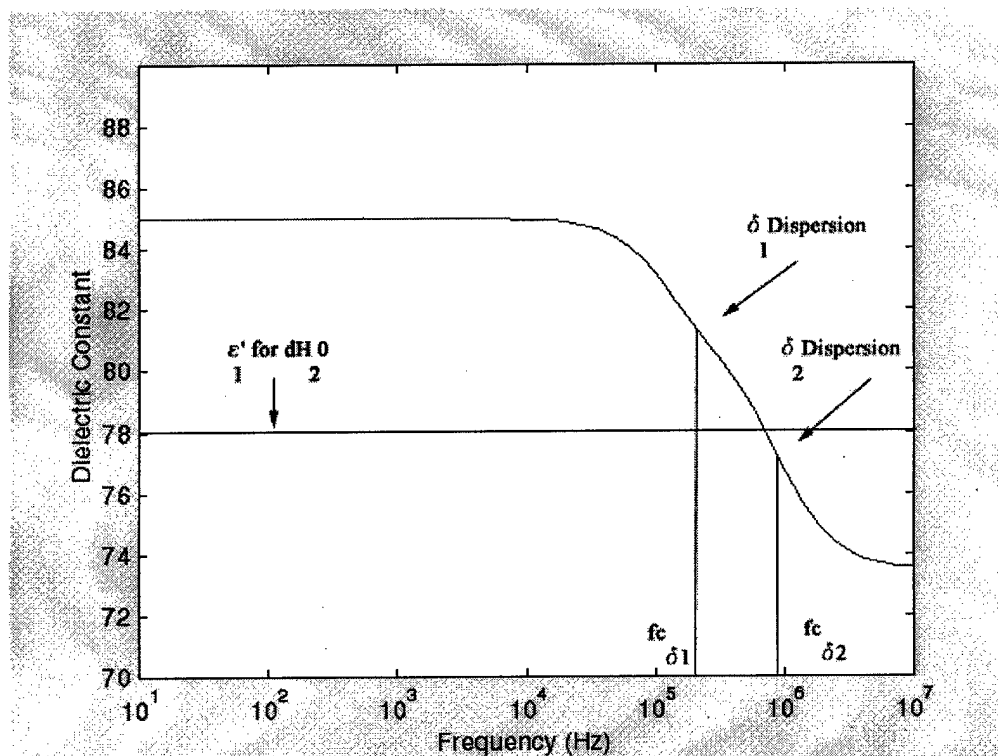


Figure 2-5 Possible dielectric dispersion curve of BSA used in this research.

Using Eqs. 2.37 and 2.38, BSA exhibits one general relaxation time of approximately $0.15 \mu\text{s}$ centered at 1 MHz in the β dispersion region. The dielectric constant just exceeds that of dH_2O at low frequencies up to around 100 kHz approaching dielectric constant values of around 90. BSA enters the β dispersion at approximately 100 kHz and levels out around 10 MHz reaching a dielectric constant of 73.5. Figure 2-5 depicts the dispersion curve for dH_2O as well for reference.

Using Eq. 2.6 as a first order approximation and assuming no ohmic or dielectric loss in the system, then the Clausius-Mossotti function, K , takes on the following values in different frequency ranges.

- Low Frequency (10^1 - 10^5 Hz): $\epsilon'_1 = 78, \epsilon'_2 = 90, K = 0.049$.
- β Dispersion (10^5 - 10^7 Hz): $-0.020 \leq K \leq 0.049$.
- High Frequency (10^7 - $10^{??}$ Hz): $\epsilon'_1 = 78, \epsilon'_2 = 73.5, K = -0.020$.

The decreasing value of the Clausius-Mossotti function, K , with frequency shows that the dielectrophoretic force also decreases with frequency according to Eq. 2.20. More importantly, the sign on K changes from positive to negative at around 1 MHz.

2.8 Summary

This chapter presented very fundamental and important theory concerning the dielectrophoretic force expression. It was shown that the dielectrophoretic force principally depends on $\text{Re}[\underline{K}]$ and $\nabla|\underline{E}|^2$. The most interesting dielectric behavior occurs when dielectric properties are frequency dependent and when losses, such as ohmic and dielectric losses, are present in the system. Under such circumstances, $\text{Re}[\underline{K}]$ can be negative or positive. When $\text{Re}[\underline{K}] < 0$, negative dielectrophoresis results. When $\text{Re}[\underline{K}] > 0$, positive dielectrophoresis results. This has important ramifications as will be shown in the next chapter through a survey of the available literature and will be shown in Chapters 5 and 6 through experimental results as observed in this research.

3 Related Work

The literature available in the field of dielectrophoresis is presented in this chapter. First, early electrode geometries as proposed by Pohl and Jones will be considered. Several dielectrophoretic separation schemes will be defined. Important work involving the determination of the electric field distribution for parallel array electrodes will be discussed. Various proposed applications of dielectrophoresis in biology will follow. The application of these proposed methods will be critiqued according to observed experimental results. Finally, uncertainties in the results obtained from these works will be described.

3.1 Early Pioneers in Establishing Conditions of Dielectrophoresis

Pohl and Jones' early work on the theoretical underpinnings of dielectrophoresis considered various electrode geometries for establishing highly nonuniform electric fields [46, 71]. They proposed electrode geometries that could be fabricated in the absence of thin-film, photolithography techniques available today. Some of their designs, accordingly, are not implemented in current research due to the proliferation of available microfabrication capabilities. Although their designs are not in use today, Pohl and Jones did establish some general principles that led to the development of microfabricated electrode arrays in use today.

3.1.1 Pohl

In formulating practical electrode geometries that produce dielectrophoretic forces, Pohl defined the dielectrophoretic force by,

$$\overline{F}_{DEP} = \frac{1}{2} \alpha \nabla |\overline{E}|^2, \quad 3.1$$

where: α is the effective polarizability, v the particle volume, \vec{E} the applied electric field vector, and ∇ the del operator. Using cylindrical coordinates (z, r, θ) , he rewrote Eq. 3.1 for the dielectrophoretic force in the radial direction, r , as,

$$F_{DEP} = k r^n. \quad 3.2$$

Assuming zero free charge throughout the volume of interest, $\nabla^2 V = 0$, no variation in the z direction, and for which a solution exists, r is given by,

$$r = r_{\theta 0} \left[\sin \left(\frac{n+3}{2} \theta \right) \right]^{\frac{-2}{n+3}}, \quad 3.3$$

where $r_{\theta 0}$ is a characteristic radial distance defined as the minimum distance from the coordinate center to the electrodes.

The relevant parameter in Eqs. 3.2 and 3.3 is n because the dielectrophoretic force varies as r^n .

The value of n in Eq. 3.2 can take on different values which correspond to different electrode geometries as shown in Figure 3-1 having the shape primarily of cylindrical geometry. Examples of cylindrical geometries are a central wire held coaxially within an outer cylindrical electrode similar to a coaxial capacitor, a wire-plate combination with two components parallel, and a wire-wire electrode made of parallel wires.

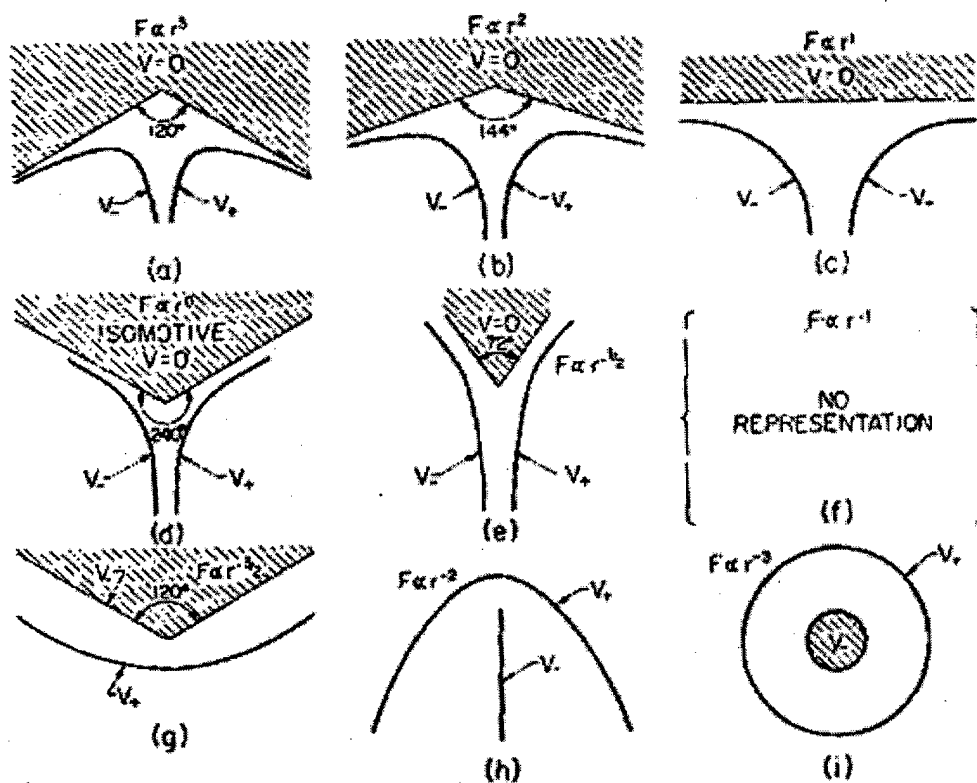


Figure 3-1 Electrode geometries corresponding to different values of n [71].

For $-1 < n \leq 3$, the system has two electrodes to which V_+ and V_- are applied and one ground. For $-3 \leq n < -1$, the system has two electrodes to which V_+ and V_- are applied. The case, $n = -1$, leads to a trivial solution because it requires $|\vec{E}|^2 = 0$ and leads $\vec{F}_{DEP} = 0$ everywhere. Pohl characterized the case of $n = 0$ as an isomotive field configuration in which the dielectrophoretic force on the particles is independent of its position within the electrode volume and, therefore, has applications in particle separations [71]. This configuration is shown in Figure 3-2. The important result from Pohl's work is that electrode geometry effects the dielectrophoretic force.

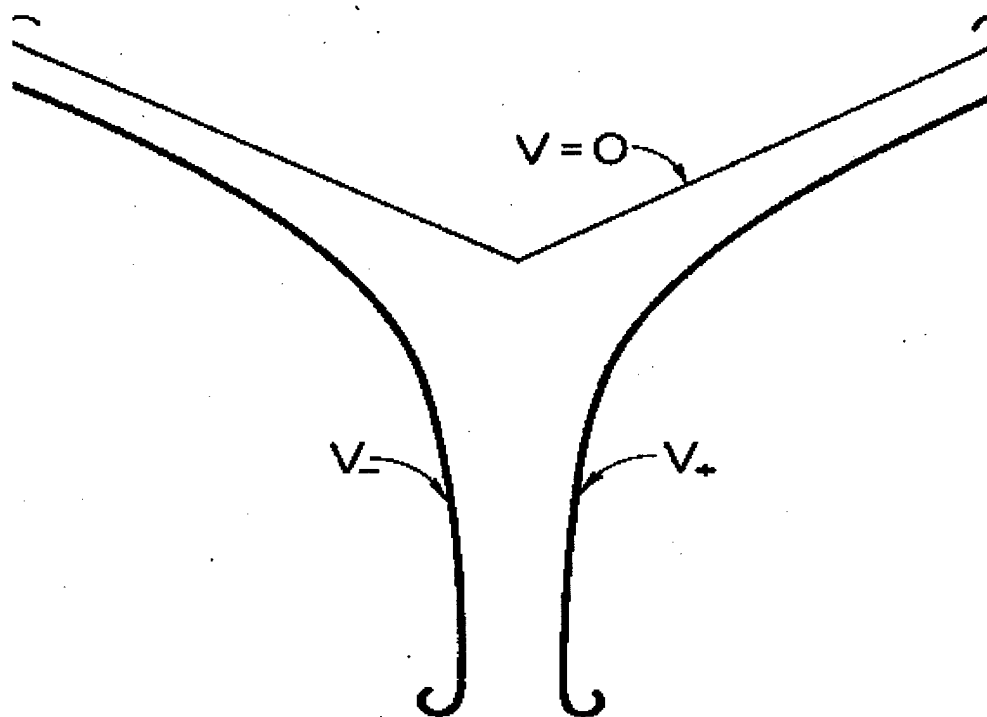


Figure 3-2 Sketch of a practical design for electrodes producing an isomotive dielectrophoretic force field. The electrodes are drawn with care to permit guidance in crafting copies. In use with ac voltage supplies, the ground electrode would connect with the center-tap of the transformer [71].

3.1.2 Jones

Jones experimented with ring-plane electrode designs for dielectrophoretic levitation of gas bubbles in a dielectric liquid of known dielectric constant and density [46]. Dielectrophoretic levitation is characteristic of particles undergoing negative dielectrophoresis in competition with a restoring force such as gravity. He realized the nonuniformity of an electrostatic field was highly dependent on the configuration and shape of the electrodes which establish the field and devised a scaling law that revealed the magnitude of the dielectrophoretic force on a particle can be increased by reducing the electrode dimensions [45]. This scaling law is given as,

$$|\overline{F}_{DEP}| \propto \frac{V^2}{L_e^3}, \quad 3.4$$

where V is the applied voltage and L_e is the characteristic electrode length. The characteristic electrode length, L_e , in a ring-plane electrode system refers to the distance of separation between the electrode ring and the plane electrode.

For example, if the dimensions of an electrode are reduced by a factor of 2, then the required voltage is reduced by a factor $2^{3/2}$. An example of a ring-plane electrode design and associated test chamber used by Jones is shown in Figure 3-3. The important result from Jones' work is that electrode dimension effects the dielectrophoretic force.

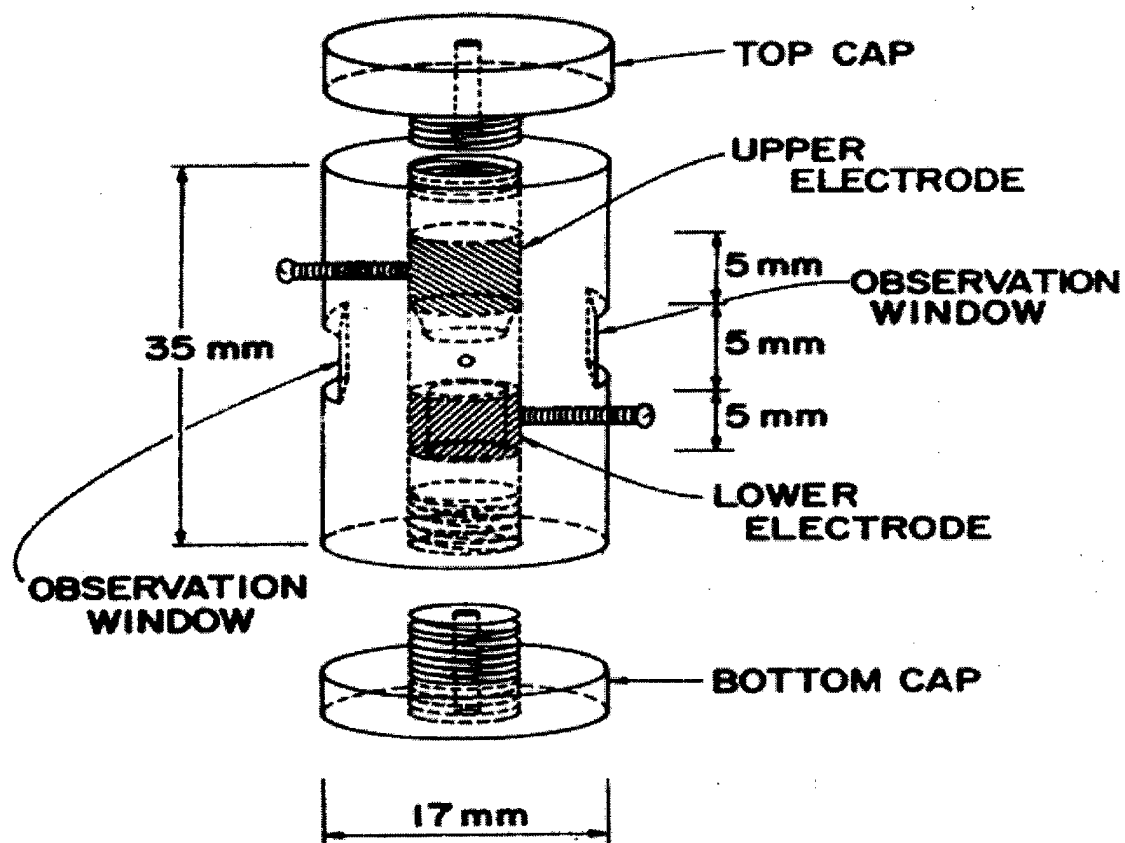


Figure 3-3 Experimental test cell used by Jones with interchangeable axisymmetric electrode shapes [46].

3.2 Proposed Dielectrophoretic Separation Methods

One principle application for dielectrophoresis is the separation of biological macromolecules such as DNA and BSA and also the sequencing of different molecular weight DNA. Three separation methods are envisioned and in some cases have been demonstrated: dielectrophoretic retention, dielectrophoretic migration, and dielectrophoretic/gravitational field-flow fractionation (DEP/G-FFF). Each method has advantages and disadvantages depending on the particle and medium in question as well as the desired results. Recently, DEP/G-FFF has received considerable attention due to its potential for distinguishing between particles with very similar dielectric properties. This section will describe these three different methods.

3.2.1 Dielectrophoretic Migration

Dielectrophoretic migration exploits opposing polarities of the dielectrophoretic forces exerted on different particle types, so that one type is attracted towards high field regions by positive dielectrophoresis while the other type(s) are repelled by negative dielectrophoresis. In this way, different particles types are focused at different regions of a microelectrode structure and spatial separation is achieved [44].

3.2.2 Dielectrophoretic Retention

Dielectrophoretic retention describes a configuration where the dielectrophoretic force holding a particle exceeds the fluid-flow shear forces tending to release the particle. Particles experiencing a sufficiently weak dielectrophoretic force (negative or small positive) are eluted by fluid flow, whereas, particles experiencing sufficiently strong positive dielectrophoretic forces are trapped at electrode edges [44].

3.2.3 Dielectrophoretic/Gravitational Field-Flow Fractionation

Both dielectrophoretic migration and retention methods depend upon there being relatively large differential dielectrophoretic forces between the particle types being sorted [44]. DEP/G-FFF overcomes these limitations to some degree.

Field-flow fractionation refers to a general class of particle separation methods that exploit the velocity gradient of a hydrodynamic flow profile within a chamber. A force is applied perpendicularly to this velocity gradient to place the particle at various positions within this flow profile. The position within the flow profile determines the elution time.

Three FFF modes exist and are distinguished by the applied perpendicular force. In normal mode, the perpendicular force pushes the particles towards the wall of the chamber where they form concentration patterns characterized by the competition between the applied force and diffusion/Brownian motion. Different particles will have different concentration patterns. The concentration pattern determines the elution time resulting from the flow profile. Smaller particles generally elute sooner than larger particles. In the second mode, the perpendicular force is so strong that it pushes the particles to the wall. The flow velocity is minimal near the wall. Larger particles will experience larger drag forces and, thereby, be eluted sooner than smaller particles. In the third mode, the applied force is such that it balances with the hydrodynamic lift force and so places the particles at some equilibrium position within the flow profile. Different particles will be positioned at different heights within the flow profile, and this then determines the elution time.

The applied perpendicular force can be generated in a variety of ways. DEP/G-FFF uses the dielectrophoretic force as the perpendicular force. In this manner, particles with different complex permittivities will experience different dielectrophoretic forces under application of different electric fields. The force the particle feels will determine the position within the flow profile. The position in the flow profile then determines the elution time with those particles near the center of the flow profile eluting more quickly than those particles near the edges of the flow profile.

3.3 Dielectrophoretic Methods Applied to Cells and Microbeads

3.3.1 *Davis and Giddings*

Davis and Giddings first studied the feasibility of DEP/G-FFF with flow chambers that negated the effects of gravity [25]. They envisioned using a coaxial capacitor as the flow chamber due to its ease of fabrication and well characterized electric field distribution. The coaxial capacitor is similar to what Pohl proposed in Eq. 3.2 where $n = -3$ with the electrodes serving as the walls of the chamber. In this manner, particles undergoing positive dielectrophoresis would be attracted to the chamber core where the electric field is maximum while particles undergoing negative dielectrophoresis would be attracted toward the chamber wall where the electric field is minimum. An induced flow within this chamber would then elute particles at different times according to their equilibrium positions within the flow profile. They concluded that the dielectrophoretic force would be strong enough to retain and separate ultrahigh-molecular-weight polymers and submicron-diameter particles dissolved or suspended in organic liquids of high dielectric constant.

3.3.2 *Gascoyne, Wang, Huang, and Yang*

Gascoyne et al. examined dielectrophoretic separation techniques ranging from dielectrophoretic migration to dielectrophoretic/gravitational field-flow fractionation. They contributed considerably to describing the electric field distribution for parallel array electrodes. Recently they implemented a dielectrophoretic/gravitational field-flow fractionation device to separate particles based upon particle size and dielectric properties. Both cells and microbeads were examined [118].

Gascoyne's early work concentrated on determining electric field distributions for interdigitated, parallel array electrodes [40]. He demonstrated the separation of mammalian cells according to their dielectric properties under suitable choices of applied electric field and cell suspension medium. The mammalian cells used in his studies were normal murine erythrocytes and murine erythroleukemia cells. At low frequencies, both

cell types exhibited negative dielectrophoresis due to $\text{Re}[\underline{K}] < 0$. At high frequencies, both cell types exhibited positive dielectrophoresis due to $\text{Re}[\underline{K}] > 0$. At an intermediate frequency, of 22 kHz, normal murine erythrocytes cells exhibited $\text{Re}[\underline{K}] < 0$ while the murine erythroleukemia cells exhibited $\text{Re}[\underline{K}] > 0$. He subsequently collected normal murine erythrocytes cells in the minimum field regions of his interdigitated, parallel array electrode device while collecting murine erythroleukemia cells in the maximum field regions. Figure 3-4 shows Gascoyne's device and the collection patterns of murine erythroleukemia cells at low and high frequencies.

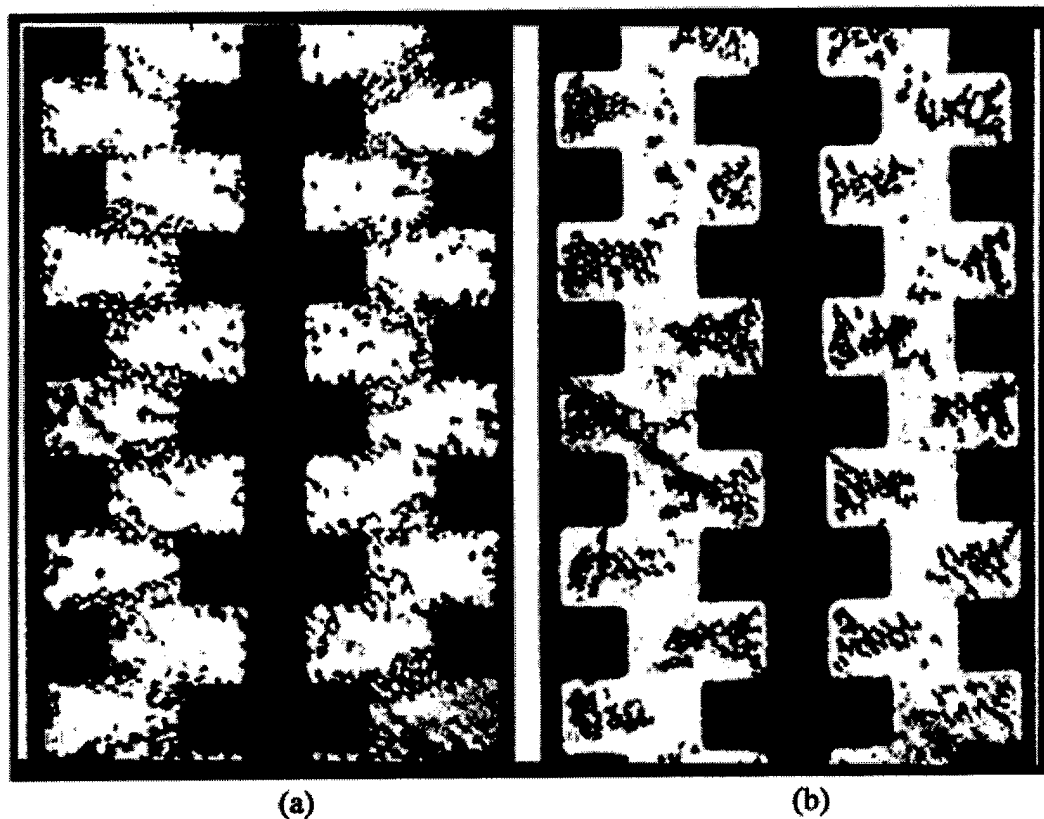


Figure 3-4 Positive and negative dielectrophoretic collection regions: (a) Murine erythroleukemia cells at 100 kHz where $\text{Re}[\underline{K}] > 0$ and positive dielectrophoresis occurs (b) Murine erythroleukemia cells at 1 kHz where $\text{Re}[\underline{K}] < 0$ and negative dielectrophoresis occurs [40].

To understand this cell collection phenomenon, Gascoyne also determined the electric field distribution of his device in the plane of the electrodes as shown in

shows that the maximum value of $\nabla|\overline{E}|^2$ occurs at the tips of the electrodes while the minimum value of $\nabla|\overline{E}|^2$ occurs in the bay regions.

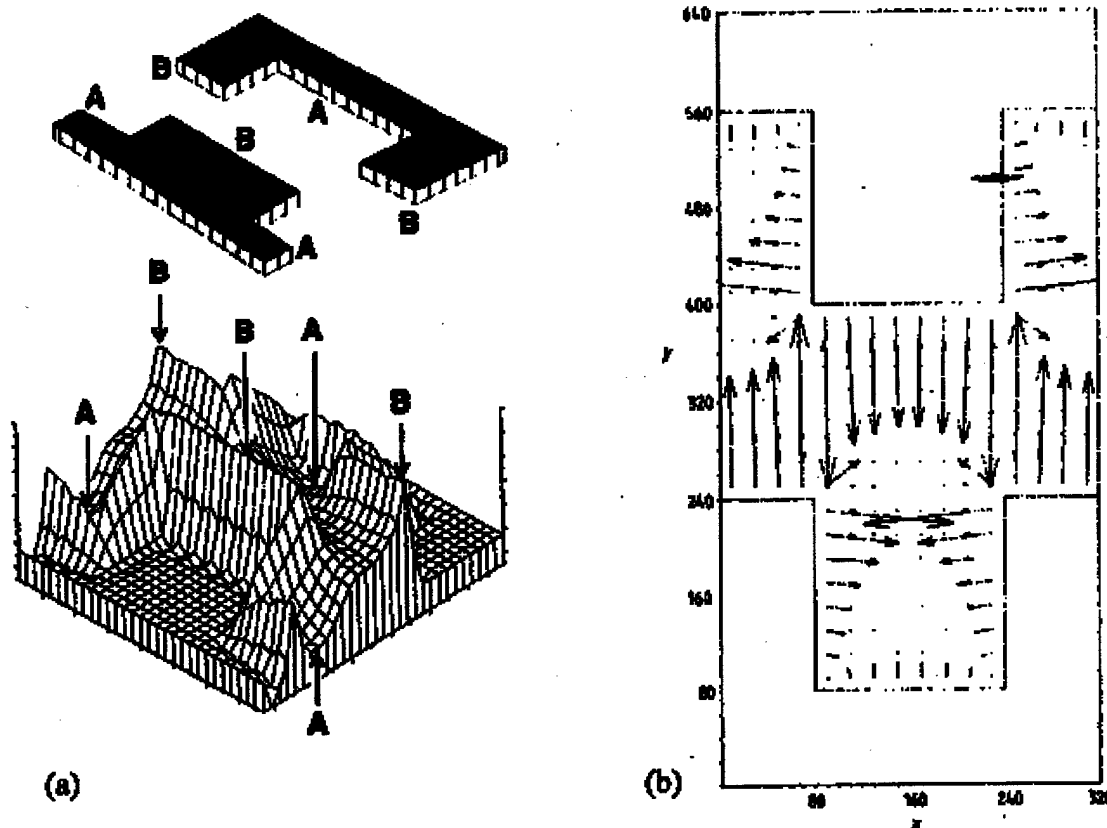


Figure 3-5 Electric field distribution: (a) The electric field distribution (vertical axis) for one segment of the periodic interdigitated electrode array. Points labeled A correspond to minima of $\nabla|\overline{E}|^2$ whilst those labeled B correspond to maxima. (b) A plot of the dielectrophoretic force parameter $\nabla|\overline{E}|^2$ for negative dielectrophoresis for the interdigitated electrode [40].

Gascoyne used similar techniques to demonstrate the separation of normal cells from cancerous cells and the separation of cancer cells from blood [36, 37, 39]. He also influenced the work of Wang and many others in this field [94-99, 101].

Wang in conjunction with Gascoyne attempted to more accurately and more simply derive the field distribution using Green's Theorem [93]. Accurate determination of the electric field distribution for a parallel array electrode or any similar planar electrode geometry is of considerable importance. The field distribution near the electrode edges is poorly understood. According to Wang, the Green's Theorem based method has many advantages over numerical solutions for the following reasons:

- 1) Depending on the complexity of the electrode geometry, analytical expressions may be obtained not only for the potential distribution but also for the electric field and the time-averaged dielectrophoretic force, circumventing the need for numerical differentiation.
- 2) Accurate field and dielectrophoretic force determinations can be made right up to the electrode plane and the electrode edges.
- 3) The approach is computationally much more efficient than numerical techniques.

Critical assumptions in the Green's Theorem based method include the following.

- 1) Overall dimensions of planar electrode array are much larger than the cell size and the height of cells above the electrode plane so that the array can be treated as being infinitely large.
- 2) The frequency of the applied field is sufficiently low that the near field approximation is valid.
- 3) Electrode polarization is negligible.

A graphical illustration of $\nabla|\overline{E}|^2$ near the electrode plane is shown in Figure 3-6.

Examination of the vector field reveals that:

- 1) $\nabla|\overline{E}|^2$ always points towards the strong field regions. At heights about one half of the electrode width,
- 2) $\nabla|\overline{E}|^2$ is dominated by its vertical component, pointing towards the electrode plane, and its amplitude decays with increasing distance from the electrode plane. Close to the electrode surface, however,
- 3) $\nabla|\overline{E}|^2$ points towards the electrode edges.

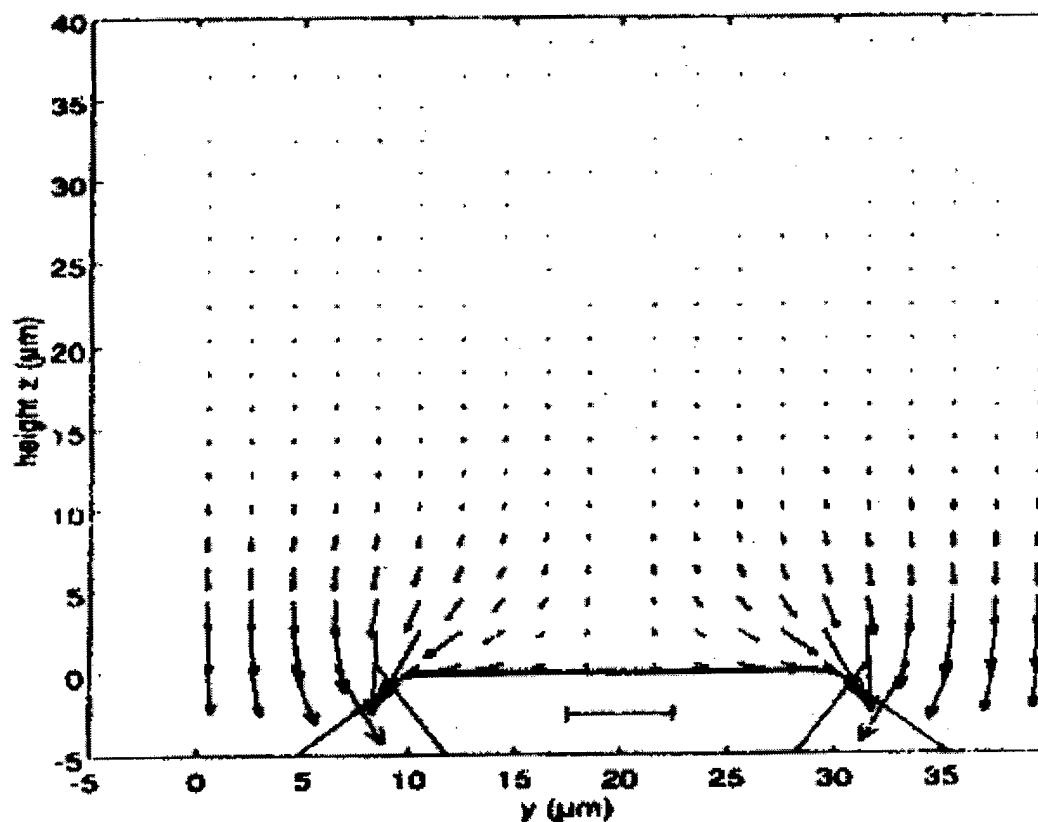


Figure 3-6 Vector representation of $\nabla|\underline{E}|^2$ [93].

Furthermore, when $\text{Re}[\underline{K}] > 0$, a positive dielectrophoretic force results pulling particles down towards the electrode plane and trapping them at the electrode edges. On the other hand, when $\text{Re}[\underline{K}] < 0$ a negative dielectrophoretic force results directing the particles upwards, levitating them, or else causing them to collect at the central regions of either the electrodes or the gaps between them.

Recently Gascoyne et al. implemented a dielectrophoretic/gravitational field-flow fractionation device to separate cells and polystyrene microbeads [44, 100, 118]. Unlike Davis and Giddings, they fabricated parallel array electrodes using thin film

photolithography techniques. A general schematic demonstrating the concept of dielectrophoretic/gravitational field-flow fractionation is shown in Figure 3-7. It was determined that separation of cells and polystyrene beads was based on the differences in their effective dielectric properties. Particles possessing different dielectric properties were positioned at different heights in a fluid-flow profile in a thick chamber by the balance of dielectrophoretic and gravitational forces, transported at different velocities under the influence of the fluid flow, and thereby separated. It was also concluded that the dielectrophoretic force was the dominant factor in controlling particle equilibrium height and the hydrodynamic lift force played little role in dielectrophoretic/gravitational field-flow fractionation [100].

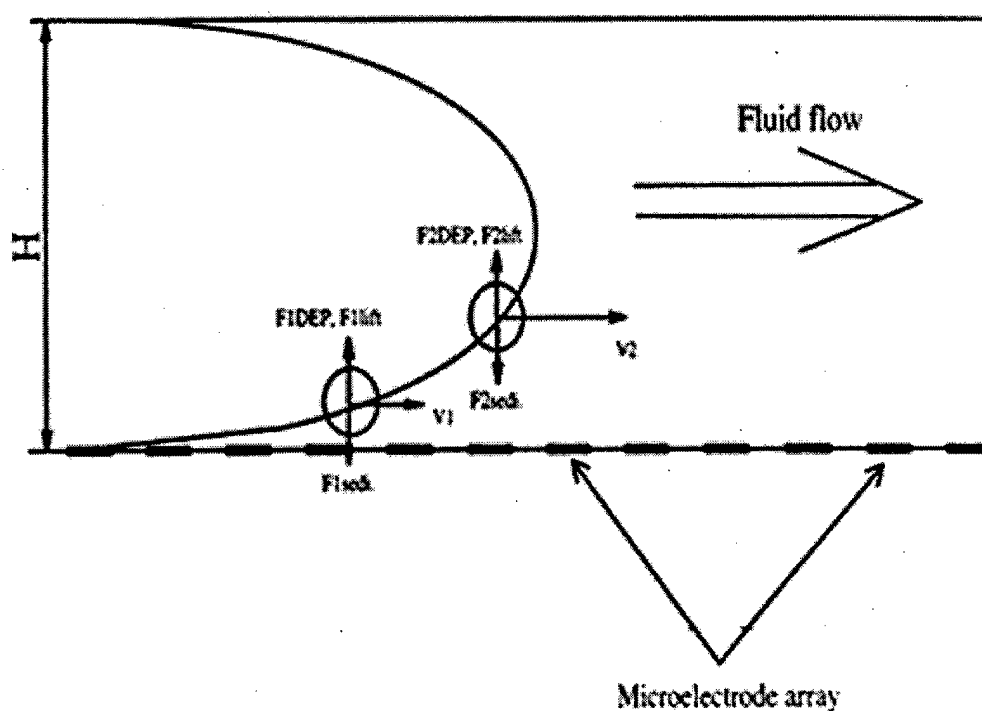


Figure 3-7 DEP/G-FFF system. A fluid profile is established in a thin chamber whose bottom plane supports a microelectrode array. Two particles of different dielectric properties equilibrate at different heights under the balance of DEP levitation, hydrodynamic lift, and sedimentation forces. Particle 2, being levitated further away from the chamber wall exhibits a larger velocity under the influence of fluid drag than particle 1 [44].

Yang further prescribed the potential biomedical applications of dielectrophoretic/gravitational field-flow fractionation [118]. According to Yang, the dielectrophoretic/gravitational field-flow fractionation can be readily implemented in microfluidic systems for processing cell samples in the volume range of nanoliters to microliters. The only issue associated with miniaturization is that the chamber has to be long enough to provide sufficient resolution for the desired cell separation. The miniaturization of DEP/G-FFF device can be interfaced to other microfluidic components including microscale polymerase chain reactions (PCRs), capillary electrophoresis

devices, cell counters, and electrochemical detectors. The capability of DEP/G-FFF separation according to density properties suggests that it can be used in integrated microfluidic systems as a substitute for centrifugation, which is currently used as a basic step in cell sample preparation.

3.4 Dielectrophoretic Methods Applied to Biological Macromolecules

The work of Gascoyne et al. exclusively involved the separation of comparatively large particles ($>1\ \mu\text{m}$) compared to that of biological macromolecules such as DNA or bovine serum albumin (BSA). Little work has been conducted in applying dielectrophoretic principles towards manipulation of these macromolecules. With increasing availability of microfabrication capabilities, however, fabricating microelectrical devices has become routine. Currently, only two groups have worked considerably with dielectrophoresis and its application towards manipulation of biological macromolecules such as DNA and BSA, Washizu and Asbury and van den Engh. Ajdari and Prost first considered separation on purely theoretical grounds.

3.4.1 *Ajdari and Prost*

Ajdari and Prost envisioned a free-flow electrophoresis device capable of selectively separating biological macromolecules such as DNA and large proteins [1]. A free-flow electrophoretic drift field would move particles across an oscillating transverse field generated by a simple parallel electrode array serving as a dielectric trap. A dielectrophoretic force induced by periodic intervals of dielectric traps would then draw particles out of the free-flow electrophoretic drift and lead to separation. They predicted trapping times would depend exponentially on the particle polarizability. In their feasibility study, they formulated the problem as follows: a Brownian particle under constant drift is trapped at periodic intervals in identical traps. On purely theoretical grounds, they hypothesized that 1 megabase pair (Mb) fragments of DNA differing by 10 kilobase pairs (10 kb) would lie in two separated bands, $\sim 2\ \text{mm}$ apart after 1 hour, whereas, the same result would typically require 100 hours with usual pulsed-field gel

electrophoresis devices. They also discussed a few critical limiting factors in this theoretical development.

- 1) Reduced separation selectivity due to idealization of electric field pattern,
- 2) Reduced separation selectivity due to onset of convection currents due to heating, and
- 3) Reduced separation selectivity due to induced conformational changes of the macromolecule.

3.4.2 *Washizu*

The volume of available literature by Washizu certainly illustrates his acumen in the field of dielectrophoresis as it relates to biological macromolecules [102-116]. Washizu fabricated a device he termed a fluid integrated circuit (FIC) to carry out his investigations of dielectrophoretic micromanipulation of cells and biological macromolecules. His early work involved manipulation of cells with his FIC serving as a cell shift register and cell deflector [113]. In the cell shift register, he demonstrated storage and one by one transport of cells without the aid of fluid flow. In the cell deflector, he simulated a deflection plate in a cell sorter that deflects cells fed from the inlet to either of two outlets. In his work with the FIC, Washizu primarily used electric field settings on the order of 10^6 V/m at frequencies of 1 MHz.

Washizu eventually applied the FIC concept to dielectrophoretic micromanipulation of DNA [109, 110]. He envisioned various applications that fall under a general category that he termed electrostatic stretch-and-positioning of DNA. These stretch-and-position methods were thought to be useful for:

- Size determination of stretched DNA where the length of DNA stretched to its full length could be measured,
- Measurement of nuclease activity,

- Electrostatic immobilization of DNA, and
- DNA sequencing where stretched DNA strands could be cut into small pieces and successively subcloned and sequenced by conventional methods.

Electrostatic stretch-and-positioning of DNA is accomplished in the following manner. A DNA molecule, randomly coiled under the absence of the electrostatic field, is stretched straight along the field lines. Using vacuum-evaporated parallel strip electrodes with sharp edges, the stretched DNA is attracted to the electrode edge where the field is stronger by dielectrophoresis until one end of the molecule touches the electrode edge, while the other end extends perpendicular to the other electrode. Washizu observed permanent fixation of DNA to the electrodes at these high electric field strengths and frequencies.

Washizu primarily used electric field settings on the order of 10^6 V/m at frequencies of 1 MHz in his FIC device. He also observed unexplained phenomenon using electric fields at lower frequencies than 1 MHz. Between frequencies of 0.1 to 2 MHz, he observed orientation of the DNA strand along electric field lines. When he switched the frequency stepwise from high frequency to 40 kHz, the DNA strand oriented perpendicularly to electric field lines. If a 40 kHz signal was applied from the beginning, he observed a meshlike or wavelike pattern that was not distinguishable as perpendicular orientation.

Washizu explained this phenomenon as possible saturation in the polarization as frequency is lowered in the following manner. According to Washizu, under conditions where DNA has a high dipole moment along its length, the orientation of DNA should be parallel to the field. The occurrence of perpendicular orientation suggests that the axial orientation is no longer dominant.

Washizu also envisioned various separation routines characteristic of dielectrophoretic retention that he termed dielectrophoretic chromatography for the dielectrophoretic separation of biological macromolecules using the FIC [114]. He observed that high molecular weight DNA with a subsequently higher polarization was more easily trapped

than that of lower molecular weight with reduced polarizability. Therefore, with the proper choice of excitation voltage, two or more types of DNA are separated. Trapped DNA are then recovered at the outlet of the flow chamber after the removal of the excitation voltage.

Washizu also applied the FIC concept to dielectrophoretic micromanipulation of BSA [114]. He observed that dielectrophoresis of 13-16 kD proteins occurs under a 10^6 V/m electric field in a frequency range from 1 kHz to 10 MHz. Furthermore, he qualitatively mapped the frequency and voltage ranges into regions of induced bubble formation and into dielectrophoretic and non-dielectrophoretic regions as shown in Figure 3-8. Washizu also investigated the dependency of trapping ability on electrode gap dimensions of 55 μm , 15 μm , and 4 μm . He determined that under a 1 MHz field, threshold voltages for dielectrophoresis were 40 V for a 55 μm gap, 15 V for a 15 μm gap, and 6 volts for a 4 μm gap.

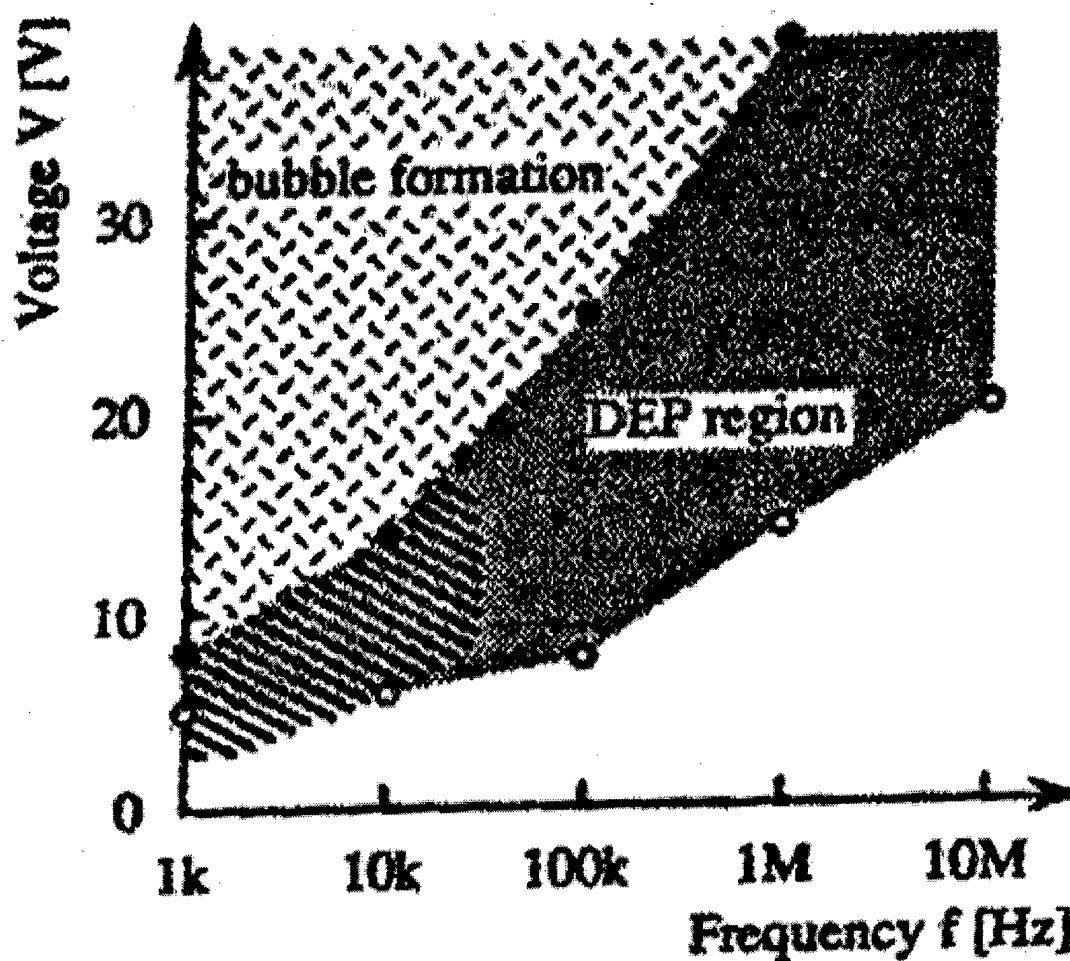


Figure 3-8 Regions of dielectrophoresis for avidin in the frequency-voltage plane determined from microscope observations [114].

3.4.3 Asbury and van den Engh

Asbury and van den Engh also recently investigated dielectrophoretic manipulation of DNA. They fabricated a device similar to Washizu's FIC [2, 3]. Asbury and van den Engh, however, investigated the response of DNA in the presence low electric field strength and low frequency compared to those settings used by Washizu. They used trapping signals typically between 0.5-4 V_{p-p} resulting in a threshold field strength around

10^5 V/m and at frequencies below 2 kHz compared to typical settings used by Washizu of 10^6 V/m and 1 MHz. Asbury and van den Engh observed that increasing frequency required increasing application of voltage until at 2 kHz the trapping potential could not overcome viscous drag that resulted from unintended fluid flow within his flow chamber. Optimal settings as determined by Asbury and van den Engh were a 3 V_{p-p} signal at 30 Hz resulting in a threshold field strength of 10^5 V/m.

Asbury and van den Engh also investigated the parameter dependence of trapping on DNA molecular weight and ionic strength as determined by the concentration of Tris-buffer used. They determined that larger molecular weight DNA improved trapping ability, and increased Tris-buffer concentration decreased trapping ability. Asbury and van den Engh also demonstrated the controlled movement of trapped DNA from one electrode edge to the next electrode edge by application of a step dc voltage.

In contrast to Wang who described the electric field distribution using the Green's Theorem based method, Asbury and van den Engh solved the Laplace equation, $\nabla^2 \bar{E} = 0$, numerically to obtain the electric potential in a periodic cross-sectional model of a parallel array electrode structure [93]. Figure 3-9 displays the result of this numerical analysis by plotting the trapping potential along a horizontal line 1 μm above the electrode plane in the case of a 1 V_{p-p} signal applied between electrodes. Positions of electrodes are depicted as black bars along the positional x axis. From Figure 3-9, it is evident that the maximum of $\nabla |\bar{E}|^2$ occurs near the edges of the electrodes and minimums occur over the central region of the electrodes and over the central region of the gaps.

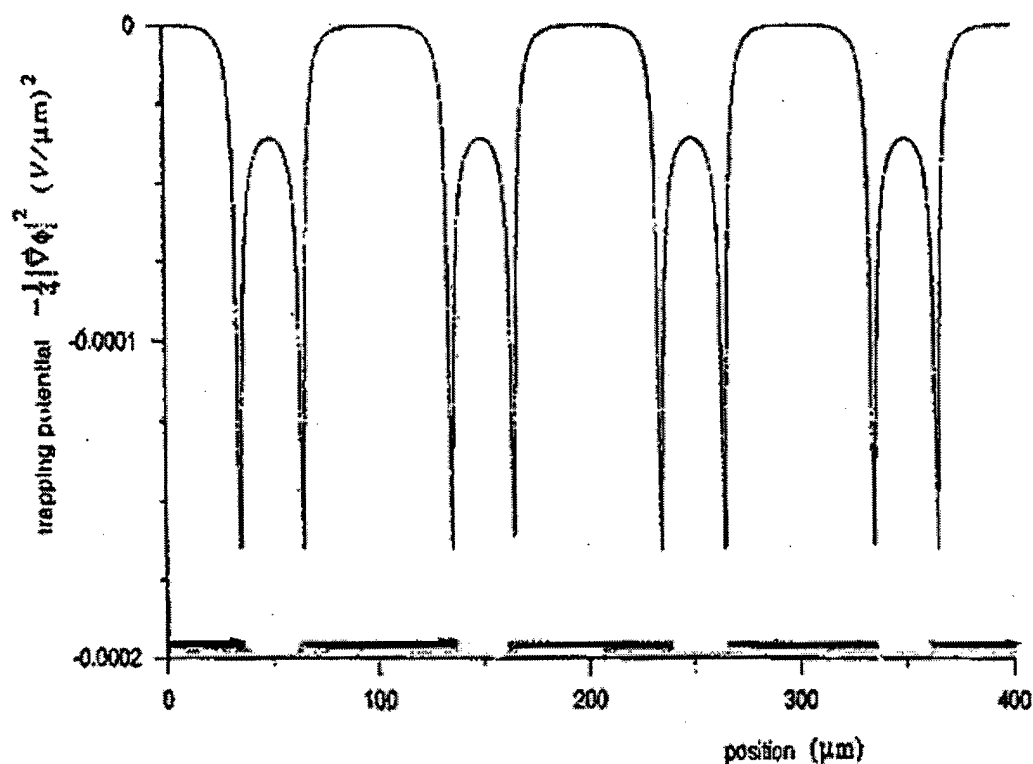


Figure 3-9 Trapping potential for dielectrophoretic trapping computed along a horizontal line 1 μm above the electrode surface. Deep and narrow wells are present [2].

Asbury and van den Engh observed two unexplained phenomenon. First, they observed that trapped DNA underwent swirling cylindrical motions over the electrode edges. This phenomenon is shown in Figure 3-10. They theorized this swirling may result from heating of the fluid near the electrode edge, thereby, causing a local decrease in the dielectric constant of the fluid. Negative dielectrophoresis of the fluid would then push the less-polarizable fluid out over the electrode where the field strength is weakest. Another explanation as theorized by Asbury and van den Engh, was that the electrode-liquid interface could have diode-like characteristics, allowing charge to exchange more easily in one direction than the other. The corresponding electric field would not be exactly symmetric with respect to a change in field polarity.

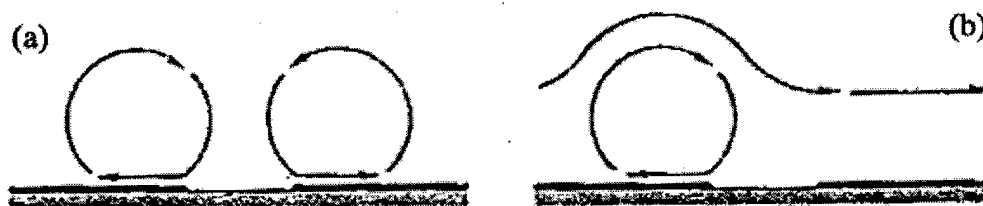


Figure 3-10 Schematic of swirling motion of trapped DNA molecules: (a) The direction of the swirling was always the same with respect to the electrode edge. (b) Interaction between the swirls and the bulk flow may be responsible for the asymmetry of the release from the traps when a steady voltage is used to dislodge the molecules [2].

The second unexplained phenomenon was that trapped molecules on one electrode edge appeared to more easily dislodge with a steady voltage pulse than those on the opposite edge. Asbury and van den Engh also employed the localized heating of the fluid and diode-like characteristics to explain this phenomenon.

Asbury and van den Engh generally described four potential applications of dielectrophoretic trapping that could be integrated into existing biological devices and techniques: DNA separation techniques, single molecule measurements, improved hybridization efficiency on DNA arrays, and genetic transformation of bacteria. These applications revolve around the concept of concentrating DNA at specific locations.

Of relevant importance is DNA separation techniques as described by Asbury and van den Engh. They envisioned that dielectrophoretic trapping could improve microfabricated separation techniques, whereby, DNA could be concentrated upstream or downstream of an arbitrary sieving medium such as a gel or microfabricated obstacle array [89, 90]. The concentration line of DNA would provide an ideal starting population for electrophoretic separation before entering the sieving medium downstream of the trapped DNA. DNA would then be size separated once entering the sieving medium.

3.5 Uncertainties and Discrepancies in Related Work

3.5.1 Dimensions of Parallel Array Electrodes

Certainly one principle difference between the microelectrode devices used among these various groups concerns the microfabricated electrode dimension. Here electrode dimension not only refers to the electrode width, w , and gap, d , but also the thickness, t , of the fabricated electrodes. These definitions are depicted in

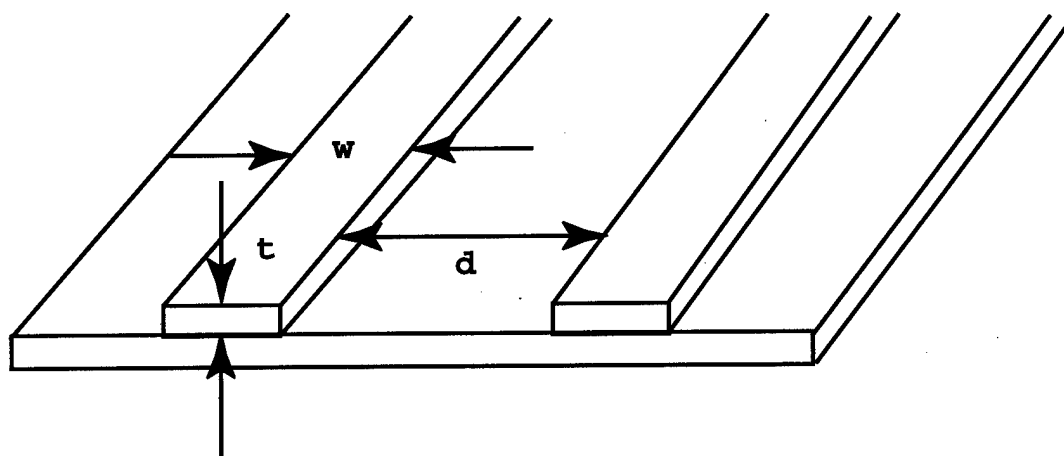


Figure 3-11 Definition of electrode dimensions for width, w , gap, d , thickness, t .

For example, Asbury and van den Engh used parallel electrode arrays with electrodes having width, $70\mu\text{m}$, gap $30\mu\text{m}$ and thickness, 60 \AA . Table 3.1 presents the electrode array types used by the various groups as well as the dimensions of the electrodes used. Some data in Table 3.1 is missing due to the fact this information was not reported in the literature. Because Wang performed his early research in the same group as Gascoyne, it is assumed Gascoyne used similar electrode thicknesses as Wang.

Table 3.1 Comparison of electrode parameters among various groups.

Group	Type Electrode Array	Electrode Width, w (μm)	Electrode Gap, d (μm)	Electrode Thickness, t		
				Seed Layer (\AA)	Electrode Layer (\AA)	Total (\AA)
Asbury	Interdigitated Parallel	70	30	20	40	60
Gascoyne	Interdigitated Parallel	80	80	N/A	N/A	apprx. 1000
	Interdigitated Castellated	80	80	N/A	N/A	apprx 1000
Wang	Interdigitated Parallel	20, 50	20, 50	70	1000	1070
	Concentric	20	20	100	250	350
	Interdigitated Parallel	N/A	4, 15, 55	N/A	N/A	10000
Washizu	Interdigitated Sinusoidal	N/A	4, 15, 55	N/A	N/A	10000

3.5.2 *Applied Electric Field Strengths and Frequencies*

Gascoyne and Wang experimented with various electric field strengths and frequencies in their studies with cells and microbeads. Their results are well characterized according to the dielectric properties of the particles examined.

When considering the observed field strengths and frequencies used by Washizu and Asbury and van den Engh with biological macromolecules such as DNA and BSA, a noticeable gap in the process space data is observed. Washizu used electric field strengths on the order of 10^6 V/m at frequencies of 1 MHz. Asbury and van den Engh used electric field strengths on the order of 10^5 V/m at very low frequencies approaching dc. Yet at both extremes of the available field strength and frequency spectrum, both observed dielectrophoresis of DNA or BSA.

3.5.3 *Suspension Medium, Chamber, and Flow Conditions*

Not all groups reported the experimental test chambers used in their research. Reported or inferred evidence suggests, though, that chamber thickness varied from 15 μm when

using a coverslip placed over the sample to 400 μm created by placing glass over the sample separated by appropriate height spacers. Those groups purposefully inducing flow within their chambers typically used fluid flow rates from 20-20,000 $\mu\text{L}/\text{min}$.

Not all groups reported conditions of the suspension medium in which the biological macromolecule was placed. Gascoyne typically used suspension mediums of desired conductivity to affect the real part the Claussius-Mossotti function in the desired manner. Washizu typically used dH_2O . Asbury and van den Engh experimented with different concentrations of a Tris-buffered saline solution as well as just using dH_2O .

3.6 Summary

This chapter presented the literature as reported by various research groups involved with dielectrophoresis. Early electrode geometries proposed by Pohl and Jones were considered. From their work, it was determined that electrode geometry and scale are important parameters in generating dielectrophoretic forces. Important work by Gascoyne et al. demonstrated that particles could be separated according to their dielectric properties by taking advantage of the phenomenon of negative and positive dielectrophoresis. Depending on the frequency, a particle may experience negative or positive dielectrophoresis and concentrate at different locations on a parallel electrode array. Work by Washizu and Asbury and van den Engh showed that biological macromolecules such as DNA and BSA could be dielectrophoretically gapped. It was concluded, though, that a considerable gap in the process space data exists between these two groups. Furthermore, the method of trapping, whether negative or positive dielectrophoresis, was suspect. Unanswered questions concerning electrode dimensions also exist. The next chapter will describe the design, fabrication, and characterization of the microanalytical system used for purposes of this research.

4 Methods and Materials

The overall theme of this chapter is the design and fabrication of the integrated microfluidic and microelectromechanical analytical system used in this research. The individual subsystem designs were achieved using a design method that focused on decoupling individual subsystems. The individual subsystems identified are the electrical subsystem, fluidic subsystem, and optical subsystem.

This chapter will first consider general design principles for a microanalytical system. The functional requirements that dictated the design of the microanalytical system and associated electrical, fluidic, and optical subsystems used in this research will then be enumerated. Consideration of design and fabrication methods will demonstrate how the subsystems satisfied their respective functional requirements. Photolithography and soft lithography methods will be described in general terms with emphasis on established protocols determined in this research. Fluid sample preparation will also be defined.

4.1 General Design of Microanalytical Systems

Microanalytical systems for performing chemical and biochemical reactions and analysis require cavities, channels, pumps, valves, storage containers, couplers, electrodes, and windows. According to Qin et al., the typical dimensions of these components are in the range of a few micrometers to several millimeters in the length or width and between 100 nm and 100 μm in depth and height. An extensive set of techniques for fabricating these microstructures exists [72]. This section describes critical issues involved in the design of these systems and describes available materials and technologies for their fabrication.

4.1.1 Critical Design Issues in Microanalytical Systems

A few critical issues must be considered in the design of any microanalytical system. Failure to take these issues into consideration will result in unexpected failure modes in the fabrication and experimental phases. With knowledge that reduced size results in

increased manufacturing and fabrication costs, little margin for error exists. Failure modes encountered late in the development and experimental phase are unacceptable and can lead to expensive design changes. All attempts must be made early to properly design and model the system before any fabrication and subsequent experimentation begins. Three critical issues exist that must be considered throughout the design process: fluid handling, precision alignment and registry, and system accessibility.

Fluid handling is a critical issue in microanalytical systems due to dramatically reduced fluid volumes often in the range from picoliters to hundreds of microliters. One justification for making fluidic systems smaller is the reduced volume of required reagents and associated reduction in total assay or process cost. As the microanalytical systems becomes smaller, however, the miniaturization does not come without some potentially detrimental side-effects such as,

- 1) Surface adsorption,
- 2) Demanding valving requirements,
- 3) Demanding requirement for pump resolution,
- 4) Demanding sample introduction, and
- 5) Demanding sample management.

The complexity is dramatically illustrated when considering that typical fluid handling volumes are less than the volume contained in a drop of water.

The reduced fluid handling volumes result in dramatic fluid/system differences between those of higher volumes. Fluid evaporation and reagent adsorption issues become prominent. Even short exposures to an unsealed environment such as air will quickly cause evaporation of the fluid. Reagents contained in the fluid may quickly become lost due to nonspecific adsorption within the microanalytical structure to channel walls or

substrates. Reduced reagents in the chemical environment can dramatically change the reaction from a well-characterized process to an uncharacterized random process.

Managing small volumes of fluid into and through microfluidic devices is not trivial. Fluid vias that connect one device to another for transport require precise tolerances. Misaligned fluid vias cause a failure mode that will render a device unusable. Only through the availability and use precision tooling can these high tolerances be successfully achieved.

Aside from issues of fluid handling, another critical issue concerns interface of these microanalytical systems to appropriate methods of actuation and measurement. The application of electrical signals, injection of fluid samples, and clarity of optical viewing is often required. The process of design may be decoupled by considering the chemical and fluidic actuations and sensor subsystem requirements separately. An ideal design will be one that accommodates all requirements in the same physical space, but maintains a logical decoupling of subsystems.

4.1.2 Materials and Technologies for Fabrication of Microanalytical Systems

Many materials and technologies exist for designing and fabricating microanalytical systems. Qin and Whitesides provide an excellent description of these materials and technologies [72].

According to Qin and Whitesides, two general classes of materials exist for microanalytical systems: rigid materials and elastomeric materials. Rigid materials include silicon, glass, quartz, and rigid organic polymers such as epoxy, polyurethane, polyimide, polystyrene, and polymethylmethacrylate. Elastomeric materials include polydimethylsiloxane (PDMS), urethanes, and biocompatible specialty blends.

Each material, whether rigid or elastomeric, has application specific advantages and disadvantages. In choosing the proper material for a specific application, one must consider cost, strength, optical characterization, and surface properties. Silicon materials,

for example, tend to be expensive, brittle, opaque in the UV/visible regions, and its surface chemistry is complicated to manipulate. On the other hand, silicon is well-characterized, and the current technology infrastructure exists to support precise and repeatable fabrication methods. Emerging applications with alternative materials will eventually drive cost-effective prototyping and volume production of microanalytical systems.

Two classes of microfabrication technology used in the fabrication of the microanalytical system in this research are photolithography and soft lithography. Photolithography is the standard method for microstructure definition in the semiconductor industry. Soft lithography is a rapid prototyping method first presented by Whitesides that is extremely useful for certain manufacturing and microfluidic devices. Most applications today both techniques.

Xia and Whitesides distinguish photolithography from soft lithography in the following manner [117]. Photolithographic techniques currently used for manufacturing microelectronic structures are based on a projection-printing system in which the image of a reticle is reduced and projected through a high numerical aperture lens system onto a thin film of photoresist that is spin-coated on a wafer. The feature resolution is limited by the wavelength of light used according to $\lambda/2$, but in practice is limited according to λ . This typically results in a limit on the order of 100 nm.

Soft lithographic techniques are distinguished by the use of an elastomeric stamp or mold as the key element that transfers the pattern to the substrate. Each uses flexible organic molecules and materials rather than rigid inorganic materials. The key promise of these techniques resides in the ability to pattern features below the 100 nm limit. Most soft lithographic masks are, however, first generated using a master mold that is created using standard techniques of photolithography.

4.2 Electrical Subsystem Functional Requirements

This section describes the functional requirements for the electrical subsystem of the microanalytical system used in this research. In general, the concept of design with functional system decoupling has been applied wherever possible. The electrical subsystem has been decoupled into three additional subsystems: the MEMS microelectrode device upon which experiments are performed, the electrical interconnect that provides access to the microelectrode device, and the instrumentation used to generate appropriate electric signals at appropriate voltage levels, frequencies, and phase-angle. In all cases, dimensional attributes are defined in Chapter 4.6.

4.2.1 MEMS Microelectrode Device

The MEMS microelectrode device is defined as that component on which experiments are conducted, and hence contains the desired electrode patterns and geometries. Its functional requirements are defined as follows.

- Independently addressable dielectrophoretic regions – The ability to simultaneously manipulate particles according to their dielectric properties requires the ability to simultaneously apply different signals to the microelectrode device.
- Standard, symmetrical interface – The functional requirement of independently addressable dielectrophoretic regions requires a means of interconnect to excitation voltage sources. Symmetry of design reduces the probability of unforeseen failure modes by ensuring the microelectrode device can be positioned in different orientations and still be accessible.
- Inert, robust, optically-clear substrate – The substrate must be optically-clear for detection of fluorescently labeled particles. Attempts should be made to use an inert substrate, although, it is recognized that this condition may not be satisfied due to non-specific adsorption. A balance exists between a desired mechanically-robust,

substrate thickness and the working distance of the optical detection system. Thick substrates improve mechanical robustness.

- Inert, robust, non-corrosive electrodes – The deposition metal used for electrodes should be: inert to prevent non-specific adsorption of the particles to the electrodes; robust for repeated, long-term use; and non-corrosive as they will be used in proximity to fluids.
- Reserved fluidic region – The fluidic region must not prevent access to the electrical interconnect.
- Reserved handling and contact regions – Minimum contact with the electrodes dictates the ability to handle the microelectrode device without physically touching the electrodes.

Figure 4-1 shows an illustrative example of the microelectrode device fabricated and used in this research.

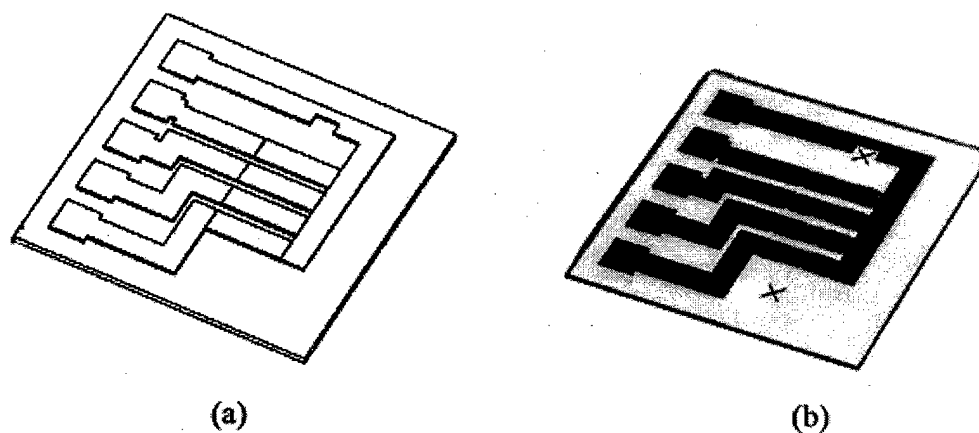


Figure 4-1 MEMS microelectrode device as: (a) Designed and (b) Fabricated.

4.2.2 Electrical Interconnect

The electrical interconnect is defined as that component which provides electrical access, mechanical registry, and optical access to the microelectrode device. Its functional requirements are defined as follows.

- Retractable, floating, precision-aligned pin assignment – The electrical contact pins are required to be precisely aligned to the standard, electrical interface of the microelectrode device. A critical failure mode exists if one or more electrical pins cannot access the microelectrode device. Each electrical pin should be retractable to break electrical contact with the microelectrode device. They are required to be independently adjustable and floating so that one pin assignment does not determine another pin's assignment.
- Electrical strain relief for minimal interference – The electrical interconnect must provide strain relief to all external connections from the microelectrode device.
- Vertical and horizontal clearance for rapid interchange – The electrical interconnect must allow for easy insertion and extraction of the microelectrode device. A failure mode exists if the microelectrode device cannot be removed or if upon removal it is damaged.

Figure 4-3 shows the electrical interconnect.

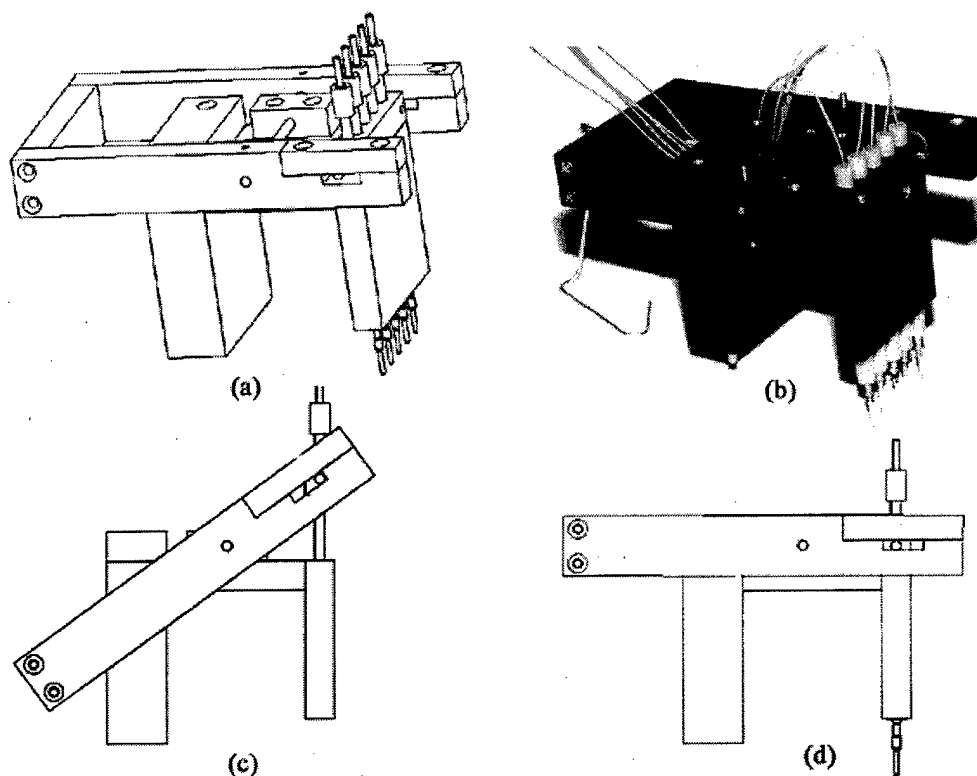


Figure 4-3 Electrical interconnect: (a) Isometric view (b) Actual device fabricated and used for experiments (c) Side view in retracted configuration (d) Side view in extended configuration.

4.2.3 *Electrical Instrumentation*

The electrical instrumentation is defined as those components which either generate or record electrical signals. Functional requirements are defined as follows.

- Independently generated voltage and frequency signals – Simultaneous generation of four electrical signals of different voltage and frequency is required. A failure mode exists if only one signal can be generated because this research requires that simultaneous signals be applied.

- Independently generated out-of-phase signals – Generation of electrical signals that are in or out phase by a controllable increment is required. A minimum of four phase-controlled signals is required.

The electrical instruments used for purposes of this research are shown Figure 4-4 in and are:

- Tektronix CFG253 3 MHz Function Generator,
- Tektronix 2252 100 MHz Programmable Hardcopy Oscilloscope, and
- Tektronix Digital Multimeter 254.



Figure 4-4 Electrical instruments.

4.3 Fluidic Subsystem Functional Requirements

This section describes the functional requirements for the fluidic subsystem of the microanalytical system used in this research. The fluidic subsystem is decoupled into three additional subsystems consisting of the MEMS microfluidic device, the fluidic interconnect, and fluidic instrumentation. In all cases, dimensional attributes are defined in Chapter 4.7.

4.3.1 MEMS Microfluidic Device

The MEMS microfluidic device is defined as that component which directs the fluid sample over the electrode arrays of the microelectrode device through fabrication of various channels of desired geometries. Its functional requirements are defined as follows.

- Standard, symmetrical interface – Standard, symmetrical fluid ports with well-defined interconnect positions reduce the probability of unforeseen failure modes by ensuring the microfluidic device can be positioned in different orientations and still be accessible from the outside world.
- Inert, robust, optically-clear material – The selected material must be inert to help alleviate nonspecific adsorption to the channel walls and loss of reagent, robust so that it can be easily removed and cleaned, and optically clear to determine proper sample injection.
- Surface conformable and self-sealing – The selected material must conform to and adhere to the surface of the microelectrode device in the presence of nonuniformities to provide a good seal and prevent fluid loss.
- Ease of removal and cleaning – The microfluidic device must be easily removed from the system so that it may be easily cleaned between experiments.

- Practical fluid flow rates – The channel geometries of desired width and depth must allow for practical fluid flow rates and association of flow parameters within the channel such as flow velocity and wall stress shear. A lower limit is placed on the fluid flow rate by the fluid delivery pump. The upper limit results from the channel geometry where the flow rate is required to be such that fluidic shear stress at the wall does not prevent particle capture.

Figure 4-5 shows an illustrative example of the microfluidic device.

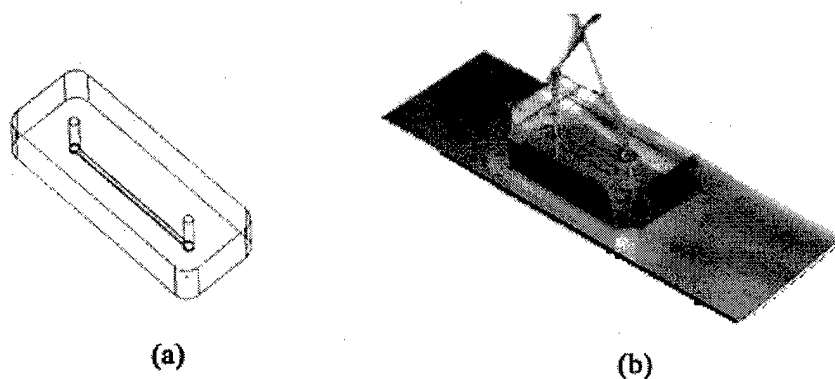


Figure 4-5 MEMS microfluidic device as: (a) Designed and (b) Fabricated.

4.3.2 Fluidic Interconnect

The fluidic interconnect is defined as that subsystem which provides fluidic access to the microfluidic device. Its functional requirements are defined as follows.

- Self-aligning, precision fluid port registry – Fluid ports must be precisely aligned to those of the microfluidic device. Inability to access the microfluidic device prevents fluid sample injection to and recovery from the microfluidic device. The fluidic interconnect must be self-aligning so that consistent sample injection and recovery is possible.

- Microsample injection and capture – Injection and recovery of the fluid sample is required.
- Strain relief for minimal channel interference – The fluidic interconnect must provide strain relief from the microfluidic device. The strain relief isolates the microfluidic device from minor mechanical pulls or tugs on the interconnect tubing during experimental set-up.
- Easy breakdown for channel cleaning – The fluidic interconnect must allow for easy insertion and extraction of the microfluidic device. A failure mode exists if the microfluidic device cannot be removed or if upon removal is damaged.

Figure 4-6 shows the mechanical interface as designed and the actual mechanical interface as fabricated and used in this research.

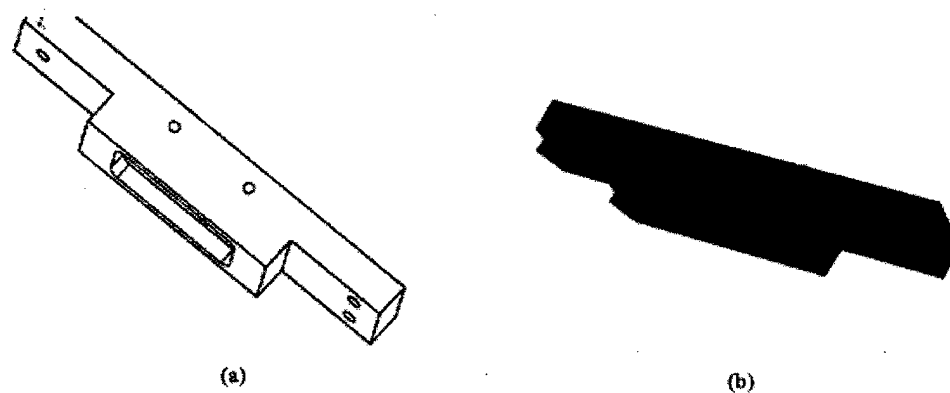


Figure 4-6 Fluidic interconnect as: (a) Designed and (b) Fabricated.

4.3.3 Fluid Pump

The fluid pump injects and recovers the fluid sample from the microfluidic device via the fluidic interconnect. Its functional requirements are defined as follows.

- Acceptable flow rates – It must be capable of providing for a range of fluid flow rates such that the minimum flow rate does not prevent particle capture.
- Sufficient volume capacity – It must be capable of holding necessary fluid sample volumes.

For purposes of this research, a Kloehe Syringe Drive Module 50300 (Las Vegas, NV, USA) with fittings supplied by Upchurch Scientific (Oak Harbor, WA, USA) was used.

4.4 Optical Subsystem Functional Requirements

This section describes the functional requirements for the optical subsystem of the microanalytical system. The optical subsystem is decoupled into two subsystems: the microscope interface platen upon which the electrical and fluidic subsystems are positioned and the fluorescent microscope component that provides for visualization and image capture of fluorescently labelled particles. This system is termed collectively as the microscopy station.

4.4.1 Microscope Interface Platen

The microscope interface platen provides a stable and precise geometric platform for the electrical and fluidic subsystems where the platen is precisely registered to the optics of epi-fluorescent microscope. Its functional requirements are defined as follows.

- Functional compatibility with electrical and fluidic subsystems – The microelectrode and microfluidic devices are registered precisely upon the microscope interface platen.
- Functional compatibility with microscope - The microelectrode device requires optical view window access aligned with the objectives of the fluorescent system.
- Removable, self-contained fixture platform - The microscope interface platen must be easily inserted and removed from the epi-fluorescent microscope.

- Self-aligning chip compartment - The microelectrode device must be easily positioned within the microscope interface platen for consistent and reproducible insertion.
- Self-aligning fluidic port holes - The microfluidic device must be easily positioned upon the microscope interface platen device for consistent and reproducible insertion.

Figure 4-7 shows the microscope interface platen.

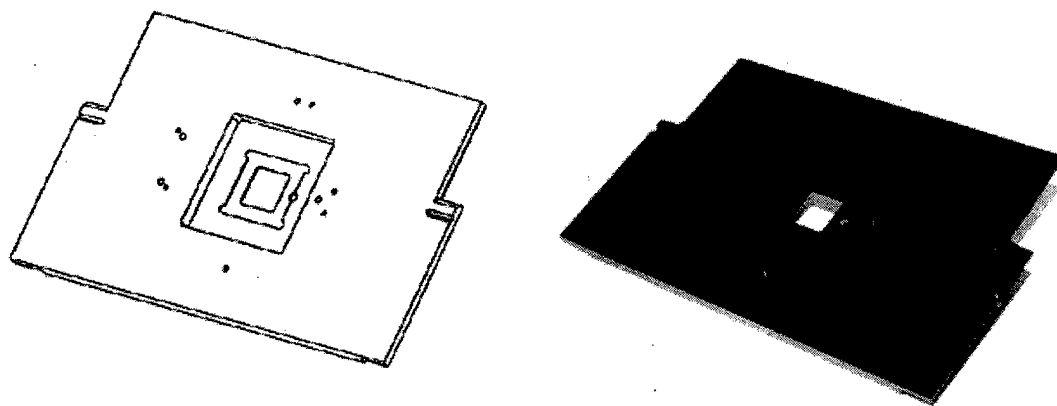


Figure 4-7 Microscope interface platen as: (a) Designed and (b) Fabricated.

4.4.2 Microscopy Station

The microscopy station is defined as that subsystem which views fluorescently labeled particles, captures the image for recording purposes, and processes the images for publishing purposes. It has been decoupled into three subsystems: epi-fluorescent microscope, image capture, and image processing.

The epi-fluorescent microscope has the following functional requirements.

- Absorption and emission spectra – The microscope must be capable of simultaneously viewing at least two different fluorescently labeled particles which, in the context of this research, is DNA and BSA.
- Long working distance objectives – The objectives must be capable of viewing images through the resulting substrate thickness of the microelectrode device.

The microscope used for purposes of this research was a Zeiss Axiovert 135 with long distance working objectives of 40x , numerical aperture 0.6, and 63x, numerical aperture 0.75, along with appropriate filter sets. Figure 4-8 shows the absorption and emission spectra of the fluorescent dyes YOYO-1 (Y-3601) used to label DNA and Alexa Fluor 594 (A-13101) used to label BSA; both were purchased from Molecular Probes (Eugene, OR, USA).

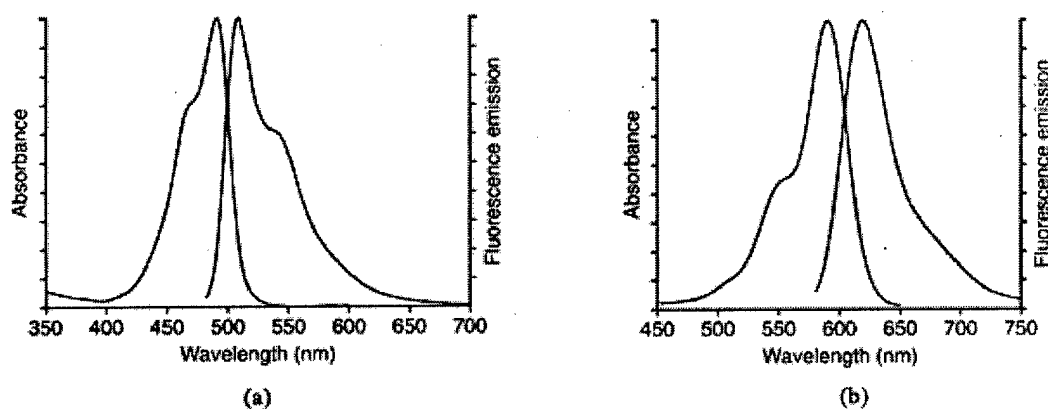


Figure 4-8 Absorption and emission spectra for fluorescent dyes: (a) YOYO-1 and (b) Alexa Fluor 594 as supplied in the Material and Safety Data Sheets.

The image capture system is defined as that system which captures the fluorescent image for recording purposes and has the following functional requirements.

- Low level light capability – The image capture system must be capable of capturing images under conditions of low level light.
- Integration – The image capture system must be capable of integrating an image over a period of time to increase the light intensity and improve image quality.

The image capture system used for purposes of this research was a Dage-MTI, Inc. (Michigan City, IN) 3-Chip Cooled CCD Color Camera along with Scion Image Capture software. The Dage-MTI camera is capable of integrating an image for up to 256 frames, with 30 ms between frames, to increase the intensity of low level light signals. The camera was capable of capturing live or still images. Live images could also be recorded using a Sony Hi-Fi SVO-2000 VCR.

The image processing system is defined as that system which enhances the captured image for both qualitative purposes such as publishing images and quantitative purposes such as determining particle capture concentration levels.

- Image enhancement – The image processing system must include such features as brightness/contrast levels, channel mixing, and filtering operations.
- Quantitative analysis – The image processing system must be capable of performing histogram analysis, surface intensity plots, and numerical integration.

Image processing in this research was accomplished using Adobe's Photoshop 5.5 and Matlab's Image Processing Toolbox. Photoshop was used for qualitative image enhancement in order to present general particle behavior. Figure 4-9 shows the microscopy station consisting of the epi-fluorescent microscope, image capture system and image processing system, used to collect, record, and process data.

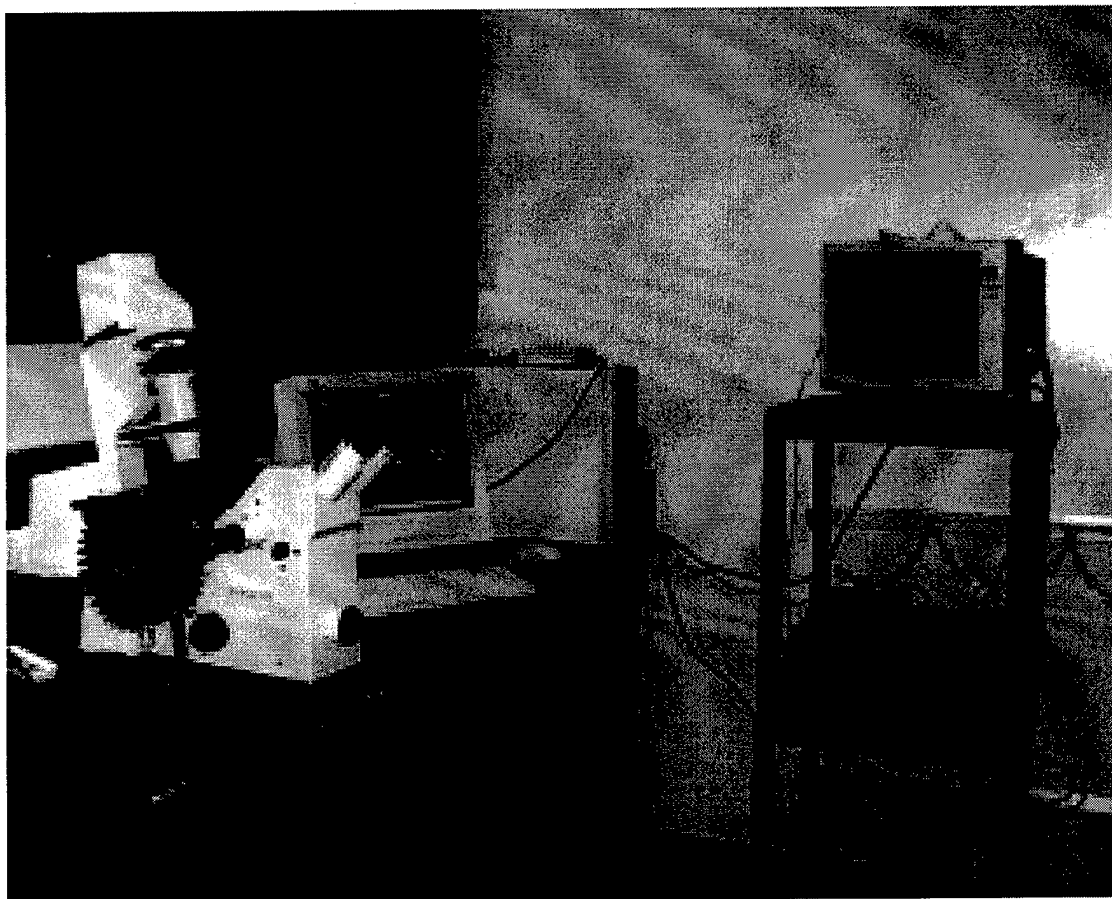


Figure 4-9 Microscopy station equipped with a Zeiss fluorescence-capable Axiovert 135, Dage-MTI 3 Chip Cooled CCD Camera, Scion Image Capture software, and Sony Hi-Fi SVO-2000 VCR.

4.5 Microanalytical System Integration

Figure 4-10 shows the integration of the microelectrode device, electrical interconnect, microfluidic device, and microscope interface platen. Figure 4-11 shows these subsystems inserted into the Zeiss Axiovert 135 epi-fluorescent microscope.

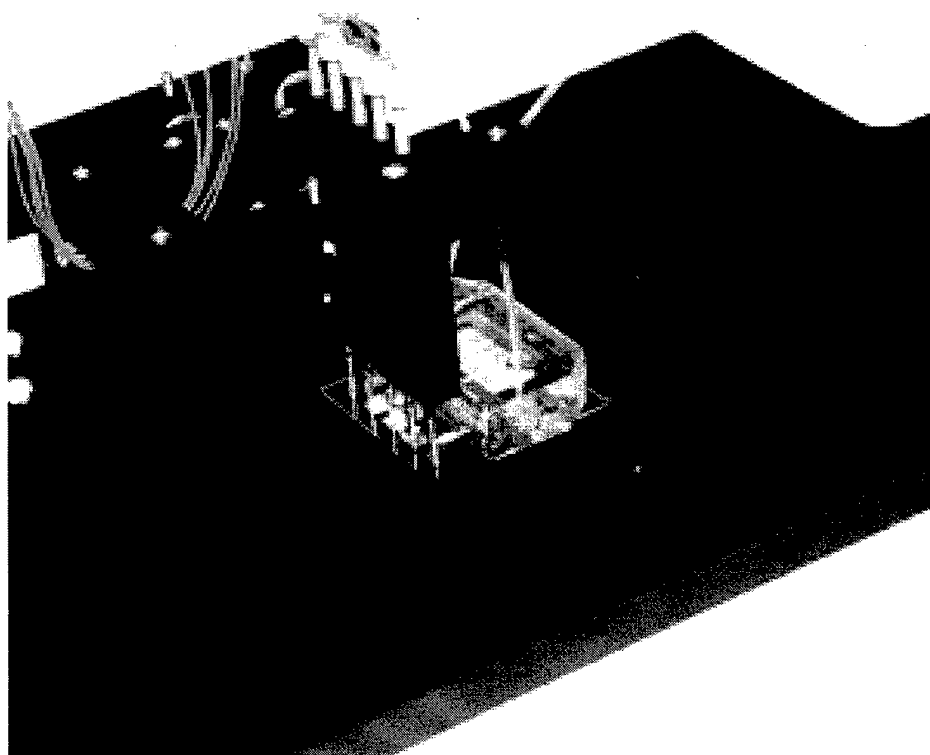


Figure 4-10 Microanalytical system integration.



Figure 4-11 Microanalytical system integration into Zeiss Axiovert 135 epi-fluorescent microscope.

4.6 Design and Fabrication of the Electrical Subsystem

This section describes the design and fabrication of the electrical subsystem decoupled into the MEMS microelectrode device and electrical interconnect. All microelectrode devices were first sketched on paper and then in AutoCAD LT 98 [16]. The electrical interconnect was first sketched on paper and detailed design performed in SolidWorks 98 [79]. The design features and subsequent fabrication methods for the microelectrode device are first presented followed by the same for the electrical interconnect. Photolithography protocols will also be examined.

4.6.1 MEMS Microelectrode Device

This section presents the unique design features and subsequent fabrication methods of the MEMS microelectrode device. Figure 4-12 shows the general schematic of the MEMS microelectrode device. Several design features are highlighted. These design features fully satisfy the functional requirements.

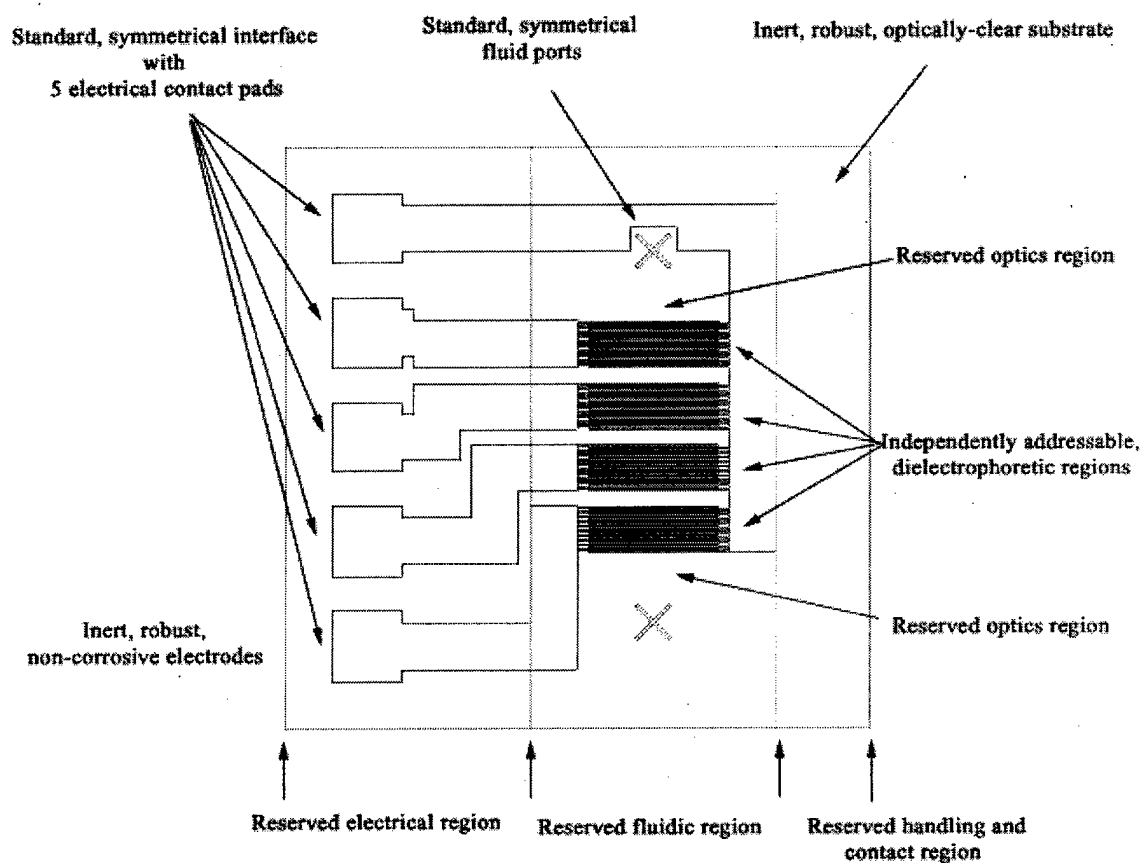


Figure 4-12 Schematic of MEMS microelectrode device illustrating the unique design features.

One feature of this design is the ability to simultaneously apply different electrical signals to the microelectrode device. In this manner, particles with different dielectric properties can conceivably be independently manipulated.

Another design feature is the potential use of this microelectrode device as a generalized testbed platform. The central region of the microelectrode device contains the experimental region. The surrounding features only serve to interface the microelectrode device with the outside world. Any desired central experimental pattern may be designed and implemented on this microelectrode device because the standard electrical and fluidic interfaces serve to connect it to existing external fixtures.

In summary, these and other unique features include:

- Independently addressable dielectrophoretic regions for independent application of electrical signals and subsequent manipulation of dielectric and charged particles,
- Generalized testbed platform with central and independently patterned experimental region,
- Standard, symmetrical electrical and fluidic interfaces for easy and robust interface with external fixtures,
- Inert, robust, non-corrosive gold electrodes for repeated, long-term use, and
- Reserved handling and contact region fabricated from robust substrate for repeated, long-term use.

Figure 4-13 shows another general schematic of the microelectrode device with labeled dimensions in millimeters.

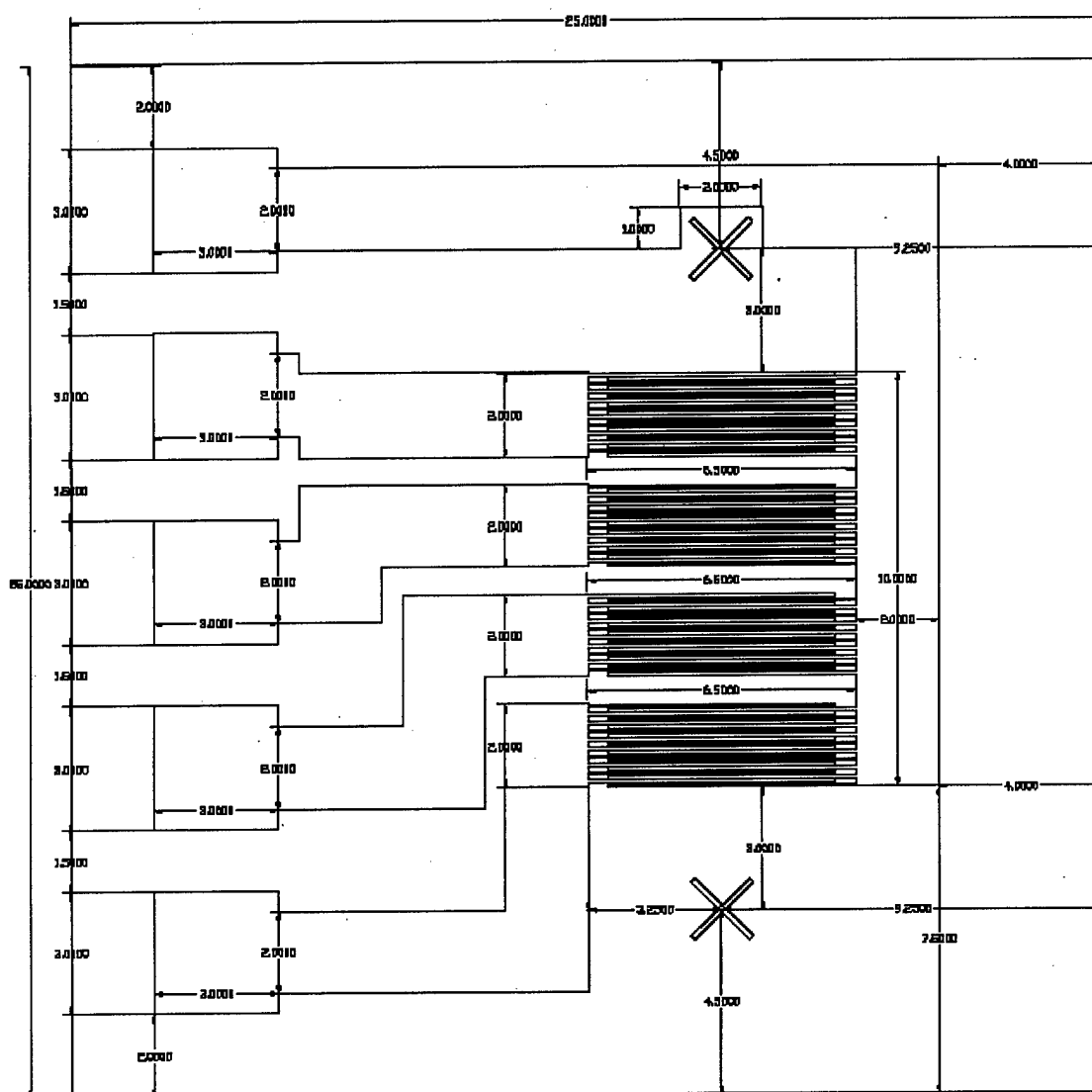


Figure 4-13 Detailed schematic of MEMS microelectrode device illustrating dimensions in millimeters (not to scale).

4.6.2 Geometry #1 - Parallel, Interdigitated

Figure 4-14 shows the standard parallel, interdigitated electrode geometry used in this research.

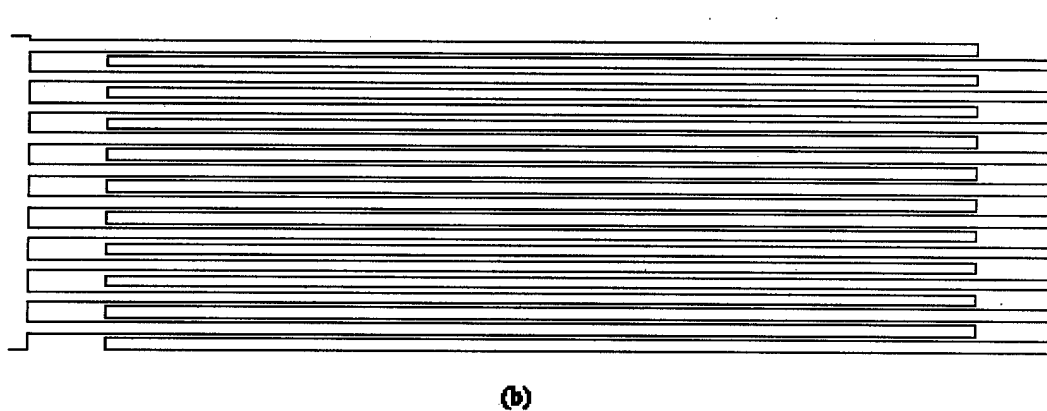
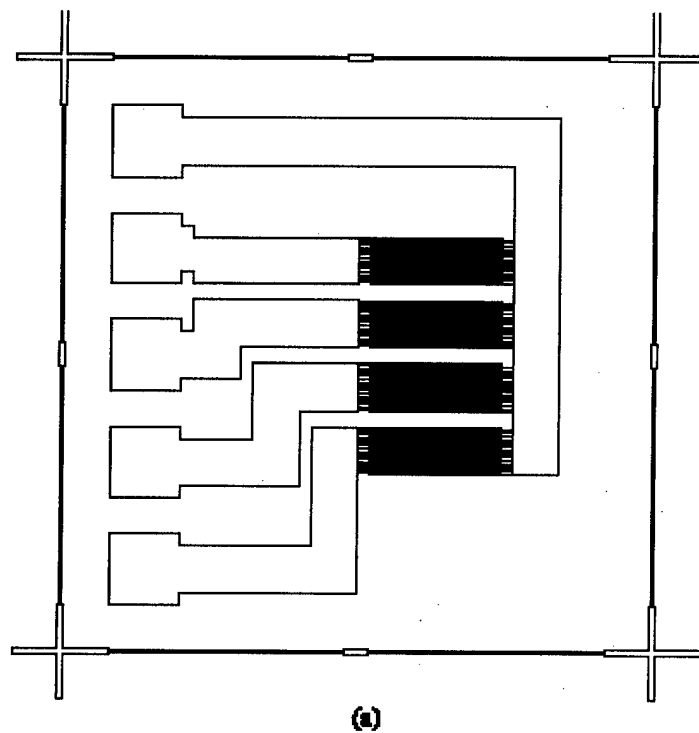


Figure 4-14 Parallel, interdigitated, electrode geometry: (a) The MEMS microelectrode device (b) Detailed view of one electrode group having electrode width of 70 μm and electrode gap of 30 μm .

Various groups most often use this design in related work. As shown in Table 4.2, however, electrode width and gap vary among the different groups. For purposes of this research, an electrode width of 70 μm and electrode gap of 30 μm for 100 μm period similar to Asbury and van den Engh was used [2]. Figure 4-14 (a) also shows the dicing lanes that define the boundary of the microelectrode device.

4.6.3 Geometry #2 - Parallel, Interdigitated, Castellated

Figure 4-15 shows the parallel, interdigitated, castellated electrode geometry used in this research.

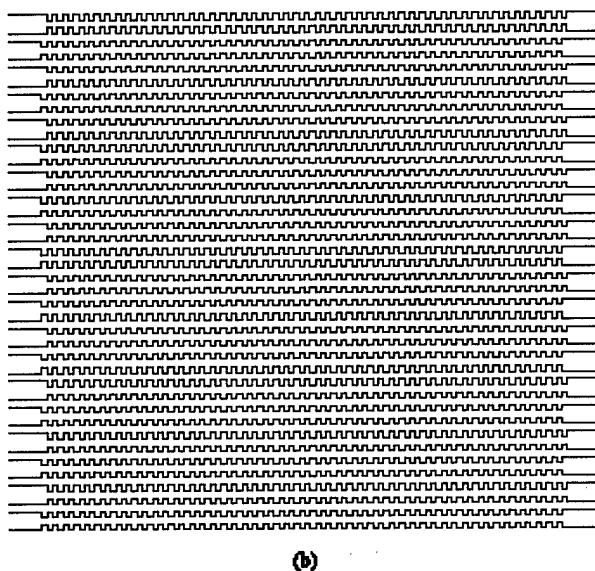
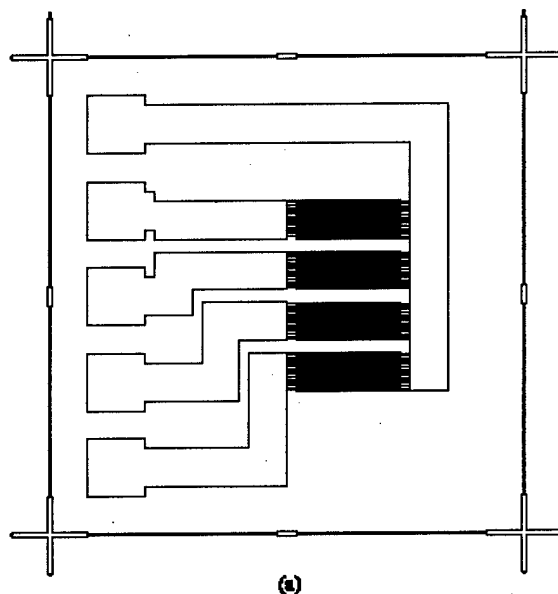


Figure 4-15 Parallel, interdigitated, castellated electrode geometry: (a) The MEMS microelectrode device (b) Detailed view of one electrode group having an electrode width of $70\text{ }\mu\text{m}$, electrode gap of $30\text{ }\mu\text{m}$, and characteristic tooth geometry of $20\text{ }\mu\text{m}$.

This design is similar to that used by Gascoyne et al. to show positive and negative dielectrophoretic trapping regions. Note here, however, the castellated geometry does not span the entire electrode length, but rather only the central region of the array. The geometry has an electrode gap and spacing of $80\text{ }\mu\text{m}$ giving an electrode period of $160\text{ }\mu\text{m}$ with characteristic tooth geometry of $80\text{ }\mu\text{m}$ [40]. For purposes of this research, an electrode width of $70\text{ }\mu\text{m}$ and electrode gap of $30\text{ }\mu\text{m}$ for electrode period of $100\text{ }\mu\text{m}$ with characteristic tooth geometry of $20\text{ }\mu\text{m}$ was used. The electrode period used was the same as for the parallel, interdigitated design because this electrode period was already proven to trap DNA by Asbury and van den Engh [2]. Figure 4-15 (a) also shows the dicing lanes that define the boundary of the microelectrode device.

4.6.4 Geometry #3 - Concentric Travelling Wave

Figure 4-16 shows the concentric travelling wave pattern used in this research.

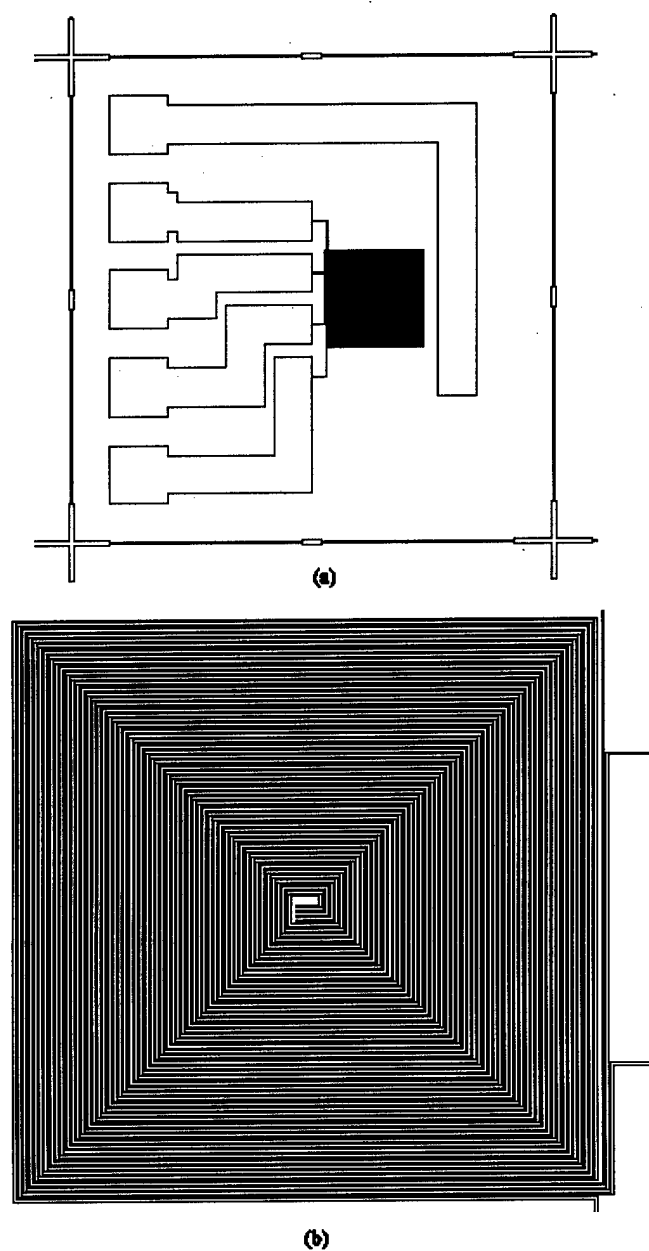


Figure 4-16 Concentric travelling wave electrode geometry: (a) The MEMS microelectrode device (b) Detailed view of the pattern shows that the four excitation electrodes spiral towards the center. The electrodes have width of $20\text{ }\mu\text{m}$ and gap of $20\text{ }\mu\text{m}$.

This pattern is termed a travelling wave pattern due to the characteristic movement particles undergo in the presence of phase-sequenced applied fields. Depending on the excitation signals, particles can be made to either concentrate in the center of the pattern or move towards the edges of the pattern. The excitation signals must each be subsequently $\pi/2$ or 90 degrees out of phase. The resultant travelling wave in concert with typical negative dielectrophoresis serves to move particles toward the center of the pattern or towards the edge of the pattern depending upon the order of the excitation signals. This pattern is similar to that used by Wang [98]. Here, though, the concentric pattern is square instead of circular. The electrodes have a width of 20 μm and gap of 20 μm . Also the fourth electrode pad that typically serves as the ground electrode is left floating.

4.6.5 Geometry #4 - Variable Pitch Rate

Figure 4-17 shows the variable pitch rate electrode design used in this research.

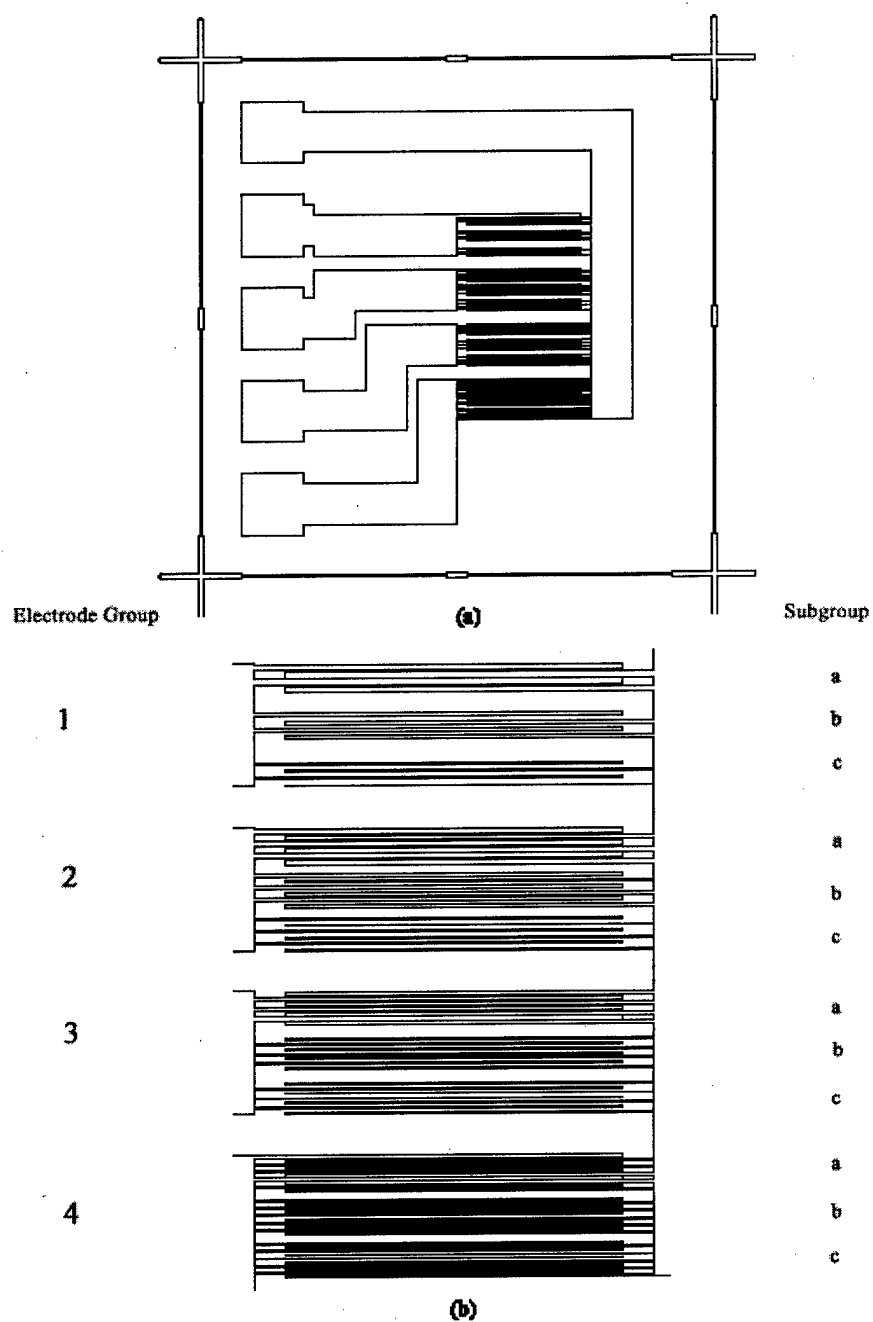


Figure 4-17 Variable pitch rate geometry: (a) The MEMS microelectrode device (b) Detailed view of all electrode groups shows different pitch rates or electrode periods. Refer to Table 4.1 for the definition of these pitch rates.

This design contains electrode arrays of different width and gap leading to different pitch rates or electrode periods. This design serves to investigate the effect of electrode period on trapping and concentration ability. The basic geometry is that of the parallel, interdigitated electrode design. Table 4.1 defines the electrode periods for each electrode group. Analysis of Figure 4-17 shows that decreasing the electrode pitch rate or period increases the effective packing area available for trapping.

Table 4.1 Definition of geometries used in variable pitch rate design.

Electrode Group	Characteristic Period (um)	Subgroup	Electrode Width (um)	Electrode Gap (um)
1	120	a	20	100
		b	60	60
		c	100	20
2	100	a	20	80
		b	50	50
		c	80	20
3	80	a	20	60
		b	40	40
		c	60	20
4	60	a	20	40
		b	30	30
		c	40	20

4.6.6 Variable Electrode Thickness and Summary of Electrode Geometries

One unique ability that thin film deposition offers is the ability to vary metal deposition times and thereby fabricate thin film electrodes at different thicknesses. It will be shown in Data Collection, that the effects of electrode thickness on device performance are relevant in the low frequency excitation range.

Table 4.2 presents the electrode pattern designs and the associated electrode thicknesses. All electrodes are patterned on glass wafers. Each wafer contains all four electrode geometries. In Table 4.2, only the wafer number assignment is used. Batch 1 refers to the initial batch of wafers processed to determine a proper adhesion layer, Titungsten, for the gold electrodes. A 75 Å Titungsten adhesion layer was deemed sufficient. Batch 2 refers to fabrication of various gold electrode thicknesses all having a 75 Å adhesion

layer. Batch 3 refers to the processing of a single wafer with 10,000 Å gold layer similar to the thickness used by Washizu [114].

Table 4.2 Wafers of various electrode thickness as designed and fabricated.

Batch	Wafer	Adhesion Layer (Å)	Gold Layer (Å)	Total Thickness (Å)
1	1	375	2000	2375
	2	275	1500	1775
	3	175	1000	1175
	4	75	500	575
	5	20	40	60
2	1	75	2000	2075
	2	75	1500	1575
	3	75	100	175
	4	75	250	325
	5	75	100	175

4.6.7 Photolithography

A brief outline of the process of photolithography will now be given. Sputtering is the first step, and it refers to the thin film deposition of desired metals onto a substrate or wafer which can then be patterned with a thin film of photoresist and subsequently wet or dry etched. Titanium was initially deposited onto a glass wafer to serve as an adhesion layer for the Gold. Gold was then deposited on top of the Titanium layer. The thin film deposition instrument used in this research was the MRC 882 SputterSphere and is shown in Figure 4-18. Deposition rates are unique for each system, and must be determined before use to deposit the correct thickness. If the deposition rate is given as x Angstroms/minute, the required deposition time for a layer of thickness, t , is given as,

$$\frac{t}{x}$$

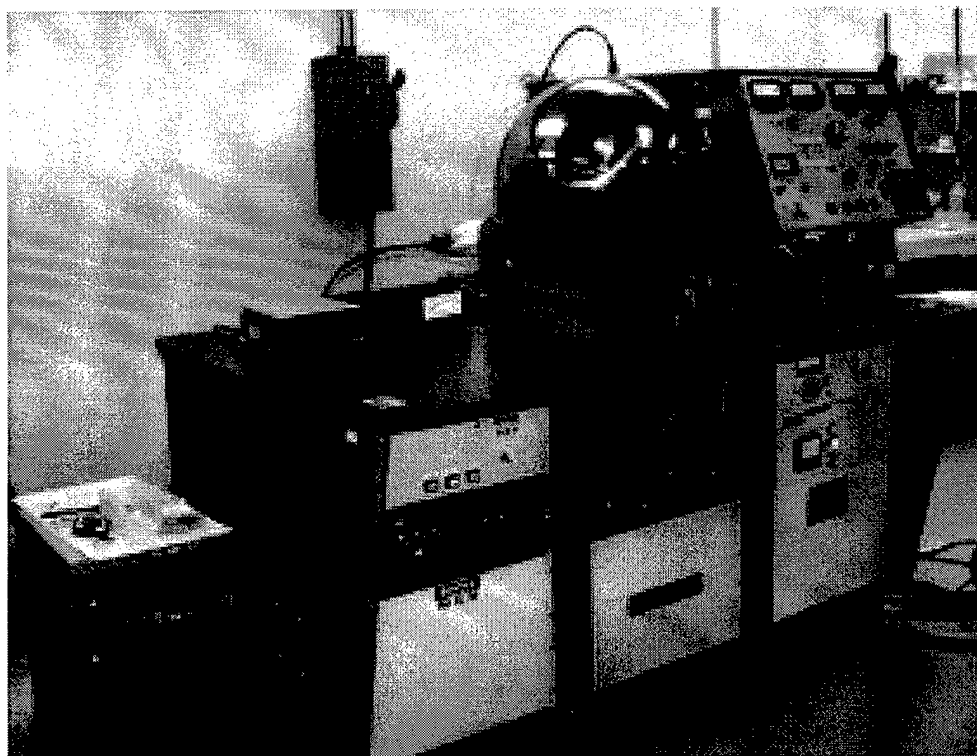


Figure 4-18 MRC 882 SputterSphere located in the Washington Technology Center's Microfabrication Laboratory at the University of Washington.

The next two steps are termed spin coating and soft-bake. A photosensitive chemical generally termed photoresist is then spun on top of the deposited metals. The photoresist will protect the deposited metals during the etching cycle. The spin cycle goes first through a 5 second spread at 500 rpm followed by a 30 second spin at 1500 rpm. The photoresist used in this research was a positive photoresist named AZ 1512 and is shown in Figure 4-19. The photoresist is then soft-baked in an oven at 90° C for 30 minutes after spin coating.



Figure 4-19 Photolithography chemicals: (a) AZ 1512 Negative Photoresist (b) AZ 351 Developing Solution (c) TFA Gold Etchant (d) Hydrogen Peroxide 30% Industrial Grade.

The next step is termed exposing. The photoresist that now covers the deposited metals can then be exposed to UV light through a dark field or light field photomask. The photomask contains the desired pattern that will be transferred to the photoresist and subsequently etched into the deposited metals. This light field photomask used in this research was first designed using AutoCAD LT 98 with the resulting DXF file sent out of house to PhotoSciences (Torrance, California, USA) who fabricated the photomask as shown in Figure 4-20. Using a positive photoresist, that area of photoresist which is exposed to UV light undergoes a chemical reaction and is subsequently washed away in the development cycle leaving photoresist to protect the patterned metals during the etching cycle. Figure 4-21 shows the Quintel 2001 3" Aligner for exposing wafers. The wafer is generally exposed to UV light for 15 seconds.

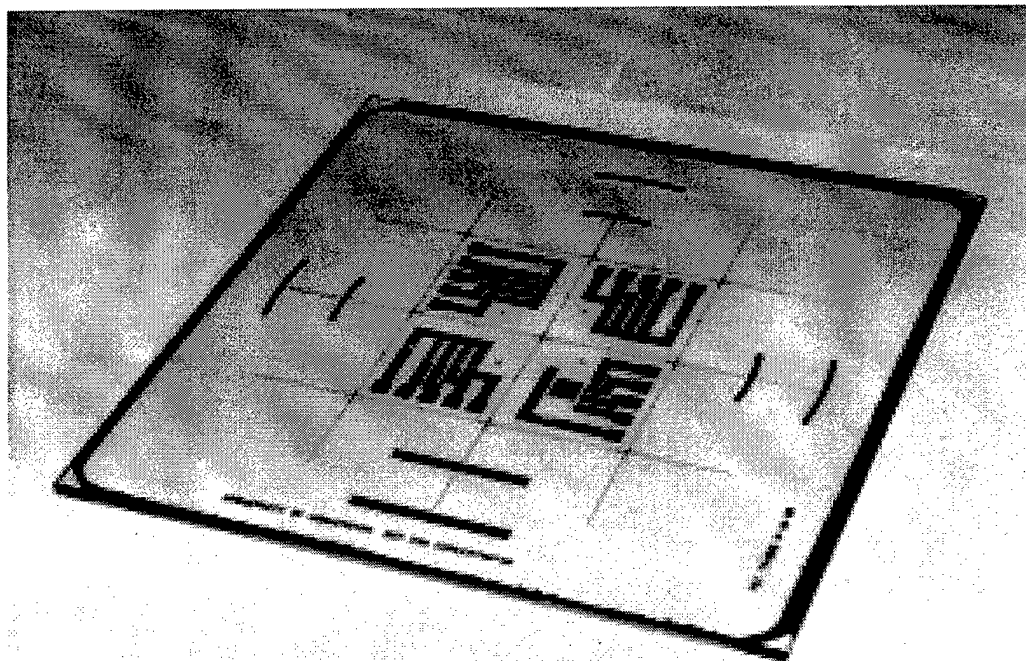


Figure 4-20 Light field photomask.



Figure 4-21 Quintel 2001 3" Aligner located in the Washington Technology Center's Microfabrication Laboratory at the University of Washington.

The next two steps are termed developing and hard-bake. After exposing the wafer, it is then be developed in AZ 351 Developing solution (see Figure 4-19) to remove the exposed photoresist leaving only unexposed photoresist patterned. Devleoping time is generally 1 minute. After development, the wafer is then hard-baked in an oven at 120° C for 45 minutes to harden the photoresist and thereby protect it and the metal under it during etching.

After hard-bake, the photoresist-covered wafer with desired electrode pattern is then etched to remove the unwanted metal. The wafer is first placed in a TFA Gold Etchant

(see Figure 4-19) for an amount of time as determined by the film thickness according to **Error! Reference source not found.** Care must be taken to not overetch the gold as undercutting may occur and result in an undesirable pattern. This is especially important when working with thick films. After etching the gold, it is immediately placed in a dH_2O rinse to stop the etching process. The wafer is then placed in a 30% Hydrogen Peroxide Industrial Grade solution (see Figure 4-19) for an amount of time as determined by the Tungsten film thickness according to Eq. 4.1. The wafer is then immediately placed in a dH_2O rinse to stop the etching process. The remaining product is the substrate with Tungsten, Gold, and photoresist layers in the desired electrode pattern. The photoresist can then be simply removed with Acetone and cleaned with Isopropyl Alcohol. Figure 4-22 shows the wafer before backend processing (dicing).

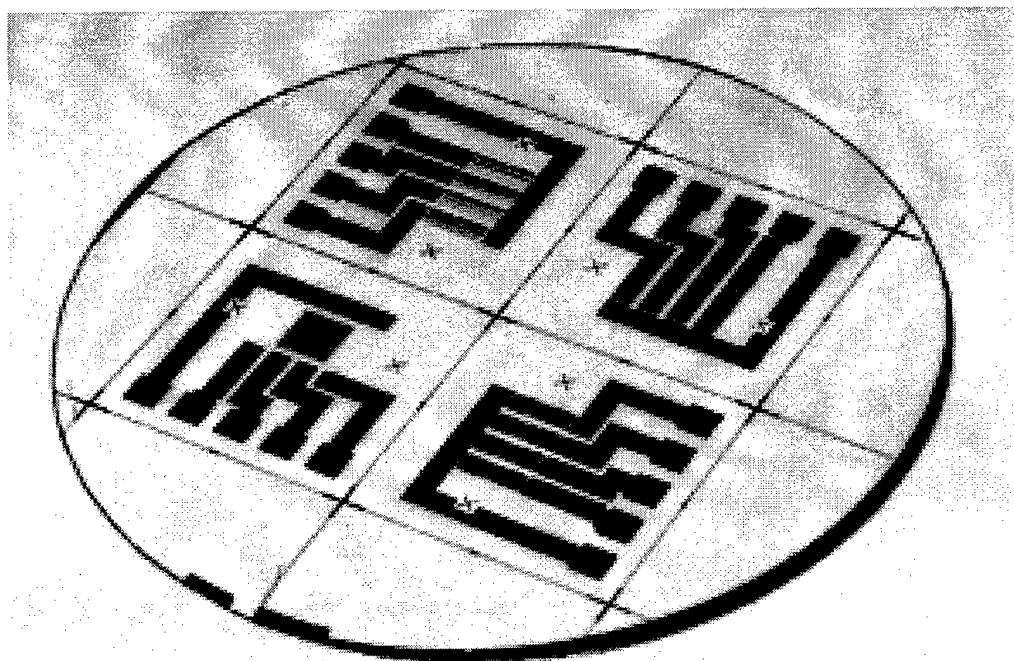


Figure 4-22 A processed wafer containing microelectrode devices as used in this research.

The final step is termed backend processing. Backend processing refers to rendering the microfabricated device usable. This primarily involves dicing the wafer to remove the microelectrode devices from the substrate. The Tempress 601 Dicing Saw for 2, 3, and 4" wafers accomplished this and is shown in Figure 4-23.



Figure 4-23 Tempress 601 Dicing Saw for 2, 3, and 4" wafers located in the Washington Technology Center's Microfabrication Laboratory at the University of Washington.

4.6.8 *Electrical Interconnect*

Figure 4-24 illustrates the electrical interconnect design.

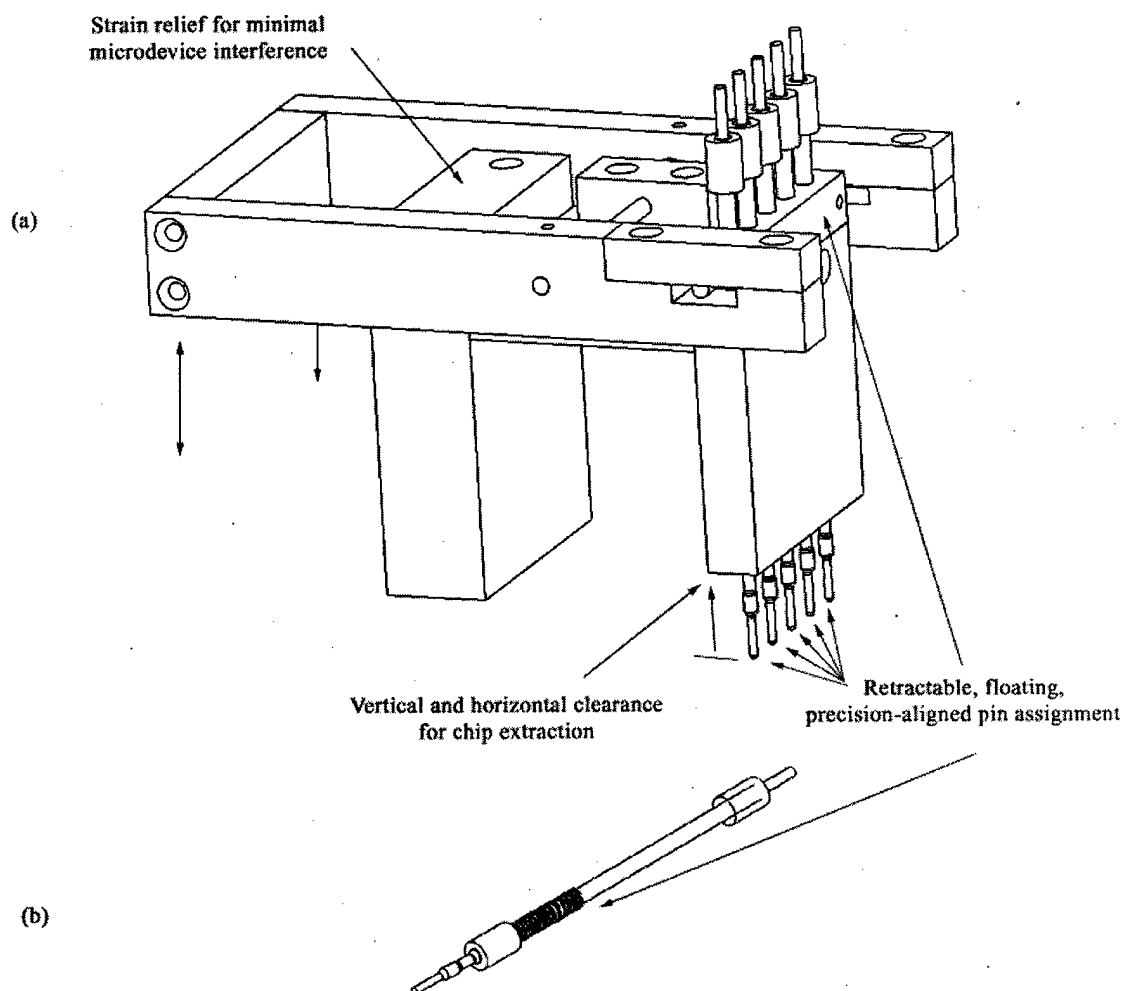


Figure 4-24 Electrical interconnect.

The electrical interconnect was first sketched on paper with detailed design then performed using SolidWorks 98 [79]. Final schematics for all parts were then sent out of house to Aerodyne Engineering in Renton, Washington for fabrication. Figure 4-25

4.7 Design and Fabrication of the Fluidic Subsystem

This section describes the design and fabrication of the fluidic subsystem decoupled into the MEMS microfluidic device and fluidic interconnect. All microfluidic devices were first sketched on paper and then in AutoCAD LT 98 [16]. The fluidic interconnect was first sketched on paper and then detailed design performed using SolidWorks 98 [79]. Soft lithography protocols will also be examined.

4.7.1 MEMS Microfluidic Device

Figure 4-26 shows an isometric view of a MEMS microfluidic device.

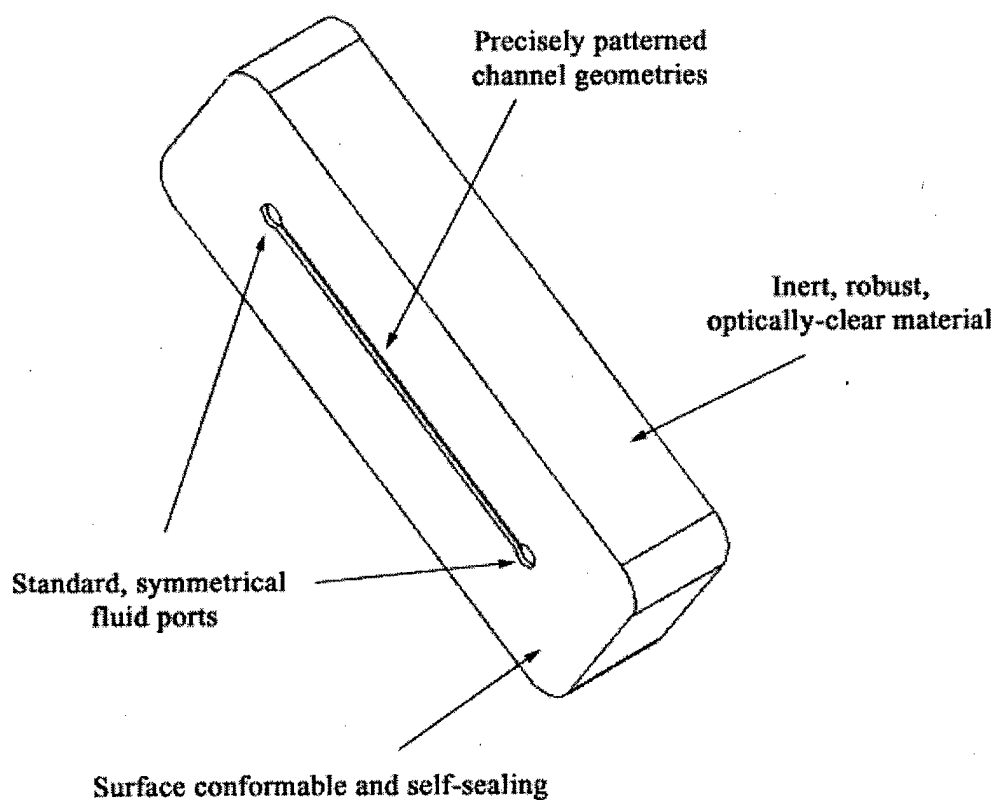


Figure 4-26 MEMS microfluidic device.

The design incorporates standard, symmetrical fluid ports. Precisely defined fluid port locations allow for ease of integration with the electrical and optical subsystems of the microanalytical system. This design may be used as a generalized static and/or flow chamber. Any channel of desired geometry and shape may be designed and incorporated into the device under the constraints of the standardized fluid ports. In summary, the design fully satisfies the functional requirements given by, .

- Standard, symmetrical fluid ports that easily interface with the outside world,
- Precisely patterned channel geometries that are dynamic so any conceivable channel geometry and shape can be used,
- Inert, robust, optically-clear substrate material made from PDMS, and
- Comformable surface that is self-sealing due to the excellent properties of PDMS.

Considerable mention should be made of the enabling microfabrication capabilities that polydimethylsiloxane (PDMS) possess. The excellent qualities of PDMS are discussed by Qin, Xia, and Whitesides [72, 117]. Briefly, these properties are:

- It is an elastomer and conforms to the surface of the substrate over a relatively large area,
- It has elastic characteristics so it can be released easily even from complex and fragile structures,
- It can be deformed reversibly and repeatedly without permanent distortion or relaxation of features,
- It can be molded at a scale suitable for optical applications (with feature sizes in the range of .1 to 10 μm) with high fidelity,
- It is optically transparent down ~ 300 nm,

- It is durable and chemically inert, and
- It is non-toxic, commercially available and inexpensive.

4.7.2 *Characteristic Fluid Flow Velocities*

Determination of the proper channel geometry depends primarily on achieving practical fluid flow velocities, and, therefore, discussion of characteristic fluid flow velocities is appropriate. Fluid mechanics play a vital role in any flow chamber system design. Determination of appropriate channel geometries depends on the resulting fluid flow velocity profiles and their anticipated effect on the biological fluids and processes within the chamber.

The mean fluid flow velocity, \bar{v} , in the microfluidic device depends on:

- Cross-sectional area of the channel with width, l , and depth, d ,
- Syringe pump step frequency, ω ,
- Syringe pump volume, c , and
- Syringe pump resolution, r .

The mean fluid flow velocity, \bar{v} , is the flow rate divided by the channel cross-sectional area. It is desired to determine the resulting mean fluid flow velocity under various settings of these parameters. Typically, though, the desired mean flow velocity, \bar{v} , is first chosen based upon either particle velocity or wall shear criterion. Then the flow rate is determined based on channel cross-sectional area. This, in turn, dictates the necessary pump settings.

The parameters are inherently confined to the following ranges due to biofluidic reasons.

- Cross-sectional area The limits on channel width are bounded by the diffraction limit of light used to pattern the channel while the upper limit is determined by the available area contained in the reserved fluidic region of the microelectrical device and special air bubble entrapment concerns, $-\infty < l \leq 4\text{ mm}$. Channel depth limits are determined by the bounds of the SU-8 epoxy-based photoresist to pattern the channels, $1\mu\text{m} \leq d \leq 500\mu\text{m}$.
- Mean fluid flow velocity The maximum range of practical flow velocity in order to observe particles in the flow under a microscope was determined to be, $0 < \bar{v} \leq 2\text{ mm/sec}$. This selection was made based on the knowledge that one electrode group of the microelectrode device is 2 mm in width. A particle travelling at 2 mm/sec traverses this distance in 1 second.
- Syringe pump step frequency The limits on the step frequency as determined by the Kloehn Syringe Drive Module 50300 are $40 \leq \omega \leq 10,000\text{ steps/sec}$.
- Syringe pump volume The limits as determined by available syringes for the Kloehn Syringe Drive Module 50300 are $25\mu\text{L} \leq c \leq 50\text{mL}$.
- Syringe pump resolution The limit as determined by the highest available step resolution for the Kloehn Syringe Drive Module 50300 is $r = 48,000:1$.

Taking these limitations under consideration, we can now determine the mean fluid flow velocity according to Eqs. 4.2 - 4.5. First, fluid step rate, α , which measures the dispense volume for each cycle of the syringe pump is given by,

$$\alpha = \frac{c}{r}, \quad 4.2$$

where c is the syringe volume and r pump resolution.

The fluid flow rate, γ , is then given by,

$$\gamma = \alpha \omega, \quad 4.3$$

where α is the fluid step rate and ω the step frequency.

A useful intermediate calculation is the total dispense time defined as,

$$t = \frac{c}{\gamma}, \quad 4.4$$

which characterizes the amount of time a syringe of certain volume, c , can be completely dispensed at a fluid flow rate of γ .

Finally, the mean fluid flow velocity is given by,

$$\bar{v} = \frac{\gamma}{A}, \quad 4.5$$

where A is the cross-sectional area of the channel given by,

$$A = ld. \quad 4.6$$

Table 4.3 shows the mean fluid flow velocities taking into account all of these limitations. The mean flow velocities shown in grey imply that they have been excluded from the available process space due to the requirement that $\bar{v} \leq 2$ mm/sec. Additional unforeseen requirements may further limit the process space. A surface plot is shown in Figure 4-27 to graphically illustrate the available process space.

Table 4.3 Example of fluid flow velocity calculation with parameters as shown. The mean flow velocities in grey are those that pertain to values excluded from the process space due to the requirement that $\bar{v} \leq 2$ mm/sec.

Channel Width:	0.5	(mm)								
Syringe Volume:	25	(uL)								
Pump Resolution:	48000	(steps)								
Fluid Step Rate:	0.0005	(uL/step)								
Channel Depth (mm):			0.001	0.005	0.01	0.025	0.05	0.1	0.25	0.5
Cross Sectional Area (mm ²):			0.0005	0.0025	0.0050	0.0125	0.0250	0.0500	0.1250	0.2500
Aspect Ratio (unitless):			500.00	100.00	50.00	20.00	10.00	5.00	2.00	1.00
Step Frequency	Fluid Flow	Dispense								
(step/sec)	Rate	Time								
	(uL/sec)	(sec)	Mean							
			Flow Velocity							
			(mm/sec)							
40	0.02	1200.00	41.67	8.33	4.17	1.67	0.83	0.42	0.17	0.08
50	0.03	960.00	52.08	10.42	5.21	2.08	1.04	0.52	0.21	0.10
100	0.05	480.00	104.17	20.83	10.42	4.17	2.08	1.04	0.42	0.21
150	0.08	320.00	156.25	31.25	15.63	6.25	3.13	1.56	0.63	0.31
200	0.10	240.00	208.33	41.67	20.83	8.33	4.17	2.08	0.83	0.42
250	0.13	192.00	260.42	52.08	26.04	10.42	5.21	2.60	1.04	0.52
300	0.16	160.00	312.50	62.50	31.25	12.50	6.25	3.13	1.25	0.63
350	0.18	137.14	364.58	72.92	36.46	14.58	7.29	3.65	1.46	0.73
400	0.21	120.00	416.67	83.33	41.67	16.67	8.33	4.17	1.67	0.83
450	0.23	106.67	468.75	93.75	46.88	18.75	9.38	4.69	1.88	0.94
500	0.26	96.00	520.83	104.17	52.08	20.83	10.42	5.21	2.08	1.04
550	0.29	87.27	572.92	114.58	57.29	22.92	11.46	5.73	2.29	1.15
600	0.31	80.00	625.00	125.00	62.50	25.00	12.50	6.25	2.50	1.25
650	0.34	73.85	677.08	135.42	67.71	27.08	13.54	6.77	2.71	1.35
700	0.36	68.57	729.17	145.83	72.92	29.17	14.58	7.29	2.92	1.46
750	0.39	64.00	781.25	156.25	78.13	31.25	15.63	7.81	3.13	1.56
800	0.42	60.00	833.33	166.67	83.33	33.33	16.67	8.33	3.33	1.67
850	0.44	56.47	885.42	177.08	88.54	35.42	17.71	8.85	3.54	1.77
900	0.47	53.33	937.50	187.50	93.75	37.50	18.75	9.38	3.75	1.88
950	0.49	50.53	989.58	197.92	98.96	39.58	19.79	9.90	3.96	1.98
1000	0.52	48.00	1041.67	208.33	104.17	41.67	20.83	10.42	4.17	2.08

**Surface Plot of Mean Fluid Flow Velocity with Frequency
and
Channel Depth for 500 μm Channel Width**

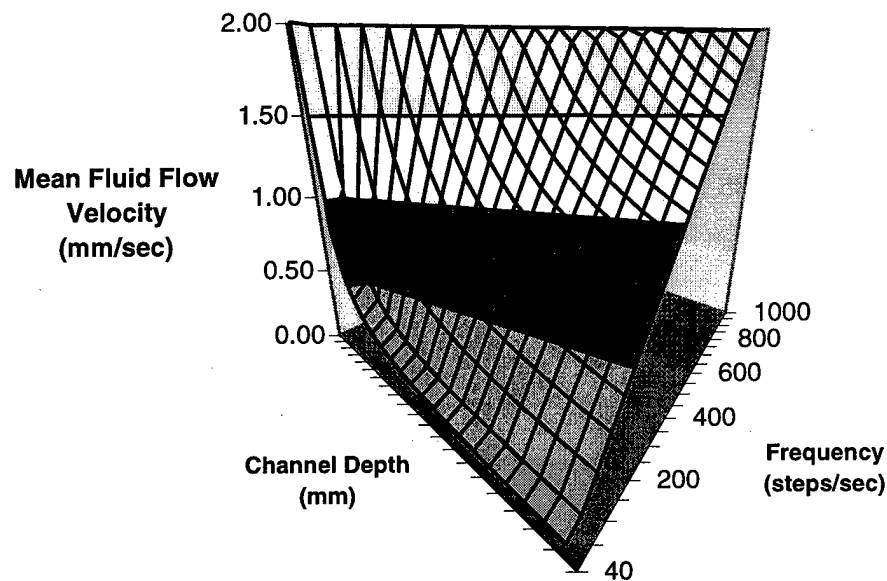


Figure 4-27 Surface plot of mean fluid flow velocity as function of channel depth and pump frequency for a fixed channel width of 500 μm .

4.7.3 Selected Channel Geometries

Three different channel shapes termed Straight, Loop, and Zigzag (Figure 4-28) were designed and fabricated for purposes of this research all at the following channel dimensions:

- Geometry #1 - 500 μm wide, 25 μm deep,

- Geometry #2 - 500 μm wide, 50 μm deep, and
- Geometry #3 - 500 μm wide, 100 μm deep.

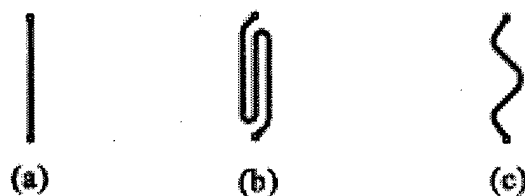


Figure 4-28 Channel shapes: (a) Straight (b) Loop (c) Zigzag.

4.7.4 Soft Lithography Method of Replica Molding

According to Qin and Whitesides, in replica molding microstructures are directly formed by casting and curing a UV curable polymer against an elastomeric mold [72]. This method is effective for replicating feature sizes ranging from several centimeters to ~ 30 nm. Molding against an elastomeric PDMS master has several advantages. First, the elastomer can make conformal contact with a substrate; it can also be released easily, even from complex and fragile structures. Secondly, PDMS provides a surface with low interfacial free energy and low reactivity. As a result, the polymers being molded do not adhere irreversibly to or react with the surface of PDMS. Thirdly, the deformation of PDMS can be controlled easily by mechanical compression, bending, and stretching. Microfabrication based on molding is remarkable for its simplicity, for its economy, and for its fidelity in transferring the patterns from the mold to the polymeric structures that it forms [72].

For purposes of this research, a dual replica molding process is used. PDMS was first cast against a rigid master mold structure patterned on a silicon wafer from SU-8 epoxy-based negative photoresist. This transferred the pattern from the master mold to the PDMS. While this newly cast PDMS part could potentially be used as the

microfluidic device, the process was taken one important step further. This newly cast PDMS then became the master mold against which a two-part room temperature curable polyurethane was cast as described by Qin and Whitesides [72]. This transferred the pattern from the PDMS to the polyurethane. The polyurethane then became the master mold against which PDMS could be cast again to fabricate future structures. This additional step is important for three reasons:

- 1) Many master molds can be made quickly and cheaply using the PDMS and two-part polyurethane. The original master mold made from SU-8 epoxy-based resin patterned on a silicon wafer can be stored or archived for future use.
- 2) The polyurethane master mold is robust and rigid so it can be machined, and
- 3) The polyurethane master mold is robust and rigid so it serves as a rigid substrate against which to cast.

In this research, the master mold consisted of various channel structures as shown in Figure 4-28 patterned on a silicon wafer with SU-8 epoxy-based negative photoresist. This pattern transfer essentially follows the same procedure as that detailed for photolithography. The photomask was first designed on paper and then in AutoCAD LT 98 [16]. Figure 4-29 shows these designs as a photonegative version of the actual mask used.

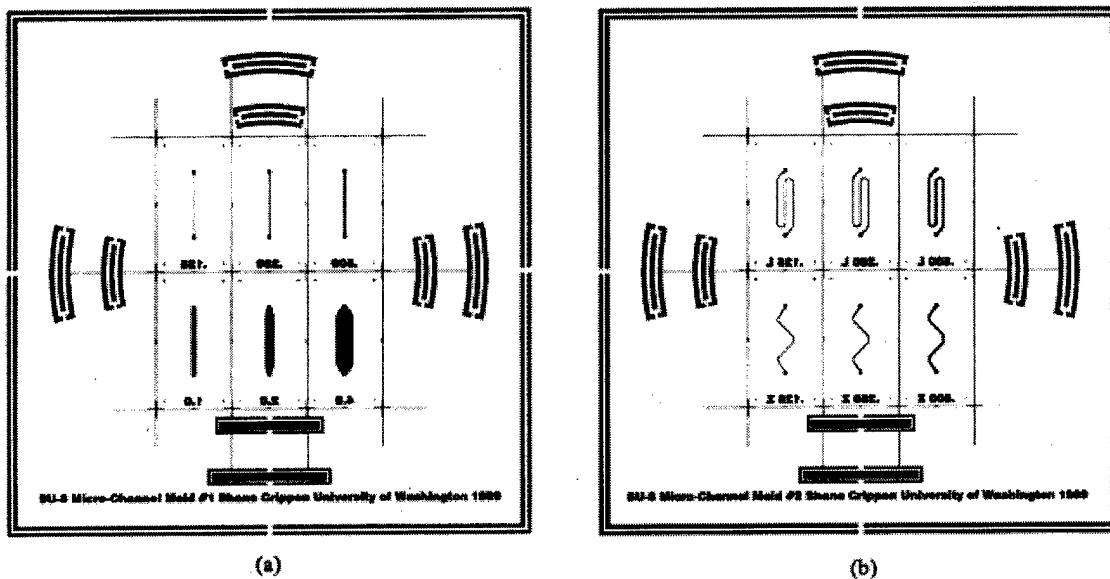


Figure 4-29 SU-8 photomasks (positive) as designed in AutoCAD LT 98 and subsequently used for pattern transfer to silicon wafer with SU-8 epoxy-based photoresist.

The resulting design was transferred to film using services available from Publication Services located at the University of Washington. Figure 4-30 shows a sheet of photomasks that were cut out and used in conjunction with a Qunitel 2001 4" Aligner similar to that shown in Figure 4-30.



Figure 4-30 Sheet of photomasks (negative) designed to transfer the microfluidic device channel patterns with SU-8 epoxy-based negative photoresist onto a silicon wafer using a Quintel 2001 4" Aligner located in the Washington Technology Center's Microfabrication Laboratory at the University of Washington.

Figure 4-31 shows the resulting SU-8 patterned silicon wafers.

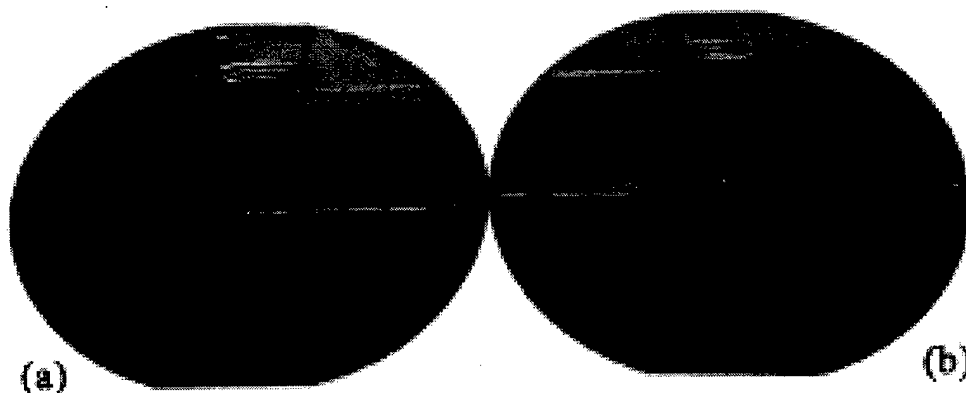


Figure 4-31 SU-8 master mold: (a) Straight channel design (b) Loop and Zigzag channel design.

These wafers were then diced with the Tempress 601 Dicing Saw as shown in Figure 4-23 to remove the individual channel patterns which were then bonded to a 3" glass disk. This assembly served as the original master mold to initially cast the PDMS against.

Initial pattern transfer was performed by casting PDMS against the SU-8 master mold. This transferred the microfluidic device channel pattern from the master mold to the PDMS. A technique implemented here ensured a virtually flat casting surface on the backside by sandwiching the SU-8 master mold and poured PDMS between flat 3" glass disks. A virtually flat surface ensured subsequent casting stages with zero deformation.

The PDMS mold was then used to cast polyurethane. This transferred the pattern from the PDMS mold to the polyurethane which then became the master mold. This master mold was machined to ensure planar surfaces and to insert 22 gauge wire posts in the location of the fluid ports. Silastic[®] tubing could then slide over these posts to serve as input and output fluid ports. Polyurethane molds are quickly and cheaply made and so in many cases are preferable over PDMS and SU-8 master molds.

The polyurethane master mold served as one half of a molding system. The other necessary half was designed in house using SolidWorks 98 and fabricated out of house from 6061 T-6 aluminum by Aerodyne Engineering in Renton, Washington. Figure 4-32 shows how the mold system fits together to cast the PDMS microfluidic device.

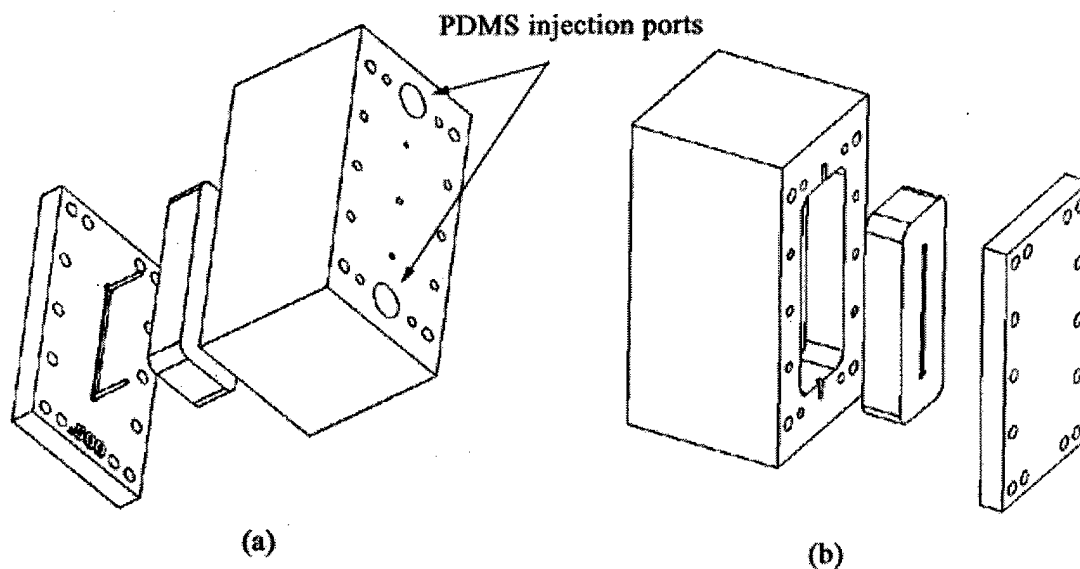


Figure 4-32 Two different views of the mold system composed of the polyurethane mold bottom, the cast PDMS microfluidic device, and the 6061 T-6 aluminum mold top.

The system is comprised of the polyurethane mold bottom, the cast PDMS microfluidic device, and the 6061 T-6 aluminum mold top. PDMS is injected into the mold cavity via the labeled injection ports. Other design features include vent holes and mounting holes. Figure 4-33 shows the actual system as designed and fabricated for purposes of this research.

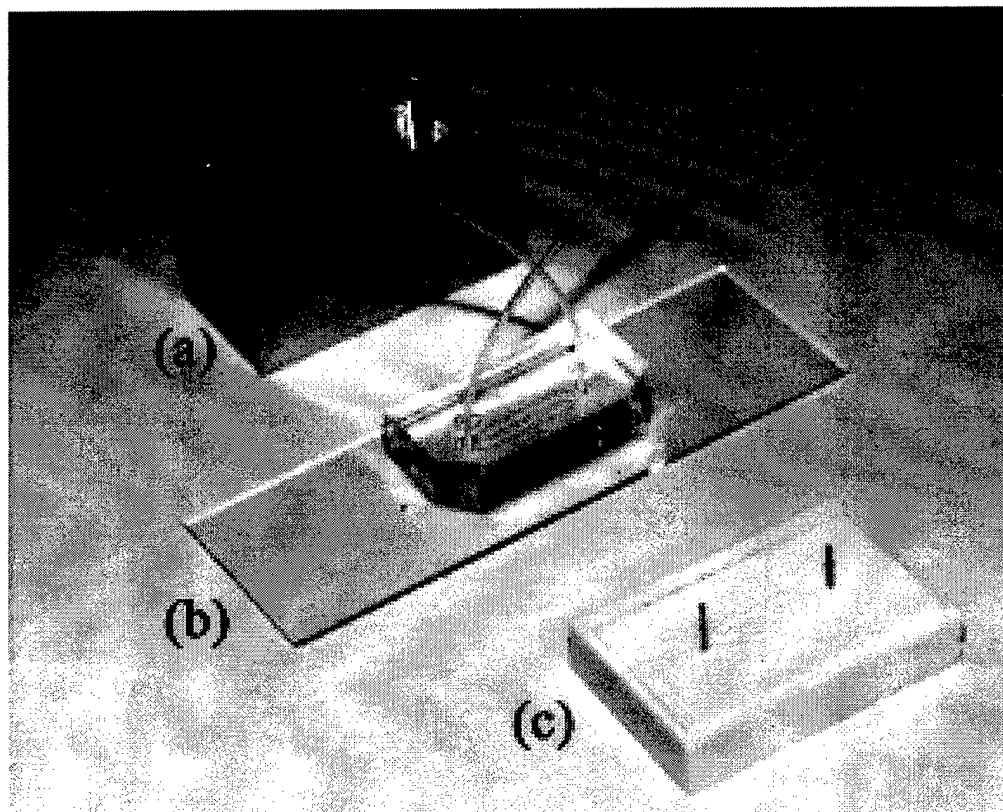


Figure 4-33 Micromolding system: (a) 6061 T-6 aluminum mold top (b) Casted PDMS microfluidic device(c) Polyurethane mold bottom.

Figure 4-34 shows all the elements of the molding process. Each of these components was designed and fabricated in house for purposes of this research.

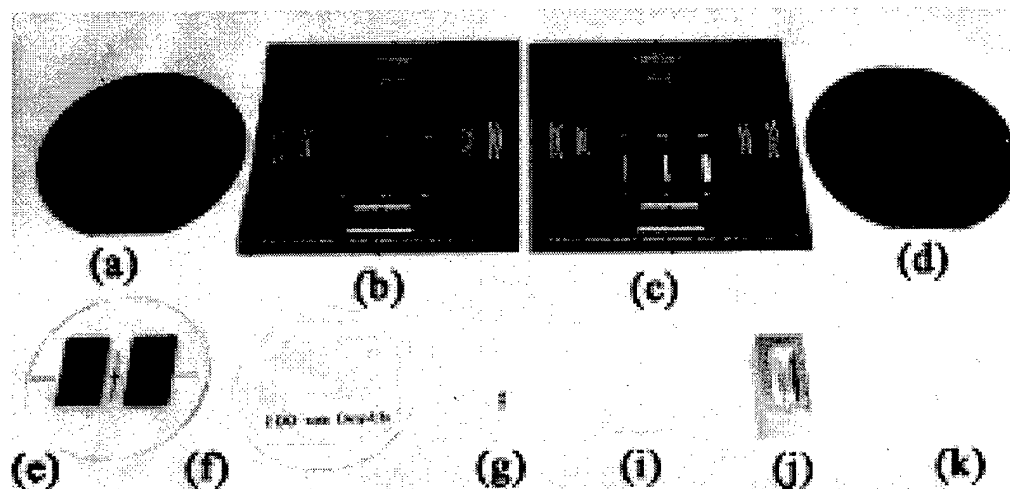


Figure 4-34 Elements of the molding process: (a) SU-8 Loop and Zigzag master mold (b) Photomask for Loop and Zigzag channels (c) Photomask for Straight channels (d) SU-8 Straight Master Mold (e) SU-8 Master Molds bonded to 3" glass disk (f) Initial pattern transfer to PDMS (g) Secondary pattern transfer to polyurethane which served as working master mold (i) polyurethane after machining operations (j) Mold top fabricated from 6061 T-6 aluminum (k) The cast microfluidic device with desired channel pattern. All components were designed and fabricated in house for purposes of this research.

4.7.5 SU-8 Process and Protocols

This section describes SU-8 lithographic process and protocols. Lorenz has been heavily involved in characterization and application of SU-8 [47-49]. According to Lorenz, SU-8 is a negative, epoxy-based, near UV photoresist first developed by IBM. This high-aspect-ratio photoresist lends itself well to MEMS applications, packaging, micromolds, spacers, etc. The key property that makes SU-8 so attractive for ultrathick resist applications is its very low optical absorption in the near-UV range. This leads to a relatively good exposure dose that is uniform over the entire resist thickness, which gives rise to vertical sidewall profiles and hence good dimension control over the entire

structure height. Another ideal property of SU-8 is its low substrate/wafer stress that typically results from thick resist coatings.

The SU-8 chemicals used for purposes of this research were purchased from MicroChem, Corp. (Newton, MA, USA) and include the following as shown in Figure 4-35: 1) SU-8 2 Viscosity Resist, 2) SU-8 5 Viscosity Resist, 3) SU-8 10 Viscosity Resist, 4) SU-8 25 Viscosity Resist, 5) SU-8 50 Viscosity Resist, 6) SU-8 Developer, 7) Remover PG, and 8) C-BL Thinner.

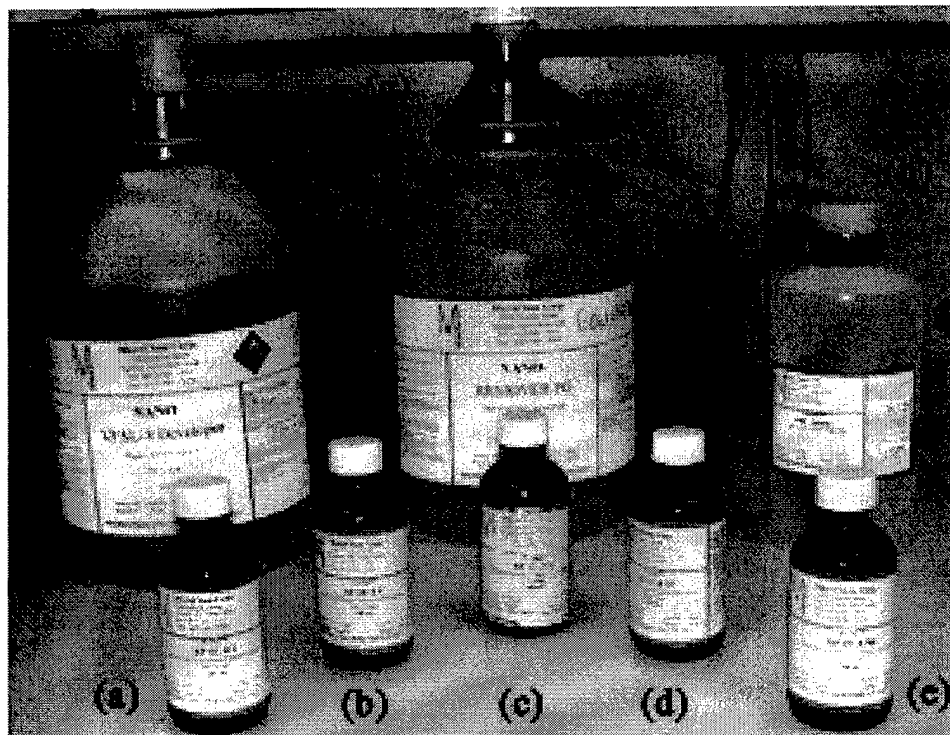


Figure 4-35 SU-8 Photoresist and associated processing chemicals as used in this research: (a) SU-8 2 Viscosity Resist (b) SU-8 5 Viscosity Resist (c) SU-8 10 Viscosity Resist (d) SU-8 25 Viscosity Resist (e) SU-8 50 Viscosity Resist (f) SU-8 Developer (g) Remover PG (h) C-BL Thinner.

Each viscosity has its own thickness and spin speed profile. High spin speeds spread the resist out across the wafer in a thinner layer which results in thinner structures. The

viscosity used also determines the possible pattern thickness. SU-8 50 is a thicker resist than the SU-8 2 and, consequently, results in thicker structures. Patterns up to 500 μm can be patterned with the SU-8 50 while patterns down to 1 μm can be patterned with the SU-8 2.

Figure 4-36 shows a typical thickness and spin speed curve for SU-8 25 as provided by the MicroChem, Corp.

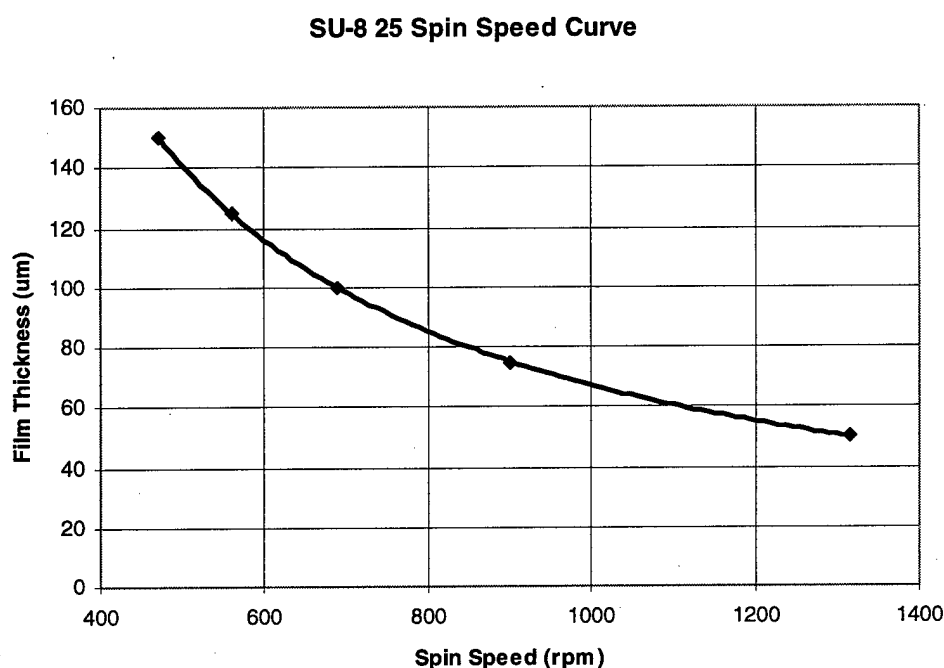


Figure 4-36 Thickness and spin speed curve for SU-8 25 as provided by MicroChem, Corp.

Figure 4-36 reveals important features. The curve in general is nonlinear. A steep portion and shallow portion of the curve exists. Film thickness is very sensitive to spin speed in the steep portion and very insensitive in the shallow region. It is desirable to operate in the shallow portion of the curve to minimize the variational effects of spin speed that may result with different spin equipment.

4.7.6 SU-8 25 Characterization: Bias Point and Linearization Methods

MicroChem, Corp. also provides protocols for soft and hard-bake times, exposure times, and development times. Through efforts of this research, the spin speed curves and subsequent protocols provided by MicroChem, Corp were determined to be inaccurate, or at the very least not applicable to facilities used in this research. As a result, characterization of SU-8 photoresists for desired film thickness was required. What follows is a summary of this characterization for only SU-8 25 followed by a general survey of all five resist viscosities.

It was desired to pattern structures for subsequent use as the master mold for the microfluidic device of 1, 10, 25, 50, and 100 μm . The selected viscosity for the desired film thickness was determined such that only spin speeds in the shallow regions of the spin speed curves were used to minimize operational sensitivity. The following shows the resist viscosities used to do this:

- SU-8 2 for 1 μm patterns,
- SU-8 5 for 10 μm patterns,
- SU-8 10 for 25 μm patterns,
- SU-8 25 for 50 μm patterns, and
- SU-8 50 for 100 μm patterns.

All protocols for spin speed and processing as provided by the MicroChem, Corp. were initially used to pattern structures on silicon wafers at 50 μm . Three important results were discovered.

- 1) The spin speed curve was inaccurate. Using the provided protocols, a spin of 1315 rpm resulted in an average film thickness of 52.5 μm for a percent error of 5.1 %.

- 2) The soft-bake time was inadequate resulting in the coated wafer sticking to and destroying the photomask and itself.
- 3) The exposure time was inadequate resulting in dramatic adhesion problems.

Efforts were made to better characterize SU-8 25 resist. First, the recommended soft-bake times were doubled for the SU-8 25 viscosity resist and tripled for SU-8 50 viscosity resist. Exposure times were adjusted anywhere from double the recommended exposure time for thicker resists to 15 times the recommended exposure time for the thinner resists. The reader may skip ahead to Table 4.4 for a summary of these results. A detailed discussion of the correction for film thickness now follows.

Initial attempts to account for film thickness error employed the bias point method where the spin speed curve as provided by MicroChem, Corp. is shifted up by the difference between the desired film thickness and average resulting thickness. This is a bias point adjustment that assumes the entire curve may be fit through the simple addition of a bias to the film thickness. Extrapolation of this bias point curve results in a new spin speed of 1378 rpm for a film thickness of 50 μm . Figure 4-37 shows the spin speed curve shifted up by 2.5 μm . Using 1378 rpm as the spin speed, an average film thickness of 48.3 μm resulted in an error of 3.4 %. This initial adjustment reduced the error, but was still deemed unacceptable.

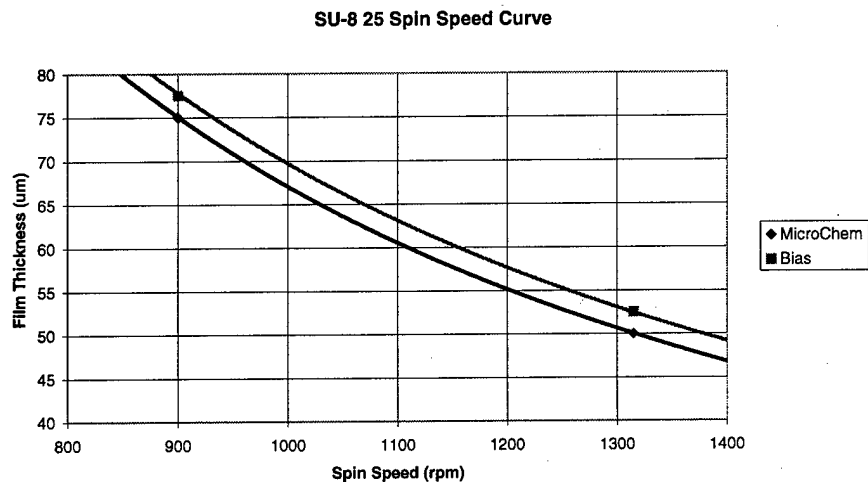


Figure 4-37 Bias point spin speed curve for SU-8 25 resist.

With two experimental data points, the spin speed curve could be linearized about 50 μm as shown in Figure 4-38.

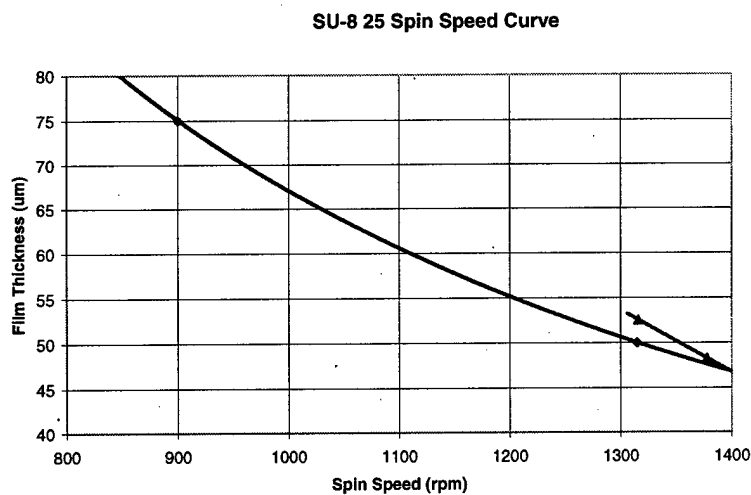


Figure 4-38 Linearized spin speed curve about 50 μm based on two experimental data points.

Extrapolation of this linearized curve results in a new estimated spin speed of 1353 rpm for a film thickness of 50 μm . Using 1353 rpm as the spin speed, an average film thickness of 49.9 μm resulted which is within 1 % of 50 μm . A linearized equation for this extrapolation is given as,

$$\text{Film Thickness} = -0.0687(\text{Spin Speed}) + 142.98. \quad 4.7$$

4.7.7 General Characterization for all SU-8 Resists

Table 4.4 shows the operational parameters as determined through this research for patterning structures at the desired thickness. The bias point and linearized procedures were carried out for all SU-8 resist viscosities. Table 4.4 only shows the final required spin speed should one desire to pattern structures at these thicknesses. It is, however, noted that the properties of photoresists change with shelf life times and appropriate quality control checks are always required.

Table 4.4 Operational protocols for patterning desired film thickness with SU-8 photoresist.

Desired Thickness (um)	SU-8 Resist	Spin Speed (rpm)	Soft-Bake Time (minutes)	Exposure Time (seconds)	Hard-Bake Time (minutes)	Development Time (minutes)	Actual Thickness (um)
1	2	4923	1/1	105	1/1	1	1.01
10	5	1755	1/3	112	1/2	2	9.92
25	10	1649	3/6	125	1/3	4	24.83
50	25	1353	5/30	140	1/5	6	49.9
100	50	1763	10/50	228	1/10	10	100.12

4.7.8 Fluidic Interconnect

Figure 4-39 illustrates the design features of the fluidic interconnect. The electrical interconnect was first sketched on paper and then extensively revised in SolidWorks 98 [79]. Final schematics for all parts were then sent to Aerodyne Engineering in Renton, Washington for fabrication.

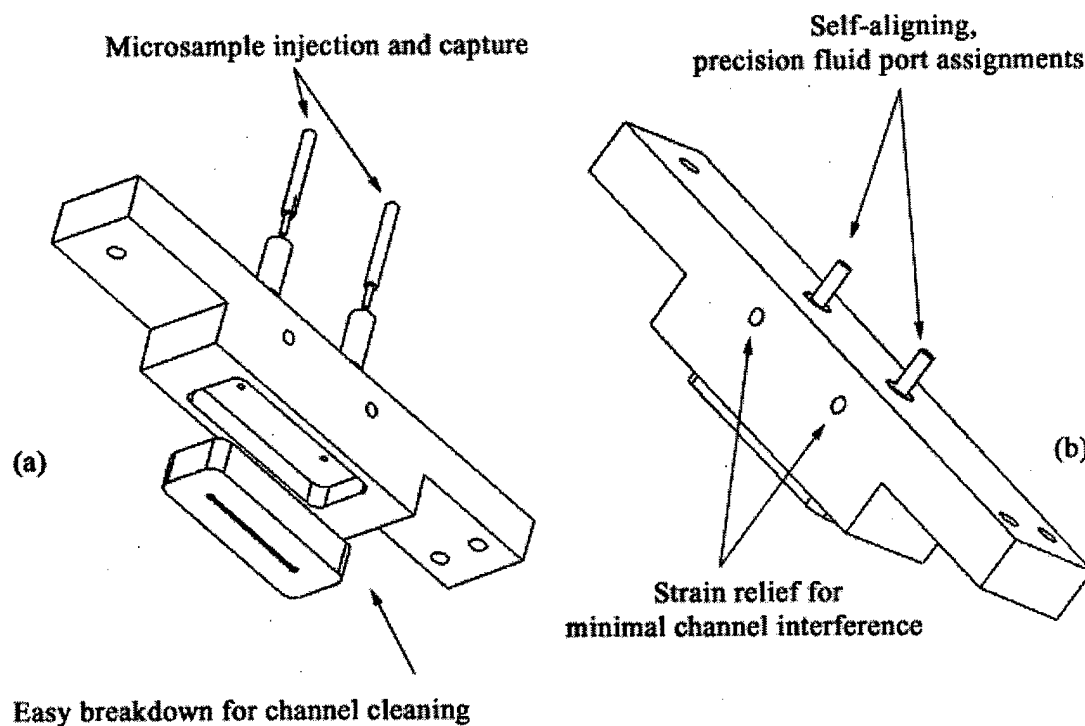


Figure 4-39 Microfluidic assembly highlighting the unique design features: (a) Exploded isometric view (b) Collapsed isometric view.

4.8 Design and Fabrication of the Microscope Interface Platen

The microscope interface platen is the platform upon which the electrical and fluidic subsystems were fixed. The platen was first sketched on paper and then extensively revised in SolidWorks 98 [79]. Final schematics for all parts were then sent out of house to Aerodyne Engineering in Renton, Washington for fabrication. Figure 4-40 illustrates the important features of the platen.

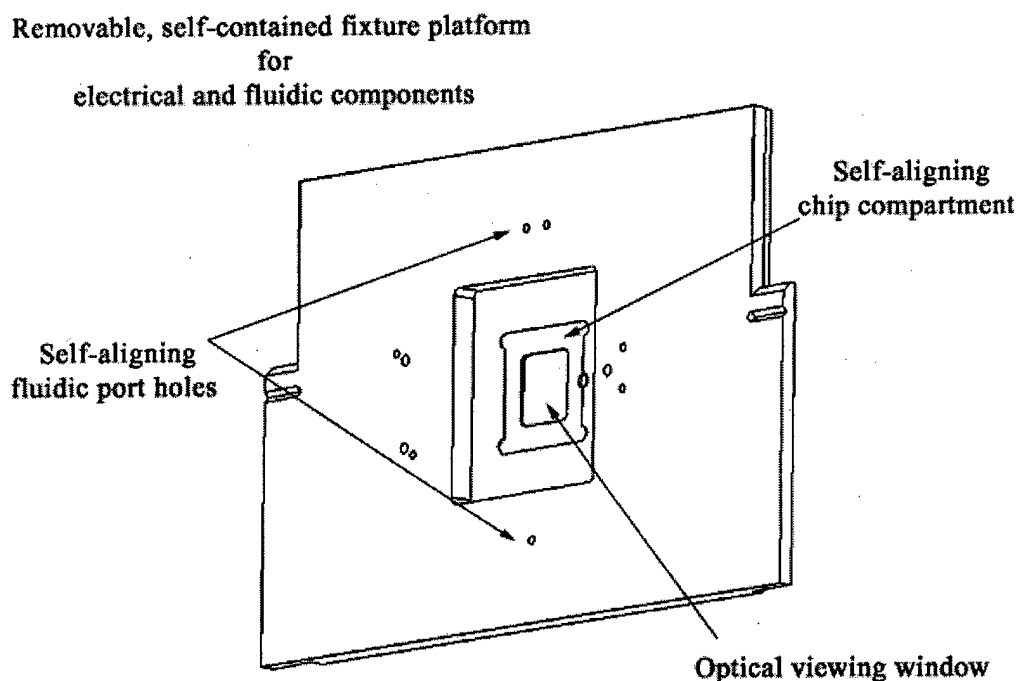


Figure 4-40 Optical mechanical interface isometric highlighting unique design features.

4.9 Fluidic Sample Preparation

DNA sample preparation mirrored that used by Asbury and van den Engh [2]. λ phage DNA of 48.5 kb was purchased from USB Corp. (Cleveland, OH, USA) and as well as λ phage DNA from Promega Corp. (Madison, WI, USA) along with 4.4 kb pBR322 Vector DNA and ~100–600 base Herring sperm DNA. YOYO-1 iodide purchased from Molecular Probes (Eugene, OR, USA) in concentrated form at 1 mM served as the fluorescent label.

The stock USB Corp. λ phage DNA was initially stored in a highly concentrated form at 425 $\mu\text{g/mL}$ in a 10 mM Tris–buffer solution of 10 mM Tris–HCl (pH 7.8), 10 mM NaCl, and 1 mM EDTA. The concentrated stock DNA was then diluted to 5 $\mu\text{g/mL}$ in 150 mL

aliquots with a Tris-buffer solution of 10 mM Tris, 12.5 mM NaCl , and 1 mM EDTA. The stock YOYO-1 iodide was initially concentrated at 1 mM. A small amount was then diluted to 10 μ M.

The final solution was prepared by addition of a dH₂O, 5 μ g/mL DNA, and 10 μ M YOYO-1 iodide in the ratio 47:2:1 (dH₂O: DNA: YOYO-1) resulting in the following final concentrations: 200 ng/mL DNA, 0.4 mM Tris, 0.5 mM NaCl, and 0.04 mM EDTA.

Samples of this solution at sufficient volume to fill the microfluidic device channel of the microfluidic device were drawn into a 1 cc syringe. This sample was then injected into the microfluidic device channel with both input and output ports clamped to prevent fluid flow. The microfluidic device channel directed the sample over the electrode arrays of the microelectrode device. The fluorescently labeled DNA could then be observed using the Zeiss Axiovert 135 epi-fluorescent microscope under the application of applied electric fields.

4.10 Summary

This chapter presented the design method of decoupling as applied to the design, fabrication, and use of the microanalytical system in this research. The microanalytical system was decoupled into three subsystems: the electrical subsystem, the fluidic subsystem, and the optical subsystem. Designs were carried out using 2 and 3 dimensional computer aided drawing programs, AutoCAD LT 98 and SolidWorks 98. The MEMS microelectrode and microfluidic devices were all fabricated in house using photolithography and soft photolithography techniques. Replica molding capabilities enabled rapid prototyping for MEMS microfluidic mold assemblies.

The next chapter will present the experimental results obtained in this research using the microanalytical system as presented in this chapter.

5 Data Collection

This chapter describes experimental data collection methods used along with subsequent experimental results observed during course of this research. First, the characteristic frequency response of microelectrical devices is presented. Important separation performance trends sensitive to the effect of dielectric medium and electrode thickness are discussed. Images showing DNA trapping on parallel and castellated electrode arrays demonstrate this phenomenological dependency on frequencies ranging from the low frequency region around 30 Hz to the high frequency region around 1 MHz. It is demonstrated that the frequency and magnitude of the applied electric field determines the dielectric response and subsequent concentration patterns in DNA trapping.

5.1 Characteristic Frequency Response of Microelectrical Devices

Dielectrophoretic trapping forces and, thus, dielectrophoretic trapping efficiency is linked to the frequency response of the microelectrical system. Therefore, characterizing the system provides a valuable tool for understanding device performance. The microelectrical system consists of an array of parallel electrode structures. Analysis and modeling of this system as a lumped parameter circuit is considered in the Data Analysis and Reduction chapter. In this chapter, only the results of the frequency response collection will be reported.

5.1.1 *Measuring Frequency Response*

Figure 5-1 (a) shows the experimental set up used to measure the system frequency response. This configuration differs from actual experimental conditions used in DNA trapping, see Figure 5-1 (b), in that the measured electrode is tied to ground through a high impedance sensing oscilloscope. When measuring the system frequency response, the grounded electrode becomes effectively a floating potential electrode. Voltage measurements taken from this electrode are referenced from a common ground. Under experimental conditions of DNA trapping, however, the grounded electrode does not

float, it is held to ground. Regardless of the configuration, the frequency response characterizes the ability of the system to hold a threshold electric field potential across interelectrode gap. The system looks like a short-circuit from input to output if the majority of the input is recovered at the output. The system looks more like an open-circuit due to capacitive effects if little input signal is recovered at the output. Furthermore, both configurations contain a dielectric medium between electrodes.

The system frequency response describes the input-output gain and phase-angle relationships as a function of frequency. System gain is measured in units of decibals,

$$dB = 20 \log \left(\frac{V_{out}}{V_{in}} \right), \quad 5.1$$

where: V_{in} is the input signal voltage and V_{out} the output signal voltage. An important parameter in frequency response plots is termed the break frequency or critical frequency, ω_c , at which the -3 dB point occurs. The break frequency is, therefore, the frequency at which the output signal falls off by a factor $1/\sqrt{2}$ or -3 dB of the input signal. When the -3 dB point is reached, the average power delivered is one-half its maximum value [61].

The phase-angle between input and output as shown in Figure 5-1 (a) was difficult to observe and subsequently not recorded other than to say that a phase-angle lag existed at low and at high frequencies. A zero phase-angle was observed in the broad band pass region of the frequency response.

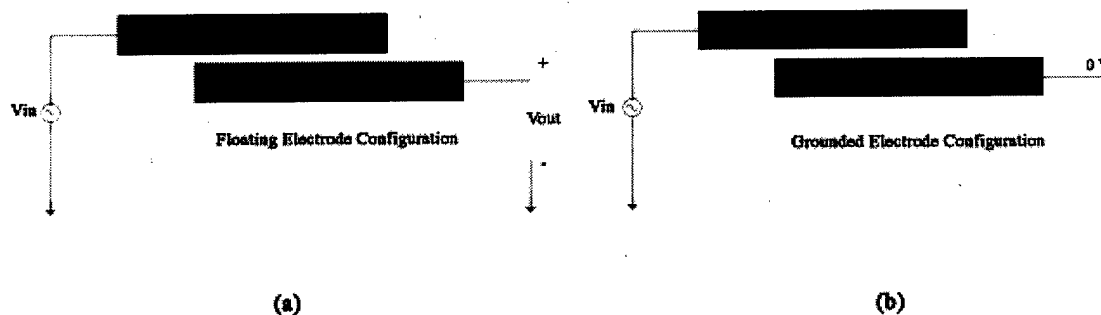


Figure 5-1 Comparison of electrode configurations: (a) Floating Potential Configuration. The adjacent electrode (output signal) floats, and voltage measurements are referenced from a common ground. (b) Grounded Electrode Configuration - This is the standard configuration under conditions of DNA trapping. The adjacent electrode is held to ground.

The dependency of the system frequency response on four different dielectric mediums and at two different electrode thicknesses, t , was investigated. The dielectric mediums are defined as follows.

- Deionized water: dH₂O
- Buffer 1: 0.4 mM Tris, 0.04 mM EDTA, 0.5 mM NaCl
- Buffer 2: 0.9 mM Tris, 0.08 mM EDTA, 1 mM NaCl
- DNA in Buffer 1: 200 ng/mL DNA in Buffer 1

Electrode thicknesses considered were 40 Å and 2000 Å.

5.1.2 Frequency Response as Function of Dielectric Medium for Electrode Thickness of 40 Å

Figure 5-2 shows the system frequency response as a function of dielectric medium using a 40 Å microelectrode device.

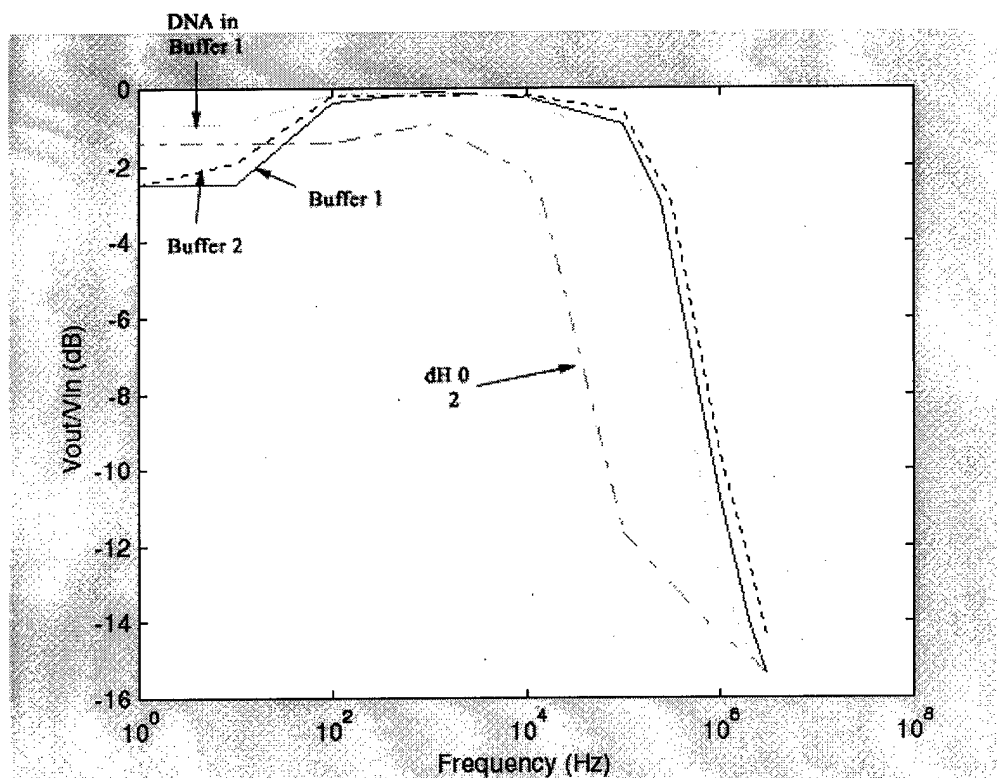


Figure 5-2 Characteristic frequency response as function of dielectric medium using 40 Å microelectrode device.

Figure 5-2 shows three general regions of interest: low frequency region, band pass region, high frequency region. At low frequencies the output signal never falls below the -3 dB point. The presence of DNA in Buffer 1 increases the low frequency gain over that of isolated Buffer 1 and Buffer 2. In the band pass region, nearly the entire input signal is transmitted to the output. Here the system looks like a short-circuit, and little threshold

electric field potential is held across interelectrode gap. At high frequencies, the -3 dB point is nearly the same for all buffer mediums. The dH₂O -3 dB point occurs at an appreciably lower frequency than that of the other dielectric mediums. At frequencies greater than the -3 dB point, the system response drops off at approximately -10 dB/dec and begins to look like an open-circuit. Hence the system is capable of maintaining a high threshold electric field potential across the interelectrode gap at higher frequencies.

5.1.3 Frequency Response as Function of Dielectric Medium for Electrode Thickness of 2000 Å

Figure 5-3 shows the system frequency response as a function of dielectric medium using a 2000 Å microelectrode device.

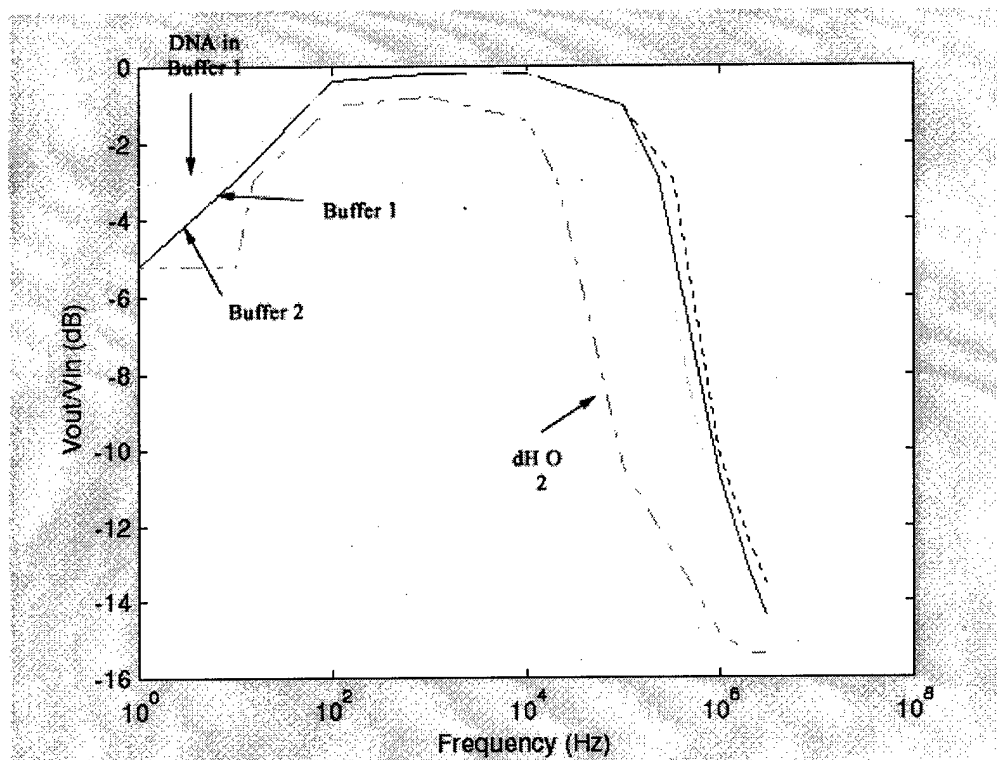


Figure 5-3 Characteristic frequency response as function of dielectric medium using 2000 Å microelectrode device.

Figure 5-3 shows three general regions of interest: low frequency region, band pass region, high frequency region. At low frequencies the output signal falls off below the -3 dB point for all dielectric mediums, and hence the system is capable of maintaining a relatively high threshold electric field potential across the interelectrode gap. The presence of DNA in Buffer 1 increases the low frequency gain over that of isolated Buffer 1 and Buffer 2. In the band pass region, nearly the entire input signal is transmitted to the output. Here the system nearly looks like a short-circuit, and little threshold electric field potential is held across the interelectrode gap. At high frequencies, the -3 dB point is nearly the same for all buffer mediums. The dH₂O -3 dB frequency occurs at an appreciably lower frequency than that of the other dielectric

mediums. At frequencies greater than the -3 dB point, the system response drops off at approximately -10 dB/dec and begins to look like an open-circuit. Hence the system is capable of maintaining a high threshold electric field potential across the interelectrode gap at higher frequencies.

5.1.4 Frequency Response as Function of Electrode Thickness

Figure 5-4 shows the frequency response as a function of electrode thickness, t , in the presence of various dielectric mediums.

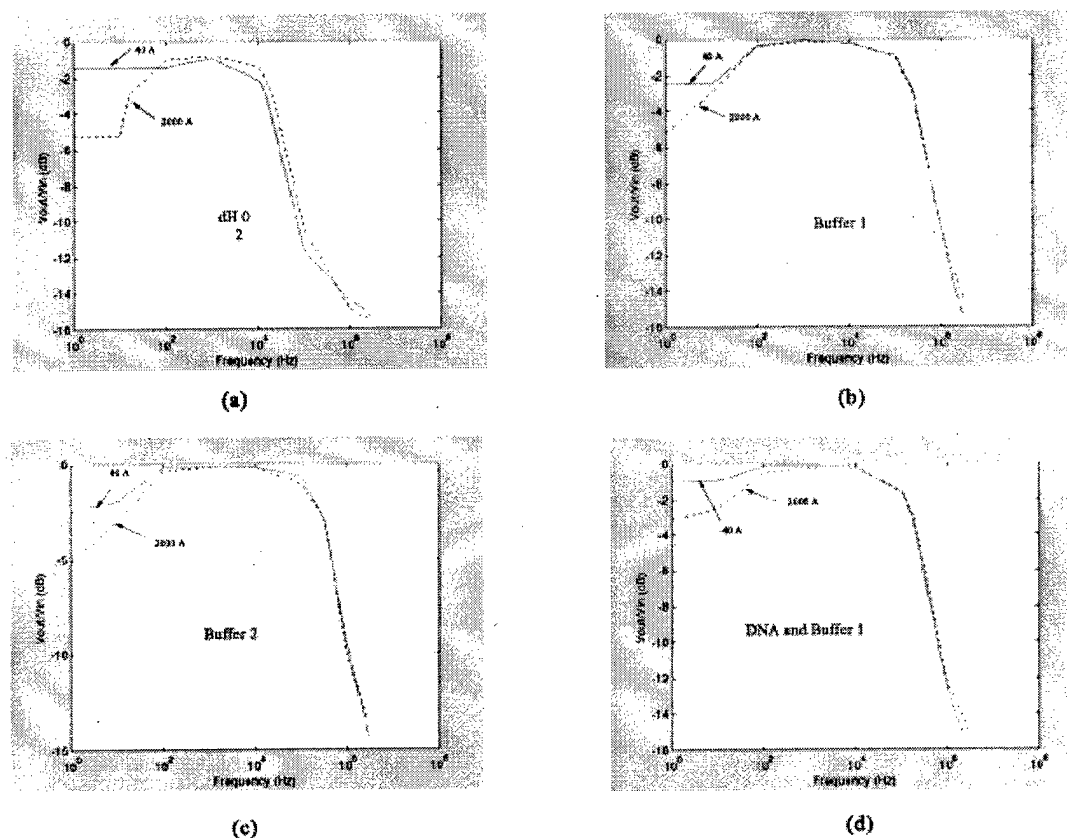


Figure 5-4 Characteristic frequency response as function of electrode thickness in the presence of various dielectric mediums: (a) 40 and 2000 Å microelectrode devices in the presence of dielectric medium, dH₂O. The output signal falls off more quickly for the 2000 Å microelectrode device in the low frequency region. (b) 40 and 2000 Å microelectrode devices in the presence of dielectric medium, Buffer 1. The output signal falls off more quickly for the 2000 Å microelectrode device in the low frequency region. (c) 40 and 2000 Å microelectrode devices in the presence of dielectric medium, Buffer 2. The output signal falls off more quickly for the 2000 Å microelectrode device in the low frequency region. (d) 40 and 2000 Å microelectrode devices in the presence of dielectric medium, DNA in Buffer 1. The output signal falls off more quickly for the 2000 Å in the low frequency region.

Analysis of Figure 5-4 shows that the electrode thickness most impacts the low frequency system response. The thicker electrode is able to maintain a greater threshold electric field potential across the interelectrode gap. Electrode thickness appears to have little effect in the band pass region and in the high frequency region.

5.1.5 Summary of Frequency Response as Function of Dielectric Medium and Electrode Thickness

Table 5.1 provides a summary of the frequency response as a function of dielectric medium for both the 40 and 2000 Å microelectrode devices.

Table 5.1 Summary of frequency response as function of dielectric medium and electrode thickness.

Dielectric Medium	Electrode Thickness					
	40 Angstroms			2000 Angstroms		
	Low Frequency 3 dB Point (Hz)	Band Pass Gain (dB)	High Frequency 3 dB Point (kHz)	Low Frequency -3 dB Point (Hz)	Band Pass Gain (dB)	High Frequency 3 dB Point (kHz)
dH ₂ O	Does not reach	-0.92	14.8	15	-0.92	21.5
DNA in Buffer 1	Does not reach	-0.13	169	10	-0.13	181
Buffer 1	Does not reach	-0.18	244	10	-0.18	241
Buffer 2	Does not reach	-0.18	326	10	-0.18	335

Analysis of Table 5.1 shows a few important trends concerning electrode thickness:

- 1) Low Frequency Region: Output signal drops off more severely for thicker electrodes indicating they are more capable of maintaining higher threshold electric field potentials between electrodes across the gap,
- 2) Band Pass Region: System gain is not effected by electrode thickness in the band pass region, and

- 3) High Frequency Region: Output signal drops off at lower frequencies for thinner electrodes, although the difference is negligible.

Analysis of Table 5.1 also reveals a few important trends concerning buffer concentration:

- 1) Low Frequency Region: Output signal is not affected by buffer concentration,
- 2) Band Pass Region: System gain in the band pass region depends on buffer concentration, and
- 3) High Frequency Region: Output signal drops off at lower frequencies as buffer concentration is decreased.

In summary, the effects of electrode thickness are greatest at low frequencies, and the effects of buffer concentration are greatest at high frequencies.

5.2 DNA Trapping Response for Frequencies up to 100 Hz

This section will present the observed experimental results of DNA trapping response as a function of frequency up to 100 Hz for both the parallel and castellated geometries. Subsequent sections will present trapping response as a function of frequency for other frequencies.

In all cases, figures shown were processed using the contrast/brightness feature of Adobe's Photoshop 5.5. This was necessary in order to improve the printing quality of the figures and better depict the positions of electrodes relative to DNA concentration patterns. Also, at lower frequencies, bleaching of the dye occurred due to electrochemical reactions and caused the fluorescent signal to fade. The behavioral effect of extreme threshold electric field potentials at low frequencies is, therefore, not known due to the inability to detect any fluorescent signal.

5.2.1 Parallel Electrode Structures

Figure 5-5 shows the regions of DNA concentration at these frequencies using a 40 Å gold microelectrode device with interelectrode gap of 30 μm. Black bars along the sides of each image show relative positions of electrodes.

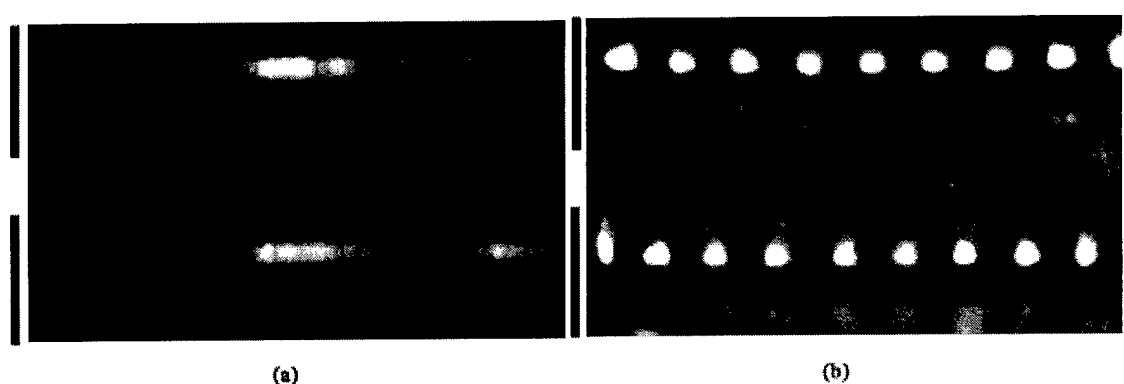


Figure 5-5 DNA trapping at 30 Hz: (a) Parallel Geometry - DNA concentrates above the plane of the electrode along one side, but slightly offset toward the central region of the electrode. (b) Castellated Geometry - DNA concentrates along one side of the electrode in the cavities. Black bars show positions of the electrodes for clarity.

The onset of trapping occurs at approximately 1.5 V_{p-p} for a threshold electric field strength of 25,000 V/m. DNA primarily concentrates over the plane of the electrode near only one edge, but slightly offset toward the central region of the electrode. Trapping occurs above only one edge of the electrode as opposed to both edges of the electrode. This edge seems to correlate to the upstream edge of initial sample injection. Swirling motions of the DNA over the electrode plane can also be observed. An increase in applied voltage causes the fluorescent signal to increase indicating greater concentration of the DNA. DNA is observed to concentrate up to an application of approximately 6 V_{p-p} when electro-chemical reactions cause the fluorescent dye to bleach, and no fluorescent signal can be detected.

5.2.2 *Castellated Electrode Structures*

The onset of trapping occurs at approximately $1.5 V_{p-p}$ for a threshold electric field strength of 25,000 V/m. DNA primarily concentrates in the cavities of the castellated design. At this low voltage, the concentration seems to be greater in the corners of the cavities. Trapping occurs only in the cavities on one side of the electrode. This side seems to correlate to the upstream edge of sample injection. Swirling motions of the concentrated DNA in the cavities can also be observed. Increasing applied voltage causes the cavity to fill with more DNA until the fluorescent signal appears to be uniform within the cavity as opposed to concentration primarily in the corners of the cavity. Electro-chemical bleaching of the fluorescent dye occurs at approximately $6 V_{p-p}$, and no fluorescent signal can be detected.

5.3 DNA Trapping Response for Frequencies Between 100 Hz and 1 kHz

5.3.1 *Parallel Electrode Structures*

Figure 5-6 shows the regions of DNA concentration at these frequencies using a 40 Å gold microelectrode device with interelectrode gap of 30 μm. Black bars along the side of the image show relative positions of electrodes.

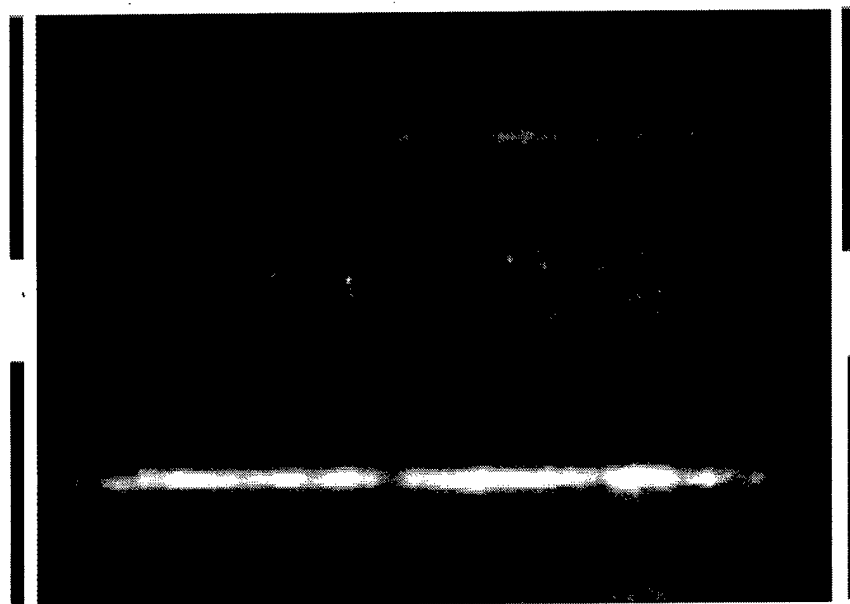


Figure 5-6 DNA trapping at 100 Hz – DNA concentrates above the electrode plane in the central region down the length of the electrode. Black bars show positions of the electrodes for clarity.

The onset of trapping occurs at approximately at $1.5 V_{p-p}$ for a threshold electric field strength of 25,000 V/m. DNA concentrates above the central region of each electrode plane. No trapping is observed near the edges the electrodes. At approximately $3.7 V_{p-p}$, the DNA appears to transition from concentrating over the central region of the electrode plane to near both edges of the electrode. Electro-chemical bleaching of the fluorescent dye occurs at approximately $7 V_{p-p}$, and no fluorescent signal can be detected.

5.3.2 *Castellated Electrode Structures*

No images were collected for the castellated electrode geometry due to a mistake on the part of this author. As a result, the concentration pattern is not uniquely identified. Extrapolation, however, for those observed concentration patterns reported in Chapters

5.2.2 and 5.3.2 indicates that DNA most likely concentrated either over the central region of the electrode or in the cavities at approximately $1.5 V_{p-p}$.

5.4 DNA Trapping Response for Frequencies Between 1 kHz and 10 kHz

This section will present the observed experimental results of DNA trapping response as a function of frequency for frequencies between 1 kHz and 10 kHz for both the parallel and castellated geometries.

5.4.1 Parallel Electrode Structures

Figure 5-7 shows the regions of DNA concentration at these frequencies using a 40 Å gold microelectrode device with interelectrode gap of 30 μm. Black bars along the sides of each image show relative positions of electrodes.

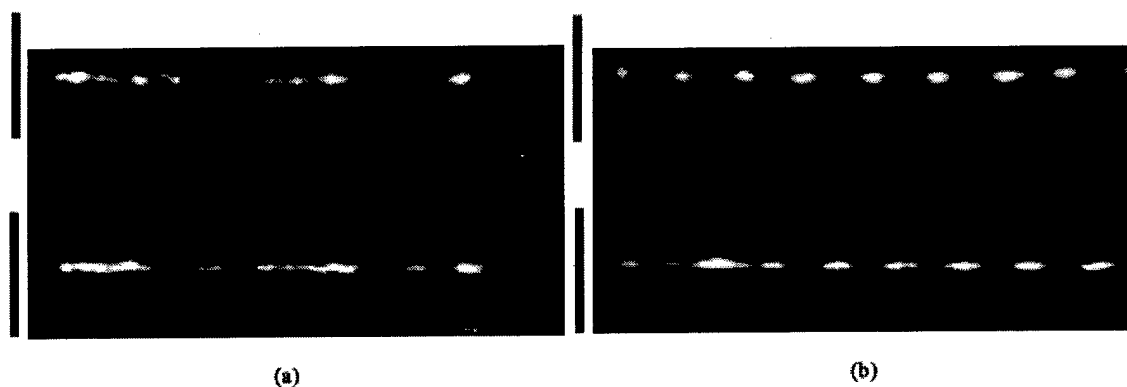


Figure 5-7 DNA trapping at 1 kHz: (a) Parallel Geometry - DNA concentrates above the electrode plane in the central region down the length of the electrode. (b) Castellated Geometry - DNA concentrates above the central region of each electrode plane in dotted patterns that correspond to alignment with the tooth of the respective electrode. Black bars show positions of the electrodes for clarity.

The onset of trapping occurs at approximately $1.5 V_{p-p}$ for a threshold electric field strength of 25,000 V/m. DNA concentrates above the central region of each electrode plane. No trapping is observed near the edges of the electrodes. Further increases in applied voltage increases the fluorescent intensity of the central region of each electrode plane indicating that more DNA is being concentrated in this area. The DNA did not appear to transition from trapping above the central region to near the edges with increasing voltage. Bleaching of the fluorescent dye due to electro-chemical reactions is not observed even at extreme voltages where the maximum available voltage is $20 V_{p-p}$.

5.4.2 *Castellated Electrode Structures*

The onset of trapping occurs at approximately $1.5 V_{p-p}$ for a threshold electric field strength of 25,000 V/m. DNA concentrates above the central region of each electrode plane in dotted patterns that correspond to alignment with the tooth of the respective electrode. No trapping is observed in the cavities of the structures. Further increases in applied voltage increases the fluorescent intensity of the central region of each electrode plane indicating that more DNA is being concentrated in this area. Bleaching of the fluorescent dye due to electro-chemical reactions is not observed even at extreme voltages where the maximum available voltage is $20 V_{p-p}$.

5.5 DNA Trapping Response for Frequencies Between 10 kHz and 100 kHz

This section will present the observed experimental results of DNA trapping response as a function of frequency for frequencies between 10 kHz and 100 kHz for both the parallel and castellated geometries

5.5.1 Parallel Electrode Structures

Figure 5-8 shows the regions of DNA concentration at these frequencies using a 40 Å gold microelectrode device with interelectrode gap of 30 μm. Black bars along the sides of each image show relative positions of electrodes.

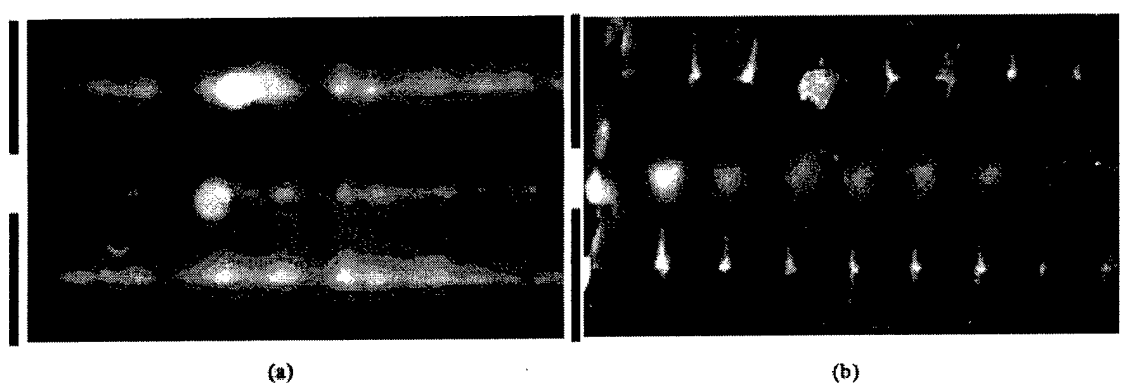


Figure 5-8 DNA trapping at 10 kHz: (a) Parallel Geometry - DNA concentrates above the central region of each electrode plane as well as in the central region of the gap between adjacent electrodes. (b) Castellated Geometry - DNA concentrates above the central region of each electrode plane as well as in the central region of each gap. DNA that concentrates in the central region of each gap does so shifted one cell over from that where the DNA concentrates over the central region of each electrode. Black bars show positions of the electrodes for clarity.

The onset of trapping occurs at approximately 4 V_{p-p} for a threshold electric field strength of 67,000 V/m. DNA concentrates above the central region of each electrode plane as well as in the central region of the gap between adjacent electrodes. The concentration bands were continuous along the length of the electrode and along the length of the gap. Further increases in applied voltage only served to increase the fluorescent signal indicating that more DNA is being concentrated. Bleaching of the fluorescent dye due to

electro-chemical reactions is not observed even at extreme voltages where the maximum available voltage is $20 V_{p-p}$.

5.5.2 *Castellated Electrode Structures*

The onset of trapping occurs at approximately $4 V_{p-p}$ for a threshold electric field strength of 67,000 V/m. DNA concentrates above the central region of each electrode plane as well as in the central region of the gap between adjacent electrodes. This unique concentration pattern is further qualitatively described as follows. DNA that concentrates over the central region of each electrode plane aligns with the tooth of the castellated structure. DNA that concentrates in the central region of each gap does so shifted one cell over from that where the DNA concentrates over the central region of each electrode. The concentration then is not continuous along the length of the electrode and gap, but rather as distinctly patterned concentration spots. Bleaching of the fluorescent dye due to electro-chemical reactions is not observed even at extreme voltages where the maximum available voltage is $20 V_{p-p}$.

5.6 DNA Trapping Response for Frequencies Between 100 kHz and 1 MHz

This section will present the observed experimental results of DNA trapping response as a function of frequency for frequencies between 100 kHz and 1 MHz for both the parallel and castellated geometries

5.6.1 *Parallel Electrode Structures*

The onset of trapping occurs at approximately $8 V_{p-p}$ for a threshold electric field strength of 133,000 V/m. DNA concentrates above the central region of each electrode plane as well as in the central region of the gap between adjacent electrodes. The concentration bands were continuous along the length of the electrode and along the length of the gap. Further increases in applied voltage only served to increase the fluorescent signal

indicating that more DNA is being concentrated. Bleaching of the fluorescent dye due to electro-chemical reactions is not observed even at extreme voltages where the maximum available voltage is $20 V_{p-p}$.

5.6.2 Castellated Electrode Structures

The onset of trapping occurs at approximately $8 V_{p-p}$ for a threshold electric field strength of $133,000 V/m$. DNA concentrates above the central region of each electrode plane as well as in the central region of the gap between adjacent electrodes. This unique concentration pattern is further qualitatively described as follows. DNA that concentrates over the central region of each electrode plane aligned with the tooth of the castellated structure. DNA that concentrates in the central region of each gap does so shifted one cell over from that where the DNA concentrates over the central region of each electrode. The concentration then is not continuous along the length of the electrode and gap, but rather appears as distinctly patterned concentration spots. Bleaching of the fluorescent dye due to electro-chemical reactions is not observed even at extreme voltages where the maximum available voltage is $20 V_{p-p}$.

No images were obtained for these settings due to a mistake on the part of the author.

5.7 DNA Trapping Response for Frequencies Around 1 MHz

This section will present the observed experimental results of DNA trapping response as a function of frequency for frequencies around 1 MHz for both the parallel and castellated geometries

5.7.1 Parallel Electrode Structures

Figure 5-9 (b) shows the regions of DNA concentration at these frequencies using a 40 \AA gold microelectrode device with interelectrode gap of $30 \text{ }\mu\text{m}$. Figure 5-10 (a) shows the effect of applied extreme threshold electric field strengths for relatively long periods of

time where the DNA concentration patterns appear to span the gap between adjacent electrodes. Black bars along the sides of each image show relative positions of electrodes

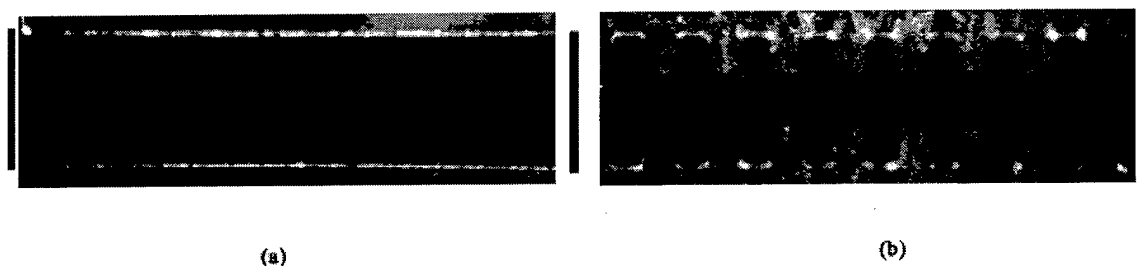


Figure 5-9 DNA trapping at 1 MHz and low threshold electric field strength: (a) Parallel Geometry - DNA concentrates at the edges of the electrodes along the length of both sides of the electrodes. The DNA appears as thin, rigid lines indicating very strong attraction to the electrode edges (b) Castellated Geometry - DNA concentrates at the tips of the teeth along both sides of the electrode. The DNA appears as thin, rigid lines indicating very strong attraction to the tips of the teeth. Black bars show positions of the electrodes for clarity.

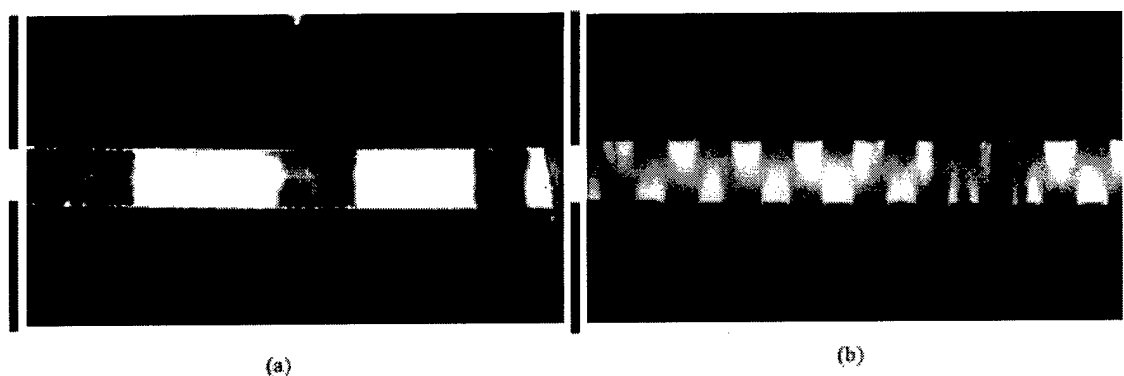


Figure 5-10 DNA trapping at 1 MHz and high threshold electric field strength: (a) Parallel Geometry - DNA concentrates at the edges of the electrodes along the length of both sides of the electrodes. Furthermore, the concentration over time increases such that the DNA concentration pattern spans the gap between electrodes. (b) Castellated Geometry - DNA concentrates at the tips of the teeth along both sides of the electrode. Furthermore, the concentration over time increases such that the DNA concentration pattern almost spans the gap between adjacent electrode teeth. Black bars show positions of the electrodes for clarity.

The onset of trapping occurs at approximately $10 V_{p-p}$ for a threshold electric field strength of 167,000 V/m. DNA concentrates strictly at both edges of each electrode. The appearance of trapping differed significantly from that at lower frequencies as the DNA appears to be held very rigidly at the electrode edges as well as making contact with the electrode edges. As the voltage increases from $10 V_{p-p}$, the trapping ability increases. If these higher trapping voltages were left in place long enough, enough DNA concentrates to the point that the DNA spans the gap between adjacent electrodes. Please reference Figure 5-10 (b) for an image at these settings. Bleaching of the fluorescent dye is not observed even at extreme voltages where the maximum available voltage is $20 V_{p-p}$.

5.7.2 *Castellated Electrode Structures*

The onset of trapping occurs at approximately $10 V_{p-p}$. Please reference Figure 5-9 (a) for an image at these settings. DNA concentrates strictly at the tips of the teeth on both sides of each electrode. The appearance of trapping differed significantly from that at lower frequencies as the DNA appears to be held very rigidly at the tips as opposed to in the cavities of the structure. As the voltage increases from $10 V_{p-p}$, the trapping ability increases. If these higher trapping voltages were left in place long enough, enough DNA concentrates to the point that the DNA spans the gap from tooth to tooth of adjacent electrodes. Bleaching of the fluorescent dye is not observed even at extreme voltages where the maximum available voltage is $20 V_{p-p}$.

5.8 Summary of Trapping Response for DNA

Table 5.2 provides of summary of trapping response as a function of frequency. It denotes the minimum observed trapping voltage as well as a description of the trapping mode.

Table 5.2 Summary of trapping response for DNA.

Frequency	Structure	Minimum Necessary Voltage (Vp-p)	Trapping Location
30 Hz	Parallel	1.5	Over plane of electrode near one edge displaced toward central region of electrode plane
	Castellated	1.5	In cavities, initially in corners at low Vp-p and filled cavity at high Vp-p
100 Hz	Parallel	1.5	Over central region of electrode plane
	Castellated	1.5	Not available
1 kHz	Parallel	1.5	Over central region of electrode plane
	Castellated	1.5	Over central region of electrode plane
10 kHz	Parallel	4	Over central region of electrode plane and in central region of gap
	Castellated	4	Over central region of electrode plane and in central region of gap in dotted pattern corresponding to tooth location
100 kHz	Parallel	8	Over central region of electrode plane and in central region of gap
	Castellated	8	Over central region of electrode plane and in central region of gap in dotted pattern corresponding to tooth location
1 MHz	Parallel	10	At electrode edges and spanning gap at large Vp-p
	Castellated	10	At tooth edges and spanning gap at large Vp-p

5.9 Summary

In this chapter, it was demonstrated that DNA concentration patterns are dependent upon the applied threshold electric field strength and frequency. At frequencies below 1 MHz, DNA was observed to concentrate in minimum field regions occurring over central regions of electrodes and gaps. Only at frequencies near 1 MHz was DNA observed to concentrate at the electrode edges.

These results indicate that DNA undergoes negative dielectrophoresis at frequencies less than 1 MHz. Between 100 kHz and 1 MHz, a transition occurs between negative and positive dielectrophoresis. Above this transition at frequencies near 1 MHz, DNA experiences positive dielectrophoresis.

According to the dielectrophoretic force expression, the Clausius-Mossotti function must then be a complex entity, \underline{K} , which describes a particle that has ohmic and/or dielectric losses and is possibly layered. The sign on $\text{Re}[\underline{K}]$ changes from negative when DNA experiences negative dielectrophoresis to positive when DNA experiences positive dielectrophoresis.

In the next chapter, these observed results will be set in the context of the characteristic frequency response of the microanalytical system and in the context of the dielectric dispersion curve for DNA.

6 Data Analysis and Reduction

Some fundamental questions concerning the mechanics of dielectrophoretic trapping of biological macromolecules such as DNA exist. For example, DNA can be trapped over the span of frequencies studied in this research from as low as 30 Hz to as high as 1 MHz. The characteristic parameters associated with trapping efficiency differ significantly at the two ends of the frequency spectrum in two important aspects.

First, the required threshold electric field strength at low frequencies is significantly less than that at high frequencies. For an interelectrode gap of 30 μm , trapping at 100 Hz requires a threshold electric field strength of 25,000 V/m while trapping near 1 MHz requires 167,000 V/m. This is near a factor of 7 different.

The second important distinction concerns the induced concentration patterns. At low frequencies, DNA concentrates over the central regions of electrodes and gaps. It appears to hover above the plane of the electrode and be loosely trapped resulting in diffuse concentration patterns. At high frequencies near 1 MHz, however, DNA concentrates at both edges of the electrodes. It appears to be very rigidly held as the concentration patterns look rigid and well-defined. Extreme applications of the threshold electric field strength can even concentrate DNA in sufficient numbers that the concentration patterns span the gap between electrodes.

From this discussion, it is seen that the characteristic dielectrophoretic trapping response differs at low frequencies from that at high frequencies. Unfortunately, no explanation for this distinction is known by the author to exist in the available literature. Understanding the basics for these differing regions of behavior will result in an entirely different set of dielectrophoresis applications than those that have already been proposed; this understanding will, furthermore, clearly illuminate an extended fundamental understanding of the underlying biophysical processes present.

This chapter shows that these counter-intuitive distinctions can be explained using knowledge of the physical properties of the biological solutions and of the complete microanalytical and biophysical systems. First the frequency dependent dielectric properties of DNA dictate the observed trapping differences at low and high frequencies. Second, the characteristic frequency response of the microelectrical devices that generate dielectrophoretic trapping forces also dictates the observed trapping differences at low and high frequencies. A model of dielectrophoretic trapping is presented that explains in a qualitative manner the linkage existing between the two extreme ends of this frequency spectrum as well as those frequencies in between. Further, the model and its frequency response explain the observed required threshold electric field potential for DNA trapping.

6.1 Development of Lumped Parameter Circuit Model for Microelectrical Devices

Any system (e.g. electrical, chemical, photonic, mechanical, biological, etc.) has a characteristic frequency response. This frequency response is easily acquired through the input of a signal at various frequencies and subsequent measurement of the resulting output signal. This characteristic frequency response is very informative. This utility was demonstrated in Chapter 5.1.5 when characterizing the characteristic frequency response of microelectrical devices used in this research.

In this section, a lumped parameter circuit model is presented as a first order approximation for the microelectrical devices used in this research. Although this response pertains to the devices used in this research, it is equally applicable to systems used by Washizu, Asbury and van den Engh, Gascoyne, and Wang [2, 3, 36, 37, 39, 40, 93-111, 113-116].

This research further distinguishes itself from prior work via the presented characteristic frequency response of microelectrode devices and subsequent bridge between frequency extremes. Gascoyne and Wang do characterize the frequency response of their systems

and its ramifications. They only studied cells and microbeads, however, and not biological macromolecules such as DNA studied in this research. Furthermore, they only studied behavioral characteristics at frequencies up to 100 kHz and not 1 MHz as in this research. As was demonstrated in Chapter 5.1.5, the system response does not begin to fall off until after 100 kHz when additional interesting results are obtained.

6.1.1 Problem Statement

The proposed model accounts for the observed frequency response over the entire range of relevant frequencies from 10 Hz to 3 MHz. The observed frequency response is generally characteristic of a band pass filter. At low frequencies near dc, the system response moderately falls off. Here the system appears to have significant resistive and capacitive effects attributable to electrode polarization, as will be discussed in Chapter 6.1.2, or attributable to capacitive coupling between electrodes. The degree of drop off is dependent on electrode thickness which can possibly be explained by the characterization of a 40 Å thick electrode as a resistive film and a 2000 Å thick electrode as a conductive trace. The response drops off more for a 2000 Å thick electrode than for a 40 Å thick electrode. In fact, a low pass filter can almost describe the system response of the 40 Å thick electrode because the system response never reaches the -3 dB point. The response does drop off at frequencies near dc, however, and will also be characterized as a band pass filter.

At high frequencies, the system response falls off dramatically (approximately -10 dB/dec) beginning at break frequencies between 169 kHz and 335 kHz primarily depending on dielectric medium as shown in Table 5.1. The break frequency is defined as that frequency at which the -3 dB point occurs. The response continues to fall off after the break frequency and is never observed to level out over the observed high frequency range up to 3 MHz. The system behaves as though it were open circuit and is, thus, capable of maintaining a large threshold electric field strength across the interelectrode gap. This behavior can possibly be attributed to parasitic capacitance.

In the broad band pass region, the input is almost entirely recovered at the output. The broad band pass region exists in the frequency range between approximately 10 Hz at which the lower -3 dB point occurs and 169 kHz to 335 kHz where the upper -3 dB point occurs. Here the system looks like a direct short from input to output. As a consequence, little threshold electric field strength is maintained. This system response can possibly be attributed to behavioral characteristics encountered after the effects of electrode polarization and capacitive coupling in the low frequency range and before the onset of parasitic capacitance in the high frequency range.

6.1.2 Electrode Polarization

Electrode polarization was briefly mentioned in Chapter 2.3.1 as having a significant effect at low frequencies. An excellent and extensive treatment of this important subject was given by several authors in 1992 in the *Annals of Biomedical Engineering* [26, 51-53, 74]. Briefly, according to de Levie, metals are very efficient conductors of electrons, but not ions. On the other hand, aqueous electrolyte solutions are ionic conductors and are hostile to electrons. Consequently, at the interface between a metal and an aqueous electrolyte solution, there is a mismatch in the type of charge carrier used. In the absence of a chemical mechanism to convert one type of charge carrier into the other, the interface behaves as a capacitance. A change in the electronic charge density on the metal side is accompanied by a compensating change in ionic charge density on the solution side, so that electroneutrality is maintained. The two types of charges can come close to each other without the possibility of neutralizing each other. Faradaic processes (interfacial oxidation and /or reduction) provide the only possibility to convert from electronic to ionic charge, or vice versa, and thus enable the continued flow of electricity through the interface [26].

In practice, electrode polarization results in a potential drop across the electrode/solution interface. As a result, the voltage potential the solution experiences is less than that which is applied to the electrodes. In other words, electrode polarization reduces the

threshold electric field potential across the interelectrode gap which in turn reduces the available dielectrophoretic trapping force.

6.1.3 Modeling the Effects of Electrode Polarization

Modeling the effects of electrode polarization is nontrivial. De Levie reports that an expression for the total interfacial admittance is so complicated that it is near meaningless to search for an equivalent circuit representation. In the simplest of cases, the components of an equivalent circuit can be associated with individual physical and/or chemical processes, but this can not be assumed to be the case in general and often can be shown to be incorrect. Consequently, an equivalent circuit should be used only for what it is: a convenient way to represent experimental data in a compact form and an effective means to assess first order model sensitivities to changes in bulk intrinsic model properties. It is not a unique representation of the physical system and, thus, may not fit experimental data well over the entire process space. Experimental data, when possible, should be compared directly with models that incorporate full theoretical modeling in a continuum rather than the potentially distorting intermediary of equivalent circuits [26].

Gascoyne et al. recently reported the experimental effects of electrode polarization in their studies of cell levitation height [44, 98]. By employing negative dielectrophoresis, they were able to levitate cells above an electrode array. The equilibrium cell height depends on the strength of the negative dielectrophoretic trapping force which in turn depends on $\nabla |\overline{E}|^2$ and $\text{Re}[\underline{K}]$. For their cell population, $\text{Re}[\underline{K}]$ achieved maximum negative values at low frequencies and transitioned to maximum positive values at high frequencies. Assuming a constant threshold electric field potential, cell levitation height should be maximal at low frequencies. It should then be slowly reduced during the transition to positive values when the cells are no longer levitated, but instead are attracted to the electrode edges due to positive dielectrophoresis.

Instead, they observed that cell levitation height *increased* during the transition toward positive values of $\text{Re}[\underline{K}]$. The only explanation for this was that the threshold electric field strength increased despite a constant applied voltage. Increasing values of $\nabla|\underline{E}|^2$, therefore, counteracted the decreasing transitional values of $\text{Re}[\underline{K}]$. They realized that electrode polarization was responsible for this phenomenon. At low frequencies, electrode polarization so reduced the threshold electric field potential that despite large negative values of $\text{Re}[\underline{K}]$, the cell levitation height was in fact less than that observed at increased frequencies when $\text{Re}[\underline{K}]$ took on less negative values, but the threshold electric field potential was greater.

Gascoyne et al. then attempted to model the effect of electrode polarization using an ion-based diffusion model developed by Schwan [74]. According to Schwan, the electrode surface impedance, Z_{pol} , that is responsible for electrode polarization can be modeled by,

$$Z_{pol} = R_{pol} + \frac{1}{j2\pi f C_{pol}}, \quad 6.1$$

where the resistive component, R_{pol} , and the capacitive component, C_{pol} , are given as functions of frequency, f , by,

$$R_{pol} \approx f^{-m} \quad \text{and} \quad 6.2$$

$$C_{pol} \approx f^{-(1-m)}. \quad 6.3$$

The term, m , is not constant and takes on values near 0.3 to 0.5 as the frequency increases from below 1 Hz to more than 10 kHz. Gascoyne et al. used $m=0.5$. Updating Eq. 6.1 with Eqs. 6.2 and 6.3 to reflect this frequency dependence gives,

$$Z_{pol} = R_{pol} f^{-0.5} + \frac{1}{j2\pi f C_{pol} f^{-0.5}}. \quad 6.4$$

The impedance of the dielectric medium between electrodes (i.e. the biological solution), according to Schwan, can be modeled by a bulk resistance, R_{bulk} , in parallel with a bulk capacitance, C_{bulk} , according to,

$$Z_{bulk} = \frac{(R_{bulk}) \left(\frac{1}{j2\pi f C_{bulk}} \right)}{\left(\frac{1}{j2\pi f C_{bulk}} \right) + (R_{bulk})} \quad 6.5$$

$$= \frac{R_{bulk}}{1 + j2\pi f R_{bulk} C_{bulk}}$$

As a rough first order approximation, the system containing electrode polarization effects, Z_{pol} , and dielectric medium impedance effects, Z_{bulk} , can then be described as shown in Figure 6-1 and then modeled by a lumped parameter circuit as shown in Figure 6-2 where arrows through the resistive and capacitive elements denote they are frequency dependent.

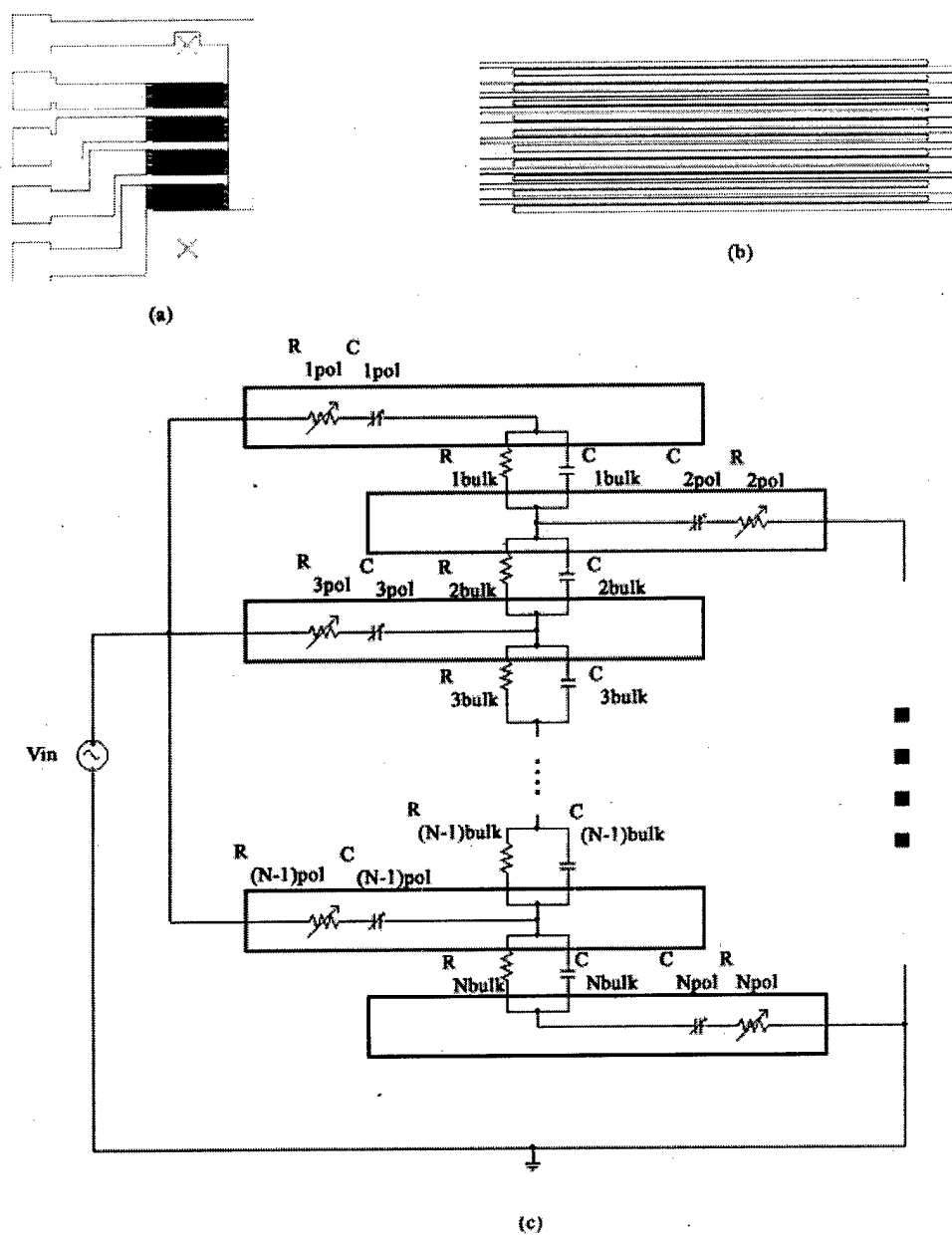


Figure 6-1 System circuit model: (a) Microelectrical Device (b) Detailed view of one electrode group of the microelectrical device (c) Circuit model of microanalytical system.

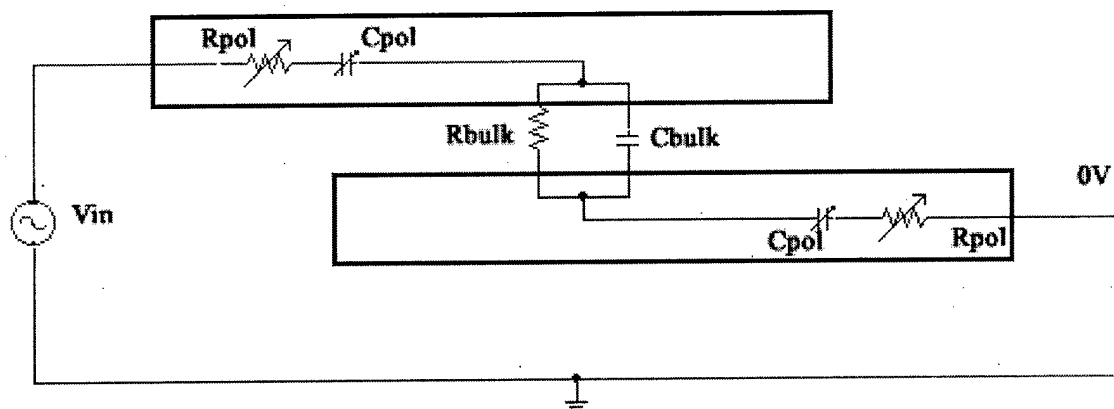


Figure 6-2 Lumped parameter circuit model of microanalytical system.

The total impedance of the lumped parameter circuit between one set of electrodes is then given by,

$$\begin{aligned}
 Z_{total} &= Z_{pol} + Z_{bulk} + Z_{pol} \\
 &= Z_{bulk} + 2Z_{pol} \\
 &= \left(\frac{R_{bulk}}{1 + j2\pi f R_{bulk} C_{bulk}} \right) + 2 \left(R_{pol} f^{-0.5} + \frac{1}{j2\pi f C_{pol} f^{-0.5}} \right)
 \end{aligned} \tag{6.6}$$

where the factor of 2 denotes that both electrodes contribute to electrode polarization.

The polarization function, $p(f)$, is defined by,

$$p(f) = \frac{Z_{bulk}}{Z_{total}}, \tag{6.7}$$

which is nothing more than a voltage divider that determines the transfer function from input to output.

$$\frac{V_{out}}{V_{in}} = p(f) \quad 6.8$$

In this definition, the bulk impedance of the dielectric medium is treated as the load in the circuit shown in Figure 6-3. Note, an important difference exists between the transfer function given in Eq. 6.8 and that measured in this research. In the experimental measurement of frequency response conducted in this research, V_{out} was measured after Z_{bulk} in a floating electrode configuration. This was due to the inability to place the voltage measurement probe in the configuration as presented by Eq. 6.8. Although Eq. 6.8 is still valid for purposes of this research, it must be considered in context.

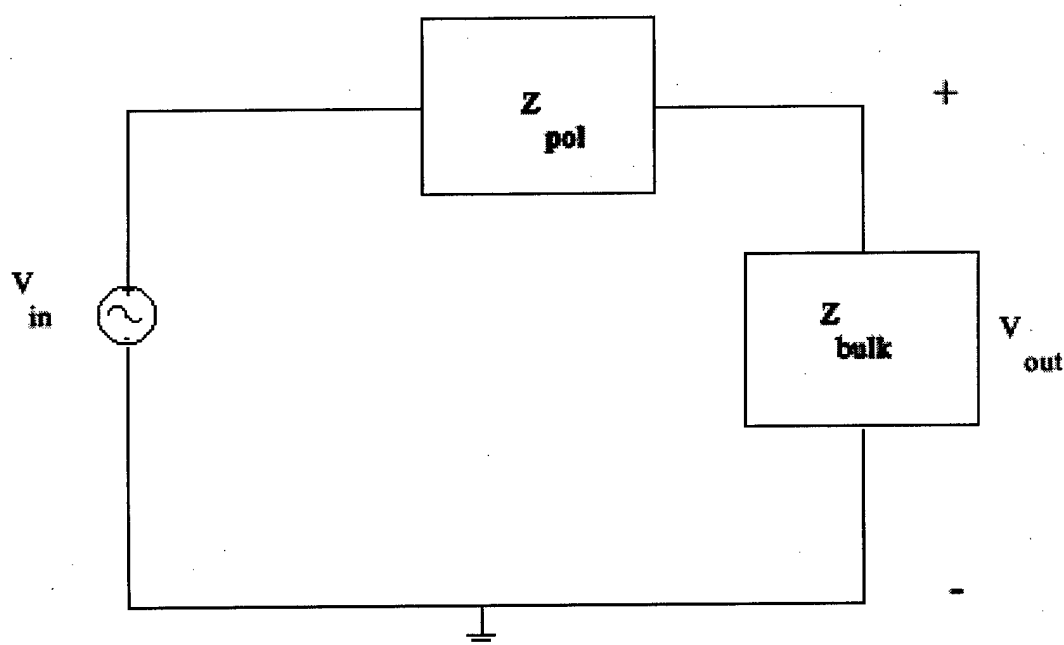


Figure 6-3 Equivalent circuit for Eqs. 6.7 and 6.8.

6.1.4 Electrode Polarization Determines Dependency of Low Frequency System Response on Electrode Thickness

Analysis of electrode polarization indicates one important concept. A voltage drop across the electrode/electrolyte interface as modeled by, Z_{pol} , results in a reduced threshold electric field strength across the interelectrode gap. In the context of the frequency response measured in this research for 40 Å and 2000 Å thick electrodes, the electrode/electrolyte interface potential drop is greatest for the 2000 Å thick electrode. This can be concluded by analysis of Figure 5-4 where the measured output voltage drops off more severely for the 2000 Å thick electrode than for the 40 Å thick electrode at low frequencies. This indicates a greater voltage drop occurs across Z_{pol} for the 2000 Å thick electrode.

This result is counterintuitive for the following reason. A 40 Å thick electrode is characterized as a resistive film while the 2000 Å thick electrode is characterized as a conductive trace. One would expect, therefore, that R_{pol} for the resistive film to be greater than R_{pol} for the conductive trace resulting in a larger Z_{pol} . As a consequence, the greater voltage drop across Z_{pol} should occur for the 40 Å thick electrode.

One reason may exist for this dichotomy. The electrode polarization impedance, Z_{pol} , is given as a combination of two terms in Eq. 6.4 due to resistive and capacitive effects. The impedance due to capacitive effects, therefore, must be greater for the 2000 Å thick electrode. In other words, C_{pol} for conductive traces must be smaller than C_{pol} for resistive films to give an overall greater Z_{pol} for conductive traces. Perhaps this can be explained according to the original assumption of discontinuity in current carriers at the electrode/electrolyte interface. More study is needed to better characterize the electrode polarization effect for thin films.

6.2 Proposed Model of DNA Trapping

Analyzing the dielectrophoretic behavior of DNA in the mutual context of the measured system frequency response, Figure 5-1, and that of the proposed dielectric dispersion curve, Figure 2-4, results in a consistent model of DNA trapping as shown in Figure 6-4.

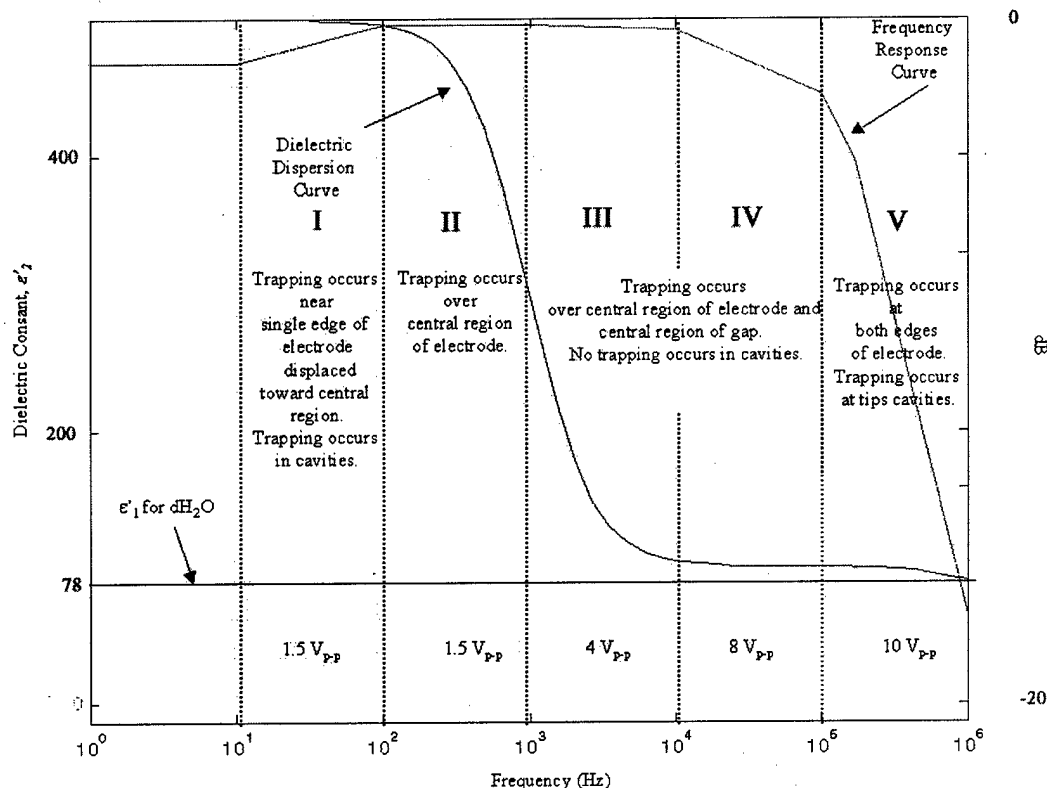


Figure 6-4 Model of DNA trapping.

The regions labeled, I-V, in Figure 6-4 are qualitatively described in the following manner:

Region I: DNA experiences negative dielectrophoresis. Little threshold electric field potential is maintained across the interelectrode gap resulting in small values for $\nabla|\vec{E}|^2$.

The permittivity of DNA, however, well exceeds that of dH_2O resulting in a large value

of $\text{Re}[\underline{K}]$. This combination of $\nabla|\overline{E}|^2$ and $\text{Re}[\underline{K}]$ is sufficient to generate large values of the dielectrophoretic trapping force, \overline{F}_{DEP} . The contribution of $\text{Re}[\underline{K}]$ to \overline{F}_{DEP} is large while the contribution of $\nabla|\overline{E}|^2$ is small.

Region II: DNA experiences negative dielectrophoresis. Little threshold electric field potential is maintained across the interelectrode gap resulting in small values for $\nabla|\overline{E}|^2$. The permittivity of DNA begins to fall with the dispersion centered at approximately 1 kHz, although, the exact placement can vary. The permittivity, however, still well exceeds that of dH₂O resulting in still relatively large values of $\text{Re}[\underline{K}]$. This combination of $\nabla|\overline{E}|^2$ and $\text{Re}[\underline{K}]$ is sufficient to generate large values of the dielectrophoretic trapping force, \overline{F}_{DEP} . The contribution of $\text{Re}[\underline{K}]$ to \overline{F}_{DEP} is large while the contribution of $\nabla|\overline{E}|^2$ is small.

Region III: DNA experiences negative dielectrophoresis. Little threshold electric field potential is maintained across the interelectrode gap resulting in small values for $\nabla|\overline{E}|^2$. The permittivity of DNA still continues to fall through the tail end of the dielectric dispersion resulting in reduced values for $\text{Re}[\underline{K}]$. A corresponding increase in the necessary trapping voltage, V_{p-p} , is observed. This combination of $\nabla|\overline{E}|^2$ and $\text{Re}[\underline{K}]$ is sufficient to generate large values of the dielectrophoretic trapping force, \overline{F}_{DEP} . The contribution of $\text{Re}[\underline{K}]$ to \overline{F}_{DEP} is large while the contribution of $\nabla|\overline{E}|^2$ is small.

Region IV: DNA experiences a transition from negative to positive dielectrophoresis. The threshold electric field potential is observed to increase resulting in increasing values for $\nabla|\overline{E}|^2$. The permittivity of DNA reaches a constant value slightly above that of water

resulting in small values of $\text{Re}[\underline{K}]$. A corresponding increase in the necessary trapping voltage, V_{p-p} , is observed. This combination of $\nabla|\overline{E}|^2$ and $\text{Re}[\underline{K}]$ is sufficient to generate large values of the dielectrophoretic trapping force, \overline{F}_{DEP} . The contribution of $\text{Re}[\underline{K}]$ to \overline{F}_{DEP} is small while the contribution of $\nabla|\overline{E}|^2$ is large.

Region V: DNA experiences positive dielectrophoresis. The threshold electric field potential continues to increase resulting in increasing values for $\nabla|\overline{E}|^2$. DNA undergoes another dispersion in this region, and the permittivity of DNA is almost equal to that of dH₂O resulting in very small values for $\text{Re}[\underline{K}]$. A corresponding increase in the necessary trapping voltage, V_{p-p} , is observed. This combination of $\nabla|\overline{E}|^2$ and $\text{Re}[\underline{K}]$ is sufficient to generate large values of the dielectrophoretic trapping force, \overline{F}_{DEP} . The contribution of $\text{Re}[\underline{K}]$ to \overline{F}_{DEP} is very small while the contribution of $\nabla|\overline{E}|^2$ is very large.

A particle that exhibits both negative and positive dielectrophoresis requires that the Clausius-Mossotti function, K , be a complex quantity, \underline{K} . A complex Clausius-Mossotti function, in turn, requires that ohmic and/or dielectric losses be present in the particle. As a result, DNA must be modeled as a single or layered particle with ohmic and/or dielectric losses. Calculating theoretical values of $\text{Re}[\underline{K}]$, then, is nontrivial. A first order approximation that treats \underline{K} as a real quantity is given by,

$$K = \frac{\epsilon'_2 - \epsilon'_1}{\epsilon'_2 + 2\epsilon'_1}, \quad 6.9$$

where ϵ'_1 and ϵ'_2 are the dielectric constants of the dH₂O and DNA, respectively. This first order approximation, however, cannot account for the observed negative and

positive dielectrophoresis characteristics of DNA. Using this approximation, DNA would always exhibit positive dielectrophoresis. Therefore, when considering regions where the system exhibits ohmic and/or dielectric losses to a significant extent, the more rigorous complex Clausius-Mossotti function,

$$\underline{K} = \frac{\underline{\epsilon}_2 - \underline{\epsilon}_1}{\underline{\epsilon}_2 + 2\underline{\epsilon}_1}, \quad 6.10$$

must be used where $\underline{\epsilon}_1$ and $\underline{\epsilon}_2$ are the complex permittivities accounting for losses present in the medium and particle, respectively. DNA may then experience both negative and positive dielectrophoresis.

6.3 Summary

This chapter presented a model of DNA trapping that links results reported in the available literature by Washizu and Asbury and van den Engh. The model more completely defines the process space by accounting for frequencies between low frequencies as studied by Asbury and van den Engh and high frequencies as studied by Washizu. It was observed that DNA exhibits both negative and positive dielectrophoresis dependent upon frequency. This behavior requires that DNA be modeled as a single or layered particle with ohmic and/or dielectric losses.

7 Conclusion

This thesis presents a body of work having content in the areas of device and experimental design, theoretical and literature based analysis, and laboratory validation and extension of scientific knowledge. Specifically, the design and fabrication of a MEMS-based microanalytical system for dielectrophoresis studies of biological macromolecules was reported. The design and use of this microanalytical system was dictated according to a need defined by the Genomation Laboratory located at the University of Washington.

This chapter presents the findings and contributions of this research to:

- 1) The development and acquisition of experimental infrastructure for the Genomation Laboratory and
- 2) The fundamental knowledge of dielectrophoresis of biological macromolecules such as DNA.

7.1 Development and Acquisition of Experimental Infrastructure

A MEMS-based microanalytical system was designed and fabricated to serve as a flexible platform for the study of electrical and biofluidic interactions. This system is comprised of an electrical subsystem, fluidic subsystem, and optical subsystem. The development and acquisition of these subsystems resulted in significant contributions to the experimental infrastructure within the Genomation Laboratory:

- Methods for design and fabrication of microelectrode devices upon which future user defined electrode structures may be patterned and subsequently characterized,
- Robust electrical interconnect that allows for the simultaneous application of excitation signals on a single microelectrode device,

- Methods for design and fabrication of microfluidic polymer devices using SU-8 epoxy-based photoresist and microtransfer replica molding,
- Robust fluidic interconnect for microsample injection and capture that mitigates fluid handling problems and results in consistent experimental parameters,
- Methods for fluorescent labeling and subsequent observation of biological macromolecules, and
- Analytical microscopy station consisting of a Zeiss Axiovert 135 epi-fluorescent microscope, Dage-MTI 3-Chip Cooled CCD Color Camera, image processing workstation, and associated recording equipment.

7.2 Dielectrophoresis of DNA

This section describes the contribution of this research to the understanding of the dielectrophoretic behavior of DNA. Such understanding was concluded through a methodical process of discovery involving theoretical and literature based analysis coupled with laboratory validation.

7.2.1 *Process of Discovery*

The theory of dielectrophoresis was elucidated according to the effective moment method of Jones [45]. It was important to establish that a particle can undergo both negative and positive dielectrophoresis depending on frequency of the applied electric field. Not all particles exhibit such behavior. Only particles that show ohmic and/or dielectric loss can exhibit such behavior as required by the real part of the complex Clausius-Mossotti function, $\text{Re}[\underline{K}]$. Particles experiencing negative dielectrophoresis are attracted to minimum electric field regions while those experiencing positive dielectrophoresis are attracted to maximum electric field regions.

Pohl and Jones demonstrated that the dielectrophoretic force is strongly dependent on the electrode geometry and dimension [45, 46, 70, 71]. Electrodes can be fashioned such that clearly defined minimum and maximum electric field regions exist. A common electrode geometry in use today is the interdigitated, parallel electrode array. Through extensive field distribution modeling, Gascoyne and Asbury and van den Engh identified that minimum electric field regions occur over the central region of the electrode and between electrodes over the gap while maximum electric field regions occur at the electrode edges [2, 40]. A unique extension of this electrode geometry is termed the castellated geometry having minimum field electric regions in the cavities and maximum electric field regions at the tips. This design was used by Gascoyne to demonstrate the separation of cells and the separation of microbeads [40]. Cells or microbeads undergoing negative dielectrophoresis collected in the cavities of the castellated design while those undergoing positive dielectrophoresis collect at the tips of the teeth.

Dielectrophoretic trapping of DNA was reported at very low frequencies near dc by Asbury and van den Engh and very high frequencies near 1 MHz by Washizu [2, 3, 102-116]. Careful analysis of their results revealed that the characteristic dielectrophoretic trapping differed at these two ends of the frequency spectrum. Asbury and van den Engh observed the DNA to undergo swirling motions over the plane of the electrode along the length of the electrode edge as illustrated in Figure 7-1 [2].

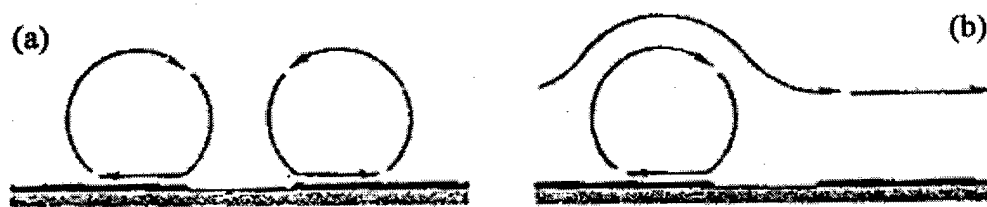


Figure 7-1 Schematic of swirling motion of trapped DNA molecules over electrode edges [2].

Washizu, on the other hand, observed the DNA to be very rigidly held at the electrode edge as opposed to over the plane of the electrode as Asbury and van den Engh observed [114]. Asbury and van den Engh postulated that this swirling may result from heating of the fluid near the electrode edge, thereby, causing a local decrease in the dielectric constant of the fluid. Negative dielectrophoresis of the fluid would then push the less-polarizable fluid out over the electrode where the field strength is weakest. Another explanation as theorized by Asbury and van den Engh, was that the electrode-liquid interface could have diode-like characteristics, allowing charge to exchange more easily in one direction than the other. The corresponding electric field would not be exactly symmetric with respect to a change in field polarity [2].

A review of the literature revealed no information regarding the dielectrophoretic behavior of DNA in the range of excitation frequencies and voltages between those examined by Asbury and van den Engh and Washizu. Also, a study of electrode polarization effects was not found.

7.2.2 Discussion of Dielectrophoresis Studies

An interdigitated parallel electrode geometry similar to that of Asbury and van den Engh and an interdigitated castellated electrode geometry similar to that of Gascoyne [2, 3, 40] were used in this study. Further, DNA sample preparation was similar to that as used by Asbury and van den Engh: 48.5 kb λ phage DNA at a concentration of 200 ng/mL and fluorescently labeled with YOYO-1 iodide while suspended in a Tris-buffer consisting of 0.4 mM Tris, 0.5 mM NaCl, and 0.04 mM EDTA. This benchmark solution was selected for purposes of direct comparison so that their work could first be reproduced and then extended.

With an application of a 30 Hz 1.5 V_{p-p} signal using the interdigitated parallel electrode geometry, it was observed that DNA concentrated over the plane of the electrode along the length of the electrode edge. This is also what Asbury and van den Engh observed in their work (see Figure 7-1). Using the interdigitated castellated electrode geometry at 30

Hz $1.5 V_{p-p}$, it was further observed that DNA concentrated in the cavities of the electrode structure. According to Gascoyne and supported by electric field distribution modeling arguments, this region corresponds to minimum field regions where negative dielectrophoresis occurs [40]. Particles undergoing negative dielectrophoresis concentrate in minimum field regions. An apparently conflicting observation exists concerning the location of trapping between the parallel geometry and castellated geometry. An explanation is not available, but the well defined negative dielectrophoresis regions of the castellated geometry suggest that negative dielectrophoresis of the DNA was observed at these frequency and voltage settings.

At 100 Hz $1.5 V_{p-p}$ using the interdigitated parallel electrode structure, DNA was observed to concentrate over the central region of the electrode. Using the interdigitated castellated electrode structure, DNA was observed to also concentrate over the central region of the electrode instead of in the cavities as observed at 30 Hz. At these frequency and voltage settings, both observations for the two electrode structures support the conclusion that DNA is undergoing negative dielectrophoresis.

The concentration of DNA over the central regions of electrodes was also observed for frequencies and voltages of 1 kHz $1.5 V_{p-p}$, 10 kHz $4 V_{p-p}$, and 100 kHz $8 V_{p-p}$. In addition, at 10 kHz and 100 kHz, not only did the DNA concentrate over the central region of the electrode, it also concentrated over the central region of the gap between electrodes. Therefore, at these frequency and voltage settings all evidence supports negative dielectrophoresis of DNA.

When the frequency and voltage was changed to 1 MHz $10 V_{p-p}$, DNA was observed to concentrate at the edges of electrodes. It did not concentrate over the plane of the electrode near the edge, but rather physically at the edge of the electrode. This location corresponds to maximum field regions. Using the interdigitated castellated electrode geometry, DNA was observed to concentrate at the tips of the teeth, also a maximum field region. The particle's location suggests a positive dielectrophoresis process.

7.2.3 *Summary of Experimental Conclusions*

It is concluded that DNA studied in this research does exhibit negative dielectrophoresis and positive dielectrophoresis based upon the following three pieces of evidence:

- Negative and positive dielectrophoretic theory presented by Pohl and Jones,
- Electric field distribution modeling presented by Gascoyne and Asbury and van den Engh that define minimum and maximum field regions, and
- Experimental observation of characteristic DNA concentration regions under dielectrophoresis as reported in the literature by Asbury and van den Engh, Washizu, and Gascoyne and as reported in this present research.

It is further concluded that DNA must be modeled as a particle that exhibits ohmic and/or dielectric loss as required by the real part of the complex Clausius-Mossotti function, $\text{Re}[\underline{K}]$, of the dielectrophoretic force expression, \overline{F}_{DEP} , developed by Pohl and Jones.

7.2.4 *Uncertainties and Unanticipated Problems*

The following uncertainties exist in the experimental observation of dielectrophoresis of DNA as reported in this research. First, it is uncertain why at an applied field frequency of 30 Hz, DNA concentrates more toward the electrode edge than near the central region of the electrode and only fully transitions to the central region at 100 Hz. One possible explanation may involve the overwhelming effects of ionic conduction at frequencies near dc. Some other mechanism may also exist that prevents DNA concentration over the central region of the electrode. Asbury and van den Engh have suggested that a mechanism may result from heating of the fluid near the electrode edge, thereby, causing a local decrease in the dielectric constant of the fluid. Negative dielectrophoresis of the fluid would then push the less-polarizable fluid out over the electrode where the field strength is weakest. Another explanation as theorized by Asbury and van den Engh, was that the electrode-liquid interface could have diode-like characteristics, allowing charge

to exchange more easily in one direction than the other. The corresponding electric field would not be exactly symmetric with respect to a change in field polarity [2].

It is further uncertain why at 30 Hz, DNA not only concentrates more toward the electrode edge than the central region, but also does so near the electrode edge that corresponds to the leading edge of initial sample injection. If the tendency of DNA is to concentrate near both edges at this frequency, then one possible explanation may involve a depletion layer of DNA that exists after the upstream electrode has already trapped DNA.

Another uncertainty concerns the conformational state of DNA as studied in this research. The exact conformational state as a function of frequency and voltage is not known. It has been assumed to be invariant, or at the least, insensitive to applied electric field frequency and strength.

One unanticipated problem concerns the dielectrophoresis study of BSA. Initial experiments suggest severe non specific adsorption of the BSA to the glass substrate of the microelectrode device. As a result, little BSA remains in solution. This might have been expected because BSA prevents nonspecific adsorption of Taq polymerase in the Genomation Laboratory's Acapella system by coating the walls of the capillary and piezo-electric dispenser before the Taq can adsorb to them. Further, initial experiments suggest difficulty in optical detection of the fluorescently labeled BSA. It is uncertain whether the BSA cannot be detected due to nonspecific adsorption to the glass substrate, or due to a mismatch between the absorption and emission spectra of the fluorescent dye and the filter sets of the epi-fluorescent microscope. What is certain is that individually labeled BSA could not be resolved or detected.

7.3 Potential Applications

One potential application concerns the size separation of DNA using dielectrophoresis. Dielectric properties of DNA are highly sensitive to molecular weight. DNA molecules

of higher molecular weight have larger dipole moments and subsequently larger dielectric constants than DNA molecules of lower molecular weight. As a result, higher molecular weight DNA should be more efficiently trapped than lower molecular weight DNA. It is uncertain what resolution could be achieved between two DNA molecules of different molecular weight. An opportunity exists to better characterize the dielectrophoretic behavior of different molecular weight DNA.

Such a characterization scheme is easy to envision. The dielectrophoretic trapping behavior of different molecular weight DNA could be characterized according to necessary electric field frequency and strength over a range of frequencies. The frequency spectrum could then be divided between negative and positive dielectrophoretic trapping regions. Each unique molecular weight DNA molecule should have unique negative and positive dielectrophoretic trapping regions. Based upon this knowledge, two or more DNA of differing molecular weights could be fluorescently labeled with different dyes and simultaneously viewed with the proper selection of filter sets for the epi-fluorescent microscope. With the ability to simultaneously apply different electric signals to the microelectrode device, the separation of differing molecular weight DNA according to their unique negative and positive dielectrophoresis regions could be observed. DNA molecules undergoing negative dielectrophoresis would concentrate in the cavities of the castellated electrode geometry while those undergoing positive dielectrophoresis would concentrate at the edges of the electrode structures. The DNA molecules would be effectively separated.

The fact that DNA exhibits both negative and positive dielectrophoresis also results in other exciting potential applications. The separation methods of dielectrophoretic migration, dielectrophoretic retention, and dielectrophoretic/gravitational field-flow fractionation take on more relative importance. This is so because these separation methods were initially thought only applicable to particles with size $> 1 \mu\text{m}$ due to the overwhelming effect of random or Brownian motion on particles with size $< 1 \mu\text{m}$. As

experimentally observed here, though, DNA is capable of undergoing negative dielectrophoresis despite the overwhelming nature of random or Brownian motion.

Finally, a potential application exists in achieving optimal dielectrophoretic concentration ability through the use of smaller electrode geometries. The electrode geometries used in this research were 70 μm in width with a 30 μm gap resulting in a characteristic period of 100 μm . There is, however, no reason to limit electrode dimensions to these parameters. Smaller electrode structures with decreased gap dimensions would effectively increase the dielectrophoretic force while decreasing the necessary applied voltages. Two implications follow. First, more DNA could be concentrated in a smaller area. Secondly, driving the necessary applied voltage to smaller values would further miniaturize the system to be inline with microchip logic voltages. A factory on a microchip could be envisioned that employs dielectrophoresis as a manipulative handling technique.

7.4 Future Work

Opportunities exist to contribute to a more detailed characterization of the dielectrophoretic behavior of DNA according to applied electric field frequency, strength and carrier solution properties of pH and ionic strength. It is understood that the low ionic strength medium used in this research is not characteristic of the mediums used in sequencing and polymerase chain reactions (PCRs). Further, future work in this direction may consider the conformational state of DNA and devise appropriate methods to measure this property.

A better characterization of the effects of electrode polarization encountered at low frequencies would be desirable. Such analysis may lend insight into the mechanism behind the observed frequency response difference at low frequencies between thin resistive film electrodes and conductive trace. Finite element analysis methods may be required to better model the effects of electrode polarization. Further, this analysis may lend insight into the apparently conflicting observation that exists concerning the location of trapping between the parallel geometry and castellated geometry at 30 Hz.

Future work may devise a set of protocols capable of characterizing the dielectrophoretic trapping behavior of BSA. As reported, adsorption and optical detection problems were encountered. One solution may be to precoat the channel of the microfluidic device and the glass substrate of the microelectrode device with concentrated unlabeled BSA before sample injection of the labeled BSA. In this manner, the channel and substrate would be saturated with unlabeled BSA leaving labeled BSA in solution for which to examine its dielectrophoretic behavior. Another option would be to examine the dielectrophoretic behavior of DNA in the presence of unlabeled BSA. Changes in dielectrophoretic behavior of DNA in the presence of BSA may also lead to valuable insight.

Future work may characterize dielectrophoretic trapping behavior of DNA and BSA under conditions of flow. Incorporation of separation schemes such as dielectrophoretic migration, dielectrophoretic retention, and dielectrophoretic gravitational field-flow fractionation require flow conditions. The infrastructure now exists at the Genomation Laboratory to conduct these separation studies.

Bibliography

1. Ajdari, A. and J. Prost, *Free-flow electrophoresis with trapping by a transverse inhomogeneous field*. Proc Natl Acad Sci U S A, 1991. 88(10): p. 4468-71.
2. Asbury, C.L., *Manipulation of DNA using nonuniform oscillating electric fields*, in *Molecular Biotechnology*. 1999, University of Washington: Seattle.
3. Asbury, C.L. and G. van den Engh, *Trapping of DNA in nonuniform oscillating electric fields*. Biophysical-Journal, 1998. 74(2): p. 1024-30.
4. Ashkin, A., *Acceleration and trapping of particles by radiation pressure*. Physical-Review-Letters, 1970. 24(4): p. 156-9.
5. Ashkin, A., *The radiation pressure of laser light*. IEEE-Journal-of-Quantum-Electronics, 1972. QE-8(6): p. 577.
6. Ashkin, A., *Applications of laser radiation pressure*. Science, 1980. 210(4474): p. 1081-8.
7. Ashkin, A., *Stable radiation-pressure particle traps using alternating light beams*. Optics-Letters, 1984. 9(10): p. 454-6.
8. Ashkin, A., *Forces of a single-beam gradient laser trap on a dielectric sphere in the ray optics regime*. Biophysical-Journal, 1992. 61(2): p. 569-82.
9. Ashkin, A., *Optical trapping and manipulation of neutral particles using lasers*. Optics-&-Photonics-News, 1999. 10(5): p. 41-6.
10. Ashkin, A. and J.M. Dziedzic, *Optical levitation by radiation pressure*. Applied-Physics-Letters, 1971. 19(8): p. 283-5.

11. Ashkin, A. and J.M. Dziedzic, *Observation of radiation-pressure trapping of particles by alternating light beams*. Physical-Review-Letters, 1985. 54(12): p. 1245-8.
12. Ashkin, A. and J.M. Dziedzic, *Optical trapping and manipulation of viruses and bacteria*. Science, 1987. 235(4795): p. 1517-20.
13. Ashkin, A., et al., *Observation of a single-beam gradient force optical trap for dielectric particles*. Optics-Letters, 1986. 11(5): p. 288-90.
14. Ashkin, A., J.M. Dziedzic, and T. Yamane, *Optical trapping and manipulation of single cells using infrared laser beams*. Nature, 1987. 330(6150): p. 769-71.
15. Ashkin, A. and J.P. Gordon, *Stability of radiation-pressure particle traps: an optical Earnshaw theorem*. Optics-Letters, 1983. 8(10): p. 511-13.
16. Autodesk, *AutoCAD LT 98*, . 1998.
17. Bone, S., et al., *Conduction and dielectric polarisation in proteins and molecular complexes*. Journal-of-the-Chemical-Society-Faraday-Transactions-I, 1981. 77(7):. p. 1729-32.
18. Bone, S., et al., *Dielectric measurements on hydrated biomacromolecules*. 1975: 1975 Dielectric Materials Measurements and Applications. IEE London UK.
19. Bone, S., P.R.C. Gascoyne, and E. Pethig, *Dielectric properties of hydrated proteins at 9.9 GHz*. Journal-of-the-Chemical-Society-Faraday-Transactions-I, 1977. 73(pt.10): p. 1605-11.
20. Bonincontro, A., et al., *Effect of ions on counterion fluctuation in low-molecular weight DNA dielectric dispersions*. Biophys J, 1984. 45(3): p. 495-501.
21. Chiu, D.T., et al., *Injection of ultrasmall samples and single molecules into tapered capillaries*. Anal Chem, 1997. 69(10): p. 1801-7.

22. Chiu, D.T. and R.N. Zare, *Biased diffusion, optical trapping, and manipulation of single molecules in solution*. J. American Chemical Society, 1996. 118(27): p. 6512-13.
23. Cole, R.H., *Dielectric theory and properties of DNA in solution*. Ann N Y Acad Sci, 1977. 303: p. 59-73.
24. Collins, F.S., et al., *New goals for the U.S. Human Genome Project: 1998-2003*. Science, 1998. 282(5389): p. 682-9.
25. Davis, J.M. and J.C. Giddings, *Feasibility study of delectrical field-flow fractionation*. Separation Science and Technology, 1986. 21(9): p. 969-89.
26. de Levie, R., *The admittance of the interface between a metal electrode and an aqueous electrolyte solution: some problems and pitfalls*. Ann Biomed Eng, 1992. 20(3): p. 337-47.
27. Eden, J., P.R.C. Gascoyne, and R. Pethig, *Dielectric and electrical properties of hydrated bovine serum albumin*. Journal-of-the-Chemical-Society-Faraday-Transactions-I, 1980. 76(pt.2): p. 426-34.
28. Essex, C.G., et al., *Dielectric properties of normal and abnormal lipoproteins in aqueous solution*. Ann N Y Acad Sci, 1977. 303: p. 142-58.
29. Essex, C.G., et al., *Five-component dielectric dispersion in bovine serum albumin solution*. Physics-in-Medicine-and-Biology, 1977. 22(6): p. 1160-7.
30. Fink, H.W. and C. Schonenberger, *Electrical conduction through DNA molecules*. Nature, 1999. 398(6726): p. 407-10.
31. Gabler, R., *Electrical Interactions in molecular biophysics*. 1978, New York: Academic Press.

32. Gabriel, C., et al., *Microwave absorption in aqueous solutions of DNA*. Nature, 1987. 328(6126): p. 145-6.
33. Gabriel, C., et al., *Dielectric behaviour of aqueous solutions of plasmid DNA at microwave frequencies*. Biophysical-Journal, 1989. 55(1): p. 29-34.
34. Gascoyne, P.R., R. Pethig, and A. Szent Gyorgyi, *Water structure-dependent charge transport in proteins*. Proc Natl Acad Sci U S A, 1981. 78(1): p. 261-5.
35. Gascoyne, P.R.C., *Electron spin resonance and spectral studies of bovine serum albumin-methylglyoxal complexes*. International-Journal-of-Quantum-Chemistry,-Quantum-Biology-Symposium, 1980(7): p. 93-100.
36. Gascoyne, P.R.C., et al., *Manipulation of erythroleukemia cells using travelling electric fields*. 1994: Proceedings of the 16th Annual International Conference of the IEEE Engineering in Medicine and Biology Society. Engineering Advances: New Opportunities for Biomedical Engineers (Cat. No.94CH3474-4). IEEE New York NY USA.
37. Gascoyne, P.R.C., et al., *Use of dielectrophoretic collection spectra for characterizing differences between normal and cancerous cells*. IEEE-Transactions-on-Industry-Applications, 1994. 30(4): p. 829-34.
38. Gascoyne, P.R.C., R. Pethig, and A. Szent Gyorgyi, *Water structure-dependent charge transport in proteins*. Proceedings-of-the-National-Academy-of-Sciences-of-the-United-States-of-America, 1981. 78(1): p. 261-5.
39. Gascoyne, P.R.C., et al., *Dielectrophoretic separation of cancer cells from blood*. 1995: IAS '95. Conference Record of the 1995 IEEE Industry Applications Conference. Thirtieth IAS Annual Meeting (Cat. No.95CH35862). IEEE New York NY USA.

40. Gascoyne, P.R.C., et al., *Dielectrophoretic separation of mammalian cells studied by computerized image analysis*. Measurement-Science-&Technology, 1992. 3(5): p. 439-45.
41. Grant, E.H., *Dielectric dispersion in bovine serum albumen*. J Mol Biol, 1966. 19(1): p. 133-9.
42. Grant, E.H., S.E. Keefe, and S. Takashima, *The dielectric behavior of aqueous solutions of bovine serum albumin from radiowave to microwave frequencies*. Journal-of-Physical-Chemistry, 1968. 72(13): p. 4373-80.
43. Grant, E.H., R.J. Sheppard, and G.P. South, *Dielectric behavior of biological molecules in solution*. 1978, Oxford: Clarendon Press.
44. Huang, Y., et al., *Introducing dielectrophoresis as a new force field for field-flow fractionation*. Biophys J, 1997. 73(2): p. 1118-29.
45. Jones, T.B., *Electromechanics of Particles*. 1995, Cambridge: Cambridge University Press.
46. Jones, T.B. and M.J. McCarthy, *Electrode geometries for dielectrophoretic levitation*. Journal-of-Electrostatics, 1981. 11(2): p. 71-83.
47. Lorenz, H., et al., *High-aspect-ratio, ultrathick, negative-tone near-UV photoresist and its applications for MEMS*. Sensors-and-Actuators-A-(Physical), 1998. A64(1): p. 33-9.
48. Lorenz, H., et al., *SU-8: a low-cost negative resist for MEMS*. Journal-of-Micromechanics-and-Microengineering, 1997. 7(3): p. 121-4.
49. Lorenz, H., M. Laudon, and P. Renaud, *Mechanical characterization of a new high-aspect-ratio near UV-photoresist*. Microelectronic-Engineering, 1998. 41-42: p. 371-4.

50. Mandel, M., *Dielectric properties of charged linear macromolecules with particular reference to DNA*. Ann N Y Acad Sci, 1977. 303: p. 74-89.
51. Mayer, S., et al., *Electrode recovery potential*. Ann Biomed Eng, 1992. 20(3): p. 385-94.
52. Mayer, S., et al., *Faradic resistance of the electrode/electrolyte interface*. Med Biol Eng Comput, 1992. 30(5): p. 538-42.
53. McAdams, E.T. and J. Jossinet, *A physical interpretation of Schwan's limit current of linearity*. Ann Biomed Eng, 1992. 20(3): p. 307-19.
54. Meldrum, D.R., *Capillary Automated Submicroliter Sample Preparation*, . 1995, University of Washington.
55. Minakata, M., *Dielectric dispersion of polyelectrolytes due to ion fluctuations*. Ann-N-Y-Acad-Sci., 1977. 303: p. 74-89.
56. Mitnik, L., et al., *Segregation in DNA solutions induced by electric fields*. Science, 1995. 267(5195): p. 219-22.
57. Mizuno, A., M. Imamura, and K. Hosoi, *Manipulation of single fine particle in liquid by electrical force in combination with optical pressure*. IEEE-Transactions-on-Industry-Applications, 1991. 27(1, pt.1): p. 140-6.
58. Mizuno, A., et al., *Opto-electrostatic micromanipulation of single cell and DNA molecule*. 1995: MHS'95. Proceedings of the Sixth International Symposium on Micro Machine and Human Science (Cat. No.95TH8079). IEEE New York NY USA.
59. Mizuno, A., et al., *Liquid microvortex generated around a laser focal point in an intense high-frequency electric field*. IEEE-Transactions-on-Industry-Applications, 1995. 31(3): p. 464-8.

60. Mizuno, A., et al., *Handling of single DNA molecule using electric field and laser beam*. 1994: IAS '94. Conference Record of the 1994 Industry Applications Conference Twenty-Ninth IAS Annual Meeting (Cat. No.94CH34520). IEEE New York NY USA.
61. Nilsson, J.W., *Electric Circuits*. 4 ed. Addison-Wesley Series in Electrical and Computer Engineering. 1993, Reading: Addison-Wesley Publishing Co., Inc.
62. Nishioka, M., S. Katsura, and A. Mizuno, *Manipulation of single DNA molecule inside capillary*. Transactions-of-the-Institute-of-Electrical-Engineers-of-Japan,-Part-E, 1996. 116-E(5): p. 171-7.
63. Nishioka, M., et al., *Micro manipulation of cells and DNA molecules*. Journal-of-Electrostatics, 1995. 35(1): p. 83-91.
64. Pedone, F. and A. Bonincontro, *Temperature dependence of DNA dielectric dispersion at radiofrequency*. Biochim Biophys Acta, 1991. 1073(3): p. 580-4.
65. Perkins, T.T., et al., *Relaxation of a single DNA molecule observed by optical microscopy*. Science, 1994. 264(5160): p. 822-6.
66. Perkins, T.T., D.E. Smith, and S. Chu, *Direct observation of tube-like motion of a single polymer chain*. Science, 1994. 264(5160): p. 819-22.
67. Perkins, T.T., D.E. Smith, and S. Chu, *Single polymer dynamics in an elongational flow*. Science, 1997. 276(5321): p. 2016-21.
68. Perkins, T.T., et al., *Stretching of a single tethered polymer in a uniform flow*. Science, 1995. 268(5207): p. 83-7.
69. Pohl, H.A., *Dielectrophoresis*. 1978, Cambridge: Cambridge University Press.
70. Pohl, H.A. and J.S. Crane, *Dielectrophoretic force*. J Theor Biol, 1972. 37(1): p. 1-13.

71. Pohl, H.A. and K. Pollock, *Electrode geometries for various dielectrophoretic force laws*. Journal-of-Electrostatics, 1978. 5: p. 337-42.
72. Qin, D., et al., *Microfabrication, microstructures, and microsystems*. Topics in Current Chemistry, 1998. 194.
73. Sakamoto, M., R. Hayakawa, and Y. Wada, *Dielectric relaxation of DNA solutions. III. Effects of DNA concentration, protein contamination, and mixed solvents*. Biopolymers, 1979. 18(11): p. 2769-82.
74. Schwan, H.P., *Linear and nonlinear electrode polarization and biological materials*. Ann Biomed Eng, 1992. 20(3): p. 269-88.
75. Smith, D.E., T.T. Perkins, and S. Chu, *Self-diffusion of an entangled DNA molecule by reptation*. Physical-Review-Letters, 1995. 75(22): p. 4146-9.
76. Smith, S.B., P.K. Aldridge, and J.B. Callis, *Observation of individual DNA molecules undergoing gel electrophoresis*. Science, 1989. 243(4888): p. 203-6.
77. Smith, S.B., Y. Cui, and C. Bustamante, *Overstretching B-DNA: the elastic response of individual double-stranded and single-stranded DNA molecules*. Science, 1996. 271(5250): p. 795-9.
78. Smith, S.B., L. Finzi, and C. Bustamante, *Direct mechanical measurements of the elasticity of single DNA molecules by using magnetic beads*. Science, 1992. 258(5085): p. 1122-6.
79. SolidWorks, *SolidWorks 98*, . 1998.
80. Takashima, S., *Dielectric dispersion of DNA*. J. Mol. Biol., 1963. 7: p. 455-67.
81. Takashima, S., *Dielectric dispersion of deoxyribonucleic acid. II*. J Phys Chem, 1966. 70(5): p. 1372-80.

82. Takashima, S., *Study of helix-coil transition of DNA by dielectric constant measurement*. Biopolymers, 1966. 4(6): p. 663-76.
83. Takashima, S., *Effect of ions on the dielectric relaxation of DNA*. Biopolymers, 1967. 5(10): p. 899-913.
84. Takashima, S., *Study of dielectric behavior of DNA in shear gradient*. Biopolymers, 1973. 12(1): p. 145-55.
85. Takashima, S., et al., *Dielectric behavior of DNA solution at radio and microwave frequencies (at 20 degrees C)*. Biophysical-Journal, 1984. 46(1): p. 29-34.
86. Tung, M.S., et al., *Influence of temperature and ionic strength on the low-frequency dielectric dispersion of DNA solutions*. Biopolymers, 1977. 16(12): p. 2653-69.
87. van der Touw, F. and M. Mandel, *Dielectric increment and dielectric dispersion of solutions containing simple charged linear macromolecules. I. Theory*. Biophys Chem, 1974. 2(3): p. 218-30.
88. van der Touw, F. and M. Mandel, *Dielectric increment and dielectric dispersion of solutions containing simple charged linear macromolecules. II. Experimental results with synthetic polyelectrolytes*. Biophys Chem, 1974. 2(3): p. 231-41.
89. Volkmuth, W.D. and R.H. Austin, *DNA electrophoresis in microlithographic arrays*. Nature, 1992. 358(6387): p. 600-2.
90. Volkmuth, W.D., et al., *Trapping of branched DNA in microfabricated structures*. Proc Natl Acad Sci U S A, 1995. 92(15): p. 6887-91.

91. Vologodskii, A.V. and N.R. Cozzarelli, *Conformational and thermodynamic properties of supercoiled DNA*. Annu Rev Biophys Biomol Struct, 1994. 23: p. 609-43.
92. Vreugdenhil, T., F. van der Touw, and M. Mandel, *Electric permittivity and dielectric dispersion of low-molecular weight DNA at low ionic strength*. Biophys Chem, 1979. 10(1): p. 67-80.
93. Wang, X., et al., *A theoretical method of electrical field analysis for dielectrophoretic electrode arrays using Green's theorem*. Journal-of-Physics-D-(Applied-Physics), 1996. 29(6): p. 1649-60.
94. Wang, X., W. Xiao Bo, and P.R.C. Gascoyne, *General expressions for dielectrophoretic force and electrorotational torque derived using the Maxwell stress tensor method*. Journal-of-Electrostatics, 1997. 39(4): p. 277-95.
95. Wang, X.B., et al., *A unified theory of dielectrophoresis and travelling wave dielectrophoresis*. Journal-of-Physics-D-(Applied-Physics), 1994. 27(7): p. 1571-4.
96. Wang, X.B., et al., *Selective dielectrophoretic confinement of bioparticles in potential energy wells*. Journal-of-Physics-D-(Applied-Physics), 1993. 26(8): p. 1278-85.
97. Wang, X.B., et al., *Particle dipole-dipole interaction in AC electric fields (cellular application)*. 1994: Proceedings of the 16th Annual International Conference of the IEEE Engineering in Medicine and Biology Society. Engineering Advances: New Opportunities for Biomedical Engineers (Cat. No.94CH3474-4). IEEE New York NY USA.
98. Wang, X.B., et al., *Dielectrophoretic manipulation of cells with spiral electrodes*. Biophys J, 1997. 72(4): p. 1887-99.

99. Wang, X.B., et al., *Non-uniform spatial distributions of both the magnitude and phase of AC electric fields determine dielectrophoretic forces*. Biochim Biophys Acta, 1995. 1243(2): p. 185-94.
100. Wang, X.B., et al., *Separation of polystyrene microbeads using dielectrophoretic/gravitational field-flow-fractionation*. Biophys J, 1998. 74(5): p. 2689-701.
101. Wang, X.B., et al., *Dielectrophoretic manipulation of particles*. IEEE-Transactions-on-Industry-Applications, 1997. 33(3): p. 660-9.
102. Washizu, M., *Electrostatic manipulation of biological objects*. Journal-of-Electrostatics, 1990. 25(1): p. 109-23.
103. Washizu, M., *Manipulation of biological objects in micromachined structures*. 1992: Proceedings. IEEE Micro Electro Mechanical Systems. An Investigation of Micro Structures Sensors Actuators Machines and Robots(Cat. No.92CH3093-2). IEEE New York NY USA.
104. Washizu, M., *Precise calculation of dielectrophoretic force in arbitrary field*. Journal-of-Electrostatics, 1993. 29(2): p. 177-88.
105. Washizu, M., *Electrostatic actuation of liquid droplets for micro-reactor applications*. IEEE-Transactions-on-Industry-Applications, 1998. 34(4): p. 732-7.
106. Washizu, M. and T.B. Jones, *Multipolar dielectrophoretic force calculation*. Journal-of-Electrostatics, 1994. 33(2): p. 187-98.
107. Washizu, M. and T.B. Jones, *Dielectrophoretic interaction of two spherical particles calculated by equivalent multipole-moment method*. IEEE-Transactions-on-Industry-Applications, 1996. 32(2): p. 233-42.

108. Washizu, M. and T.B. Jones, *Generalized multipolar dielectrophoretic force and electrorotational torque calculation*. Journal-of-Electrostatics, 1996. 38(3): p. 199-211.
109. Washizu, M. and O. Kurosawa, *Electrostatic manipulation of DNA in microfabricated structures*. IEEE-Transactions-on-Industry-Applications, 1990. 26(6): p. 1165-72.
110. Washizu, M., et al., *Applications of electrostatic stretch-and-positioning of DNA*. IEEE-Transactions-on-Industry-Applications, 1995. 31(3): p. 447-56.
111. Washizu, M., et al., *Space-resolved manipulation of biological macromolecules*. Proceedings-of-the-SPIE --The-International-Society-for-Optical-Engineering, 1996. 2716: p. 133-43.
112. Washizu, M., T. Nanba, and S. Masuda, *Electrical cell fusion using fluid integrated circuit*. Technology-Reports-of-the-Seikei-University, 1988(45): p. 3061-9.
113. Washizu, M., T. Nanba, and S. Masuda, *Handling biological cells using a fluid integrated circuit*. IEEE-Transactions-on-Industry-Applications, 1990. 26(2): p. 352-8.
114. Washizu, M., et al., *Molecular dielectrophoresis of biopolymers*. IEEE-Transactions-on-Industry-Applications, 1994. 30(4): p. 835-43.
115. Washizu, M., et al., *Molecular surgery based on microsystems*. 1997: Transducers 97. 1997 International Conference on Solid-State Sensors and Actuators. Digest of Technical Papers (Cat. No.97TH8267). IEEE New York NY USA.
116. Washizu, M., et al., *Molecular surgery of DNA using enzyme-immobilized particles*. Transactions-of-the-Institute-of-Electrical-Engineers-of-Japan,-Part-E, 1996. 116-E(5): p. 196-202.

117. Xia, Y. and G.M. Whitesides, *Soft Lithography*. Angew. Chem. Int. Ed. Engl., 1998. 37: p. 550-75.
118. Yang, J., et al., *Cell separation on microfabricated electrodes using dielectrophoretic/gravitational field-flow fractionation*. Anal Chem, 1999. 71(5): p. 911-8.

Appendix A

This appendix outlines the development of the dielectrophoretic force expression as derived by Pohl [69]. The dielectrophoretic force expression as reported in current available literature is inconsistent and difficult to interpret due to various usage of the electric field vector term, \bar{E} . One may encounter \bar{E}_{rms} associated with E_{rms}^2 and \bar{E}_0 associated with E_0^2 . This thesis will be consistent and use \bar{E} to describe the applied electric field vector associated with $|\bar{E}|^2$ in the dielectrophoretic force expression. The development follows.

Consider that the dielectrophoretic force on a neutral body at equilibrium in a static electric field is given as,

$$\bar{F}_{DEP} = (\bar{p} \cdot \nabla) \bar{E}, \quad \text{A.1}$$

where ∇ is the del operator and \bar{E} the applied electric field vector. The static dipole moment vector is given by,

$$\bar{p} = \underline{\alpha} \bar{E}, \quad \text{A.2}$$

where $\underline{\alpha}$ is a complex quantity, denoted by the underbar, and termed the tensor polarizability or dipole moment per unit volume in unit field, v is the volume of the body, and \bar{E} is the applied electric field vector. Substitution of Eq. A.2 into A.1 yields

$$\bar{F}_{DEP} = \underbrace{\underline{\alpha} v}_{\substack{\text{complex} \\ \text{scalar}}} (\bar{E} \cdot \nabla) \bar{E}. \quad \text{A.3}$$

Using the following matrix algebra identity,

$$(\bar{\mathbf{A}} \cdot \nabla) \bar{\mathbf{B}} = \nabla (\bar{\mathbf{A}} \cdot \bar{\mathbf{B}}) - (\bar{\mathbf{B}} \cdot \nabla) \bar{\mathbf{A}} - \bar{\mathbf{A}} \times (\nabla \times \bar{\mathbf{B}}) - \bar{\mathbf{B}} \times (\nabla \times \bar{\mathbf{A}}), \quad \text{A.4}$$

for the term $(\bar{\mathbf{E}} \cdot \nabla) \bar{\mathbf{E}}$ in Eq. A.3 yields

$$(\bar{\mathbf{E}} \cdot \nabla) \bar{\mathbf{E}} = \nabla (\bar{\mathbf{E}} \cdot \bar{\mathbf{E}}) - (\bar{\mathbf{E}} \cdot \nabla) \bar{\mathbf{E}} - \bar{\mathbf{E}} \times (\nabla \times \bar{\mathbf{E}}) - \bar{\mathbf{E}} \times (\nabla \times \bar{\mathbf{E}}). \quad \text{A.5}$$

Knowing that the electric field vector, $\bar{\mathbf{E}}$, can also be written as,

$$\bar{\mathbf{E}} = \nabla \Phi, \quad \text{A.6}$$

where Φ is the electrostatic potential along with the definition, $\nabla \times \nabla \Phi = 0$, the following must be true.

$$\nabla \times \bar{\mathbf{E}} = 0 \quad \text{A.7}$$

Substitution of Eq. A.7 into A.5 then yields,

$$\begin{aligned} (\bar{\mathbf{E}} \cdot \nabla) \bar{\mathbf{E}} &= \nabla (\bar{\mathbf{E}} \cdot \bar{\mathbf{E}}) - (\bar{\mathbf{E}} \cdot \nabla) \bar{\mathbf{E}} - \bar{\mathbf{E}} \times (\cancel{\nabla \times \bar{\mathbf{E}}}) - \bar{\mathbf{E}} \times (\cancel{\nabla \times \bar{\mathbf{E}}}) \\ &= \nabla (\bar{\mathbf{E}} \cdot \bar{\mathbf{E}}) - (\bar{\mathbf{E}} \cdot \nabla) \bar{\mathbf{E}} \end{aligned} \quad \text{A.8}$$

Solving Eq. A.9 for $(\bar{\mathbf{E}} \cdot \nabla) \bar{\mathbf{E}}$ gives,

$$(\bar{\mathbf{E}} \cdot \nabla) \bar{\mathbf{E}} = \frac{1}{2} \nabla (\bar{\mathbf{E}} \cdot \bar{\mathbf{E}}) = \frac{1}{2} \nabla |\bar{\mathbf{E}}|^2. \quad \text{A.9}$$

The dielectrophoretic force expression given in Eq. A.3 can then be written as,

$$\begin{aligned} \bar{\mathbf{F}}_{DEP} &= \alpha \nabla (\bar{\mathbf{E}} \cdot \nabla) \bar{\mathbf{E}} \\ &= \frac{1}{2} \alpha \nabla |\bar{\mathbf{E}}|^2 \end{aligned} \quad \text{A.10}$$

A.11